UNRESTRAINED MEASUREMENT OF ARM MOTION BASED ON A WEARABLE WIRELESS SENSOR NETWORK

LEE GUO XIONG

School of Electrical and Electronic Engineering

A thesis submitted to the Nanyang Technological University
in partial fulfilment of the requirement for the degree of
Doctor of Philosophy

2012

Acknowledgements

I would first like to thank my supervisor, A/P Low Kay Soon for his advice, suggestions, constant support and encouragement during this research period. Being my supervisor as well for my undergraduate URECA and FYP, he has led me into research with much patience and it is my pleasure to continue working under him for my graduate studies.

I would also like to express my gratitude to Mr Tawfiq Taher, MSc Student, AY07/08, for setting the groundwork for my research project by developing the first initial hardware prototype for the wireless sensor modules. I have learned a lot from him in terms of technical skills and practical hardware implementation during my two months stint working with him.

The author is also grateful to the technical staff from Control Engineering Laboratory and Aerospace Electronics Laboratory, Mrs Tan Geok Lan Janet, Mr Chan Hian Kuan, Mrs Lim Guek Har Joanne and Mrs Yap Poh Geok Pamela for their kind assistance and technical support. Janet has been extremely helpful in facilitating administrative matters with her experience and goodwill. Mr Chan on the other hand, has provided valuable support in terms of hardware design, implementation and being a test subject for my experiments for motion tracking.

I am also thankful to a number of other people whom I have met since the embarkment of this journey. Dr Caroline Hargreaves, my tutor during my Ph.D course conducted jointly with Imperial College in my first year, has provided sound advice on the Ph.D process. Dr Bala S Rajaratnam, Manager/Projects from School of Health Science, Nanyang Polytechnic, has given useful insights from a clinician perspective on our project. Dr Cao Runzi and Dr Guo Hao, my seniors, have shared their experience and provided valuable advice on the route

to getting a Ph.D degree.

I would like to acknowledge Nanyang Technological University for the support of my graduate studies through the Nanyang President's Graduate Scholarship.

Finally, I am especially grateful to my parents for their gift of love, care and support. They have scrimped and saved from their humble income to raise me up and support my undergraduate studies and expenses. I am able to continue my academic pursuit today as a result of this gift.

Table of Contents

Abstract

Measurement of human body motion has a myriad of applications ranging from gaming, rehabilitation, animation, virtual reality, sports science and surveillance. Existing methods of motion tracking include visual, mechanical, magnetic and inertial tracking. Visual methods require line of sight and suffer from the notorious occlusion problem. For the existing mechanical or inertial tracking methods, they have cumbersome wirings which hinder the natural movements. In this thesis, a wearable wireless sensor network using inertial/ magnetic sensors is developed to overcome the limitations of these existing methods.

Using tri-axial accelerometer as the sole sensor will lead to singularity when the heading axis is vertical, restricting measurement of orientation to half a vertical plane. A new factorized quaternion approach is proposed in this research to overcome this deficiency with consideration of anatomical and sensor constraints. Different from the conventional approach based on single angle-axis quaternion, the proposed approach factorizes the quaternion into two principal axis quaternions corresponding to two equivalent arm motions. This allows for the implementation of anatomical arm constraints that match the range of arm motion and reduces the ambiguity in solutions. In addition, the singularities arising from the use of tri-axial accelerometers can be detected and resolved for a transient state.

A novel algorithm based on elevation and heading angles is also proposed to determine the orientation of a sensor node equipped with tri-axial accelerometer, gyroscope and magnetometer. Compared to Euler angles, the fixed elevation and heading angles are independent on the temporal order of rotations. In addition, the fixed elevation and heading angles are observable and thus more intuitively visualized. External acceleration due to the rotation of the human arm segment is

estimated using the gyroscope and compensated in the accelerometer output. As the magnetometer is easily affected by magnetic disturbances caused by electrical appliances and ferrous materials, it is decoupled from the accelerometer and used solely for the determination of heading. A new singularity avoidance method is also proposed to resolve the singularity problem that may arise, thereby allowing for measurement through all possible orientations.

Experiments have been performed to evaluate the proposed wearable wireless sensor network in terms of accuracy, latency and power consumption. Experimental results show that the proposed factorized quaternion approach is able to resolve transient singularities and ambiguity arising from the use of triaxial accelerometer. Performance of the novel elevation and heading algorithm is also comparable to an indirect Kalman Filter at a reduced computational cost. The implementation of a singularity avoidance strategy makes the algorithm suitable for implementation in a fixed-point processor. Magnetic disturbances affect only the accuracy of the heading angle and not the elevation angles.

List of Figures

List of Tables

List of Algorithms

CHAPTER 1

Introduction

1.1 Human Body Motion Capture

Human motion capture and tracking has a myriad of applications including gaming, virtual reality [1, 2], animation [3], sports science [4, 5], rehabilitation [6] and surveillance [7]. Existing methods for motion capture include mechanical, visual/optical, audio, radar, magnetic and inertial tracking [8].

Mechanical sensing involves the use of a physical linkage between the target and the environment. The approach involves an articulated series of two or more rigid mechanical pieces interconnected with transducers such as potentiometers or shaft encoders. An example is the goniometer which measures the joint angle by determining the resistance of a potentiometer which changes as the angle between the articulated links changes [9]. Such approach can be very precise and accurate for single pose estimation but is cumbersome and not suitable for long term monitoring.

Visual tracking involves the use of a single or multiple cameras [7, 10]. It can be either visual marker or marker free depending on whether indicators need to be attached to the body parts. The captured images suffer from problems due to occlusion, lighting changes, clutter, shadow and noise. Single camera tracking is normally based on model, contour or feature but it generates ambiguity easily due to occlusion or depth. Multiple cameras can reduce the ambiguity and handle occlusion but they typically involve the use of complicated algorithms with intensive computations. Visual tracking systems are very accurate (errors in 1mm) and are

often used as the standard in human motion analysis. These systems however are costly and are confined to motion tracking in a specialized laboratory.

Acoustic tracking employs the transmission and sensing of sound waves while radar uses radio or microwaves [8]. Both technologies typically operate on the principle of time-of-flight range finding. Both systems suffer from the problem of multipath due to the signal arriving at the receiver via more than one different path. Acoustic signals are prone to reflections about walls and objects in the room, affecting the amplitude and phase of the received signal. The latency of an acoustic system can range from 10 to 100ms and time is also needed for echos from previous measurements to die out before initiating new ones. Electromagnetic waves travel much faster (3×10^8 m/s) but this makes the task of measuring time with sufficient resolution difficult. For instance, a resolution of 1 mm will require the use of a timer with a frequency greater than 300 GHz.

Magnetic systems determine the position and orientation by measuring the magnetic field vector with a magnetic sensor either using a pulsed direct current (DC) field or current induced in electromagnetic coil with a rapidly changing alternating current (AC) magnetic field [11]. The MotionStar DC magnetic tracking system from Ascension, for instance, has a static position accuracy of 8 mm and orientation accuracy of 0.5° in 1.5m range [12]. Both DC and AC technologies are distorted by the presence of ferromagenetic materials in the vicinity which is compensated either by mapping the distortion field through extensive calibration or magnetic shielding. The range of magnetic tracking is also limited by the inverse cubic attenuation of magnetic field as a function of distance from the source.

In recent years, the use of inertial and magnetic sensor in the measurement of human motion have attracted much interest as they are liberated from many

problems associated with other technologies [13–17]. The development and advances in Micro-Electro-Mechanical System (MEMS) technology has also made inertial/magnetic sensors lighter, smaller and cheaper. An inertial/magnetic tracking system uses a combination of accelerometers, gyroscopes and magnetometers. There is no inherent latency associated with inertial/magnetic sensing and all delays in the system are due to data transmission and processing. In addition, this approach is also source-free unlike methods such as electromagnetic, acoustic or optical devices that require emissions from a source to track the objects.

In this thesis, the use of inertial and magnetic sensors for determining the human body motion is investigated. Specifically, the human arm is examined as it has a large number of degrees of freedom.

1.2 Motivations

The interest in home-based rehabilitation schemes have gathered pace in recent years due to the global trend of an ageing population that put considerable strain in many countries' healthcare facilities and services [18]. Inertial/magnetic sensors, being light, small and cheap are good candidates for an ambulatory measurement system used in telerehabiliation [19, 20] conducted in the patient's home or office. The use of inertial/magnetic sensors is also free from privacy issues often related with the use of cameras. In addition, the use of an ambulatory system for a home based rehabilitation program greatly reduces the need for frequent visits to the hospital for the patients. A good ambulatory system has to meet several design criteria: lightweight, easy attachment, little hindrance to natural movement, capability for long term monitoring, high accuracy and ideally low latency.

Previous research work has been conducted to make an ambulatory system for motion tracking portable [21, 22] and wearable [23–26]. However, these systems have many wiring and therefore pose a constraint on natural body motion. As

such, the design of wearable wireless sensor network system is proposed in this thesis to overcome this limitation.

Accelerometers measure the component of its acceleration along each of its sensitive axis. They have been used as an inclinometer assuming that the linear acceleration due to the body segment to which it is attached is small as compared to the gravitational acceleration [14, 27]. The heading of the accelerometer with respect to the gravity axis however is unknown. As such, a magnetic sensor is commonly used for the determination of heading information. However, the presence of ferromagnetic material in the cluttered home or office environment will affect the accuracy. Method for compensating magnetic inferences is difficult in an ever-changing home or office environment. Gyroscopes can be used to determine the heading but they suffer from the notorious drift problem which makes them unsuitable for long term monitoring. A more common approach is to use gyroscopes together with an accelerometer to compensate for the dynamic movements and with magnetic sensors for compensation of the fluctuating magnetic fields.

In view of the limitations of these sensors, an accelerometer-only approach in the tracking application remains attractive even today. In addition, the cost of an accelerometer is very low and draws much less current as compared to the gyroscope and magnetometer. Accelerometers are thus a very attractive candidate to be used in battery-powered sensor nodes for long term monitoring.

1.3 Objectives

The objectives of this thesis are as follows:

- Investigate and evaluate a wearable wireless sensor network system based on tri-axial accelerometers. Each sensor node should be autonomous and perform processing and recording of data without an interrogation unit [28].

Thus it is completely untethered, driven by a wireless capability with a rechargeable power source. In addition, each sensor node should also be low in power consumption.

- Investigate the maximum information that can be obtained from a tri-axial accelerometer for tracking the motion of the human arm while factoring in the anatomical constraints of the human arm. This information will enable the physiotherapist to determine the types of motion that are measurable for monitoring the progress of the rehabilitation process in restoring the functional use of the arm.
- Develop a new algorithm to extend measurement of orientation with the use of a triad of triaxial accelerometer, magnetometer and gyroscope sensors. The algorithm should take into account the influence of the magnetic disturbances on the accuracy of orientation estimates using the magnetometer and the use of the gyroscope in modelling the kinematics of the segment.

1.4 Main Contributions

The following lists the main contribution of this thesis:

- **Proposal and development of a new factorized quaternion approach to determine arm motions using accelerometers with anatomical and sensor constraints**

  With the proposed approach, the measurement can be extended to measure rotations along the arm segment long axis in this work. Due to the constraint of the accelerometer in the determination of heading information, measurement of the motion for the upperarm is limited to a single vertical plane. For forearm, the measurement can be extended along a tilted plane by making use of the information on the upperarm. Different from

the conventional single angle-axis quaternion, a factorized quaternion approach is proposed to determine the motion of the articulated arm limbs. This approach has three main advantages: 1) Singularities arising from the use of accelerometers can be detected and resolved for a transient state. 2) Anatomical constraints adhering to the range of arm motions can be incorporated to reduce the ambiguity in solutions. 3) Measurement of the arm movements can be limited to a single plane without the need for an additional optimization constraint.

- **Proposal and development of an elevation and heading angles based algorithm for orientation determination**

  A new algorithm based on the use of elevation and heading angles is proposed for orientation determination. The elevation angles are defined as the angles of the sensor's axis with respect to the horizontal plane and the heading angle is defined as the angle between the projection of the heading axis on the horizontal and the magnetic north. The kinematics of the rotation of the body segment is modelled about a fixed point of rotation and used to estimate the external acceleration using the gyroscope. The use of the magnetometer is decoupled from the accelerometer and used solely for the determination of heading. A novel singularity avoidance strategy is proposed to avoid any possible singularities that may arise and makes the algorithm suitable for implementation in a fixed point processor.

- **Development of an Unrestrained Arm Motion Measurement System**

  A wearable wireless sensor network based on triaxial accelerometers to measure arm motion has been developed which allow for unrestrained measurement of body limb motion. Initial studies have been performed on the measurement of the arm motion along the sagittal plane with one degree

of freedom for each arm limb. The lightweight and compact size of the developed sensor node makes its attachment to the limb easy. Experimental results have shown that the system has good accuracy and response rate when benchmarked with a goniometer.

1.5 Outline of thesis

The rest of the thesis is structured as follows.

Chapter 2 provides a literature review of the related research in motion tracking based on inertial/magnetic sensors. The challenges and limitations of the existing work are also identified in this literature review.

Chapter 3 presents the development of a wearable wireless sensor node. The system configuration in first described followed by the selection of wireless standard and protocol. The estimation of the latency of the system is presented for a single and multiple-sensor node network. A calibration procedure for the accelerometer is then introduced using a precision rotary stage.

In Chapter 4, an algorithm for tilt measurement is proposed with a single degree of freedom using a tri-axial accelerometer. The performance of the wearable wireless system implementing the tilt measurement algorithm is evaluated experimentally under a set of common benchmarks for a motion tracking system, namely accuracy, latency and power consumption. Measurement of orientation is then extended to two degrees of freedom using the Euler angles with rotation matrices and quaternions. A single angle-axis quaternion approach is also proposed to find the orientation of the articulated human arm limb (the upperarm and forearm). Numerical simulations results are presented to demonstrate the performance of the single-axis quaternion algorithms.

Chapter 5 presents in details the proposed factorized quaternion approach. The proposed algorithm is the first to use the concept of factorized principal axis

quaternion to determine orientation of the arm limb to resolve transient singularities and reduce ambiguity in the solutions. Simulation studies show that this approach is able to overcome the weakness of the conventional single angle-axis quaternion approach. The performance of the factorized quaternion using the tri-axial accelerometer is then benchmarked experimentally with a proprietary sensor fusion algorithm in a commercial multiple sensor inertial measurement unit. The results show that the factorized quaternion approach is able to resolve the transient singularities, reduce ambiguity in solutions while implicitly implementing the constraint of motion measurement in a single plane.

In Chapter 6, the formulation of a new algorithm based on fixed elevation and heading angles in orientation determination is described. Instead of using Euler angles which depend on the temporal order, the elevation angles of the sensor node is determined using the accelerometer while the heading is determined using the magnetometer. External acceleration due to the rotation of the human arm segment is estimated using the gyroscope and compensated in the accelerometer output. A novel singularity avoidance method is also proposed to avoid singularities that may arise during measurement. Experimental results show that the performance of the elevation and heading algorithm is comparable to an indirect Kalman Filter at a reduced computational cost. With the singularity avoidance strategy, the maximum value of the elevation angle of the heading axis is capped, allowing for the implementation using a fixed point processor without arithmetic overflow. The presence of magnetic disturbances affects only the accuracy of the heading angles.

Chapter 7 summarizes the research work and describes the directions of future research in wearable wireless sensor for human motion measurement.

CHAPTER 2

Literature Review

2.1 Introduction

Inertial sensors such as accelerometers and gyroscopes have been widely used since the 1950s in inertial navigation systems and attitude determination systems in aircrafts, ships, submarines and satellites. Magnetic sensors on the other hand have been used for over 2000 years to indicate horizontal directions. Accelerometers and gyroscopes are known as inertial sensors as they exploit the property of inertia, namely the resistance to change in momentum; to sense changes in linear motion for the accelerometer and angular motion for the gyro. These sensors then were however bulky and expensive and thus unsuitable for use in human motion capture. In the 1970s, low cost and small sized (less than 2cm) strain-gauge accelerometers became available which lead to preliminary investigation into its use in measurement of human movements [29]. Problems such as low sensitivity, absence of a steady state response, noise and bulk of associated electronics impeded the adoption of this technology in human motion measurement. It was not until the late 1990s with the advent of microelectronic mechanical systems (MEMS) that the use of inertial sensors in human motion tracking started to take off. Similarly, the magenetoresistive effect was discovered by Thompson in 1856 but it was only until the last three decades that thin film technology enabled the production of practical miniature magnetic sensors for application use [30].

In this chapter, the principle of operation of common MEMS inertial and magnetic sensors is first briefly introduced. An overview of relevant research work

on the use of inertial and magnetic sensors in measurement of human motion is then presented together with their merits and limitations.

2.2 Principle of Operation of Inertial/ Magnetic Sensors

Accelerometers measure the linear acceleration, i.e the rate of change of velocity with respect to time. Most MEMS accelerometer today are capacitive acceleration sensors. In such devices, a beam attached to a central mass is moveable under the influence of acceleration. As the distance between the moveable and fixed beams changes, the capacitance in turn changes which can be used to extract acceleration information.

A gyroscope is an angular rate sensor which can be used to determine the angular velocity. The word gyroscope came from the Greek-words *gyros* which means "rotation" and *skopein* which means "to view". MEMS based gyroscopes are designed to measure angular rates using the Coriolis force. In such a gyroscope, a silicon structure such as a tuning fork is driven by an oscillator to vibrate at a precise amplitude and frequency along a single plane. An applied angular rotation about an axis parallel to this structure generate a Coriolis acceleration of direction perpendicular to both the rotation axis and vibrating velocity. This oscillatory Coriolis force is then used to produce a DC signal of magnitude proportional to the rotation rate by a detector element and signal conditioning circuitry.

A magnetometer is a device that measures the magnetic field [31]. There are many types of magnetometers, eg. fluxgate, magnetoresistive sensors, Hall-Effect sensors etc. One of the most common type is the anisotropic magnetoresistive (AMR) sensor. This sensor is made up of thin strips of permalloy (an alloy of nickel and iron) whose electrical resistance varies with a change in applied magnetic field. In the presence of a magnetic field, a change in the Wheatstone

bridge resistive elements causes a corresponding change in voltage across the bridge outputs. These resistive elements are aligned together to have a common sensitive axis that will provide positive voltage change with magnetic fields increasing in the sensitive direction. As the output is in proportion to the one-dimensional axis (the principle of anisotropy) and its magnitude, additional sensor bridges placed at orthogonal directions permit accurate measurement of arbitrary field direction.

2.3 Related Research

2.3.1 Inertial Tracking using Accelerometers

An accelerometer measures the acceleration along its sensitive axis. In inertial navigation systems (INS), the gravity vector is offset from the accelerometer reading to determine the external acceleration. In the absence of bias, the acceleration can be integrated twice to obtain the position estimates. However, any errors in deriving the acceleration will be integrated with time producing velocity errors. These velocity errors are in turn integrated with time generating position errors. A constant bias causes a position error that grows quadratically with time. Strapdown INS typically require precision accelerometers with bias uncertainties of less than 50 μg [32]. For low cost MEMS sensors with bias uncertainty in the order of milli-g, this drift in distance error with time makes position estimates using MEMS accelerometers unsuitable for many long term monitoring applications.

Alternatively, the accelerometer can be used as an inclinometer for tilt measurement by measuring the acceleration due to gravity in static condition or in semi-static conditions where the external acceleration is small as compared to the gravitational acceleration. Since most real-life objects do not experience constant linear acceleration, the gravity vector can also be estimated by averaging the accelerometer over a sufficient long period of time. Since measurements using this approach do not entail integration of the accelerometer output, errors in

inclination/orientation determination typically do not drift with time.

Bernmark and Wiktorin [33] performed studies on measuring elevation of the human arm during flexion and abduction movements from normal to high velocities. However, their measurement was limited to a single degree of freedom. In addition, their approach was not able to differentiate between flexion and abduction movements nor measure rotation about the arm's longitudinal axis.

Cheng et al. [34] described the use of bi-axial MEMS accelerometers for the measurement of joint angles between rigid bodies using two methods. The first method called the Common Mode Rejection (CMR) made use of the ratio of the output of the accelerometers mounted on adjacent links attached ideally at the same joint to determine the joint angle. The second method called Distributed Common Mode Rejection (DCMR) made use of two accelerometers mounted on the same link to estimate the acceleration vector at the joint. The acceleration vector at the adjacent link was determined in a similar manner and the ratio of these two acceleration vectors at the same joint was again used for determination of the joint angle. Experimental results showed that the angular error from CMR is 0.4 rad compared to 0.03 rad using DCMR. These two methods however are restricted to one degree of freedom joint angle measurement between rigid links and requires more than one accelerometer distributed along each link for the DCMR method.

Luinge and Veltink proposed a Kalman filter [27] to estimate the offset, acceleration and gravitational vector. The external acceleration was assumed to have a bandpass characteristics and modelled as an autoregressive process. The bias was assumed to have a bandwidth that is low with respect to the acceleration and is modelled as a Markov process. The states of the Kalman Filter are the error in gravity vector and bias estimates. However, with a zero state transition matrix and the matrix connecting the state to the measurement being column rank-deficient,

the states of the formulated Kalman Filter are generally non-observable [35]. Experiments were conducted for the inclination measurement (angle of z-axis with respect to the vertical) for the human trunk and pelvis during lifting tasks and errors were found to be 2° rms. Experimental results also showed that the bias offset estimation is more accurate when the sensitive axis is in the direction of gravity.

Measurement was extended to two degrees of freedom by Lee and Ha [36] using rotation matrices based on Euler angles. A calibration method was proposed to account for non-orthogonality of the sensor axes. To better estimate the gravity vector and compensate for dynamic motions, they proposed placing two triad of accelerometers at different lengths from the axis of rotation. The shortcoming of their work was that no benchmarks or comparison with truth data were performed.

The advantages of the MEMS accelerometer are the small size, low cost and low current consumption (can be as low as 0.01mA but typically <0.5mA) which allow for long term continuous monitoring. One of its main drawback is the assumption that the magnitude of the external acceleration is much less than the gravitational acceleration. If the dynamic motion has large acceleration, inaccurate measurements of body movements will be observed. In addition, the accelerometer is unable to differentiate rotation about the vertical axis.

2.3.2 Measurement using Accelerometer and Gyroscope

A gyroscope measures the angular velocity. The change in orientation can be obtained by integrating the angular velocity with respect to time. However, integration of the gyroscope output results in a drift in orientation due to biases in the gyroscope and noise. A constant bias error when time integrated causes an angular error that grows linearly with time. Successful Attitude Heading and Reference Systems (AHRS) and Inertial Navigation System (INS) require very

expensive gyroscopes (e.g. ring laser and fibre optic gyroscopes) that have exceptional long term bias stability (0.01 °/hour) [32]. For low cost inertial sensors based on MEMS, the accuracy is typically in the order of degrees per second. As such, the performance of systems associated with MEMS gyroscopes are unacceptable for many applications. The accelerometer is therefore often used to provide an absolute reference orientation to the gyroscope.

Rehbinder and Hu [37] proposed a linear Kalman filter for fusing the data from the gyroscope and accelerometer. The norm of the accelerometer output was used for the detection of external acceleration and used to switch the Kalman Filter in between two modes: low acceleration and high acceleration. The system in the low acceleration mode is observable and the convergence of the filter is assured. The system in the high acceleration mode however is unobservable and the filter could diverge. The overall Kalman Filter is shown to be stochastically observable if a bound is implemented on the minimum and maximum time that the system is in each mode. Simulation results showed that the estimates are stable even in the presence of external accelerations. The algorithm however was not validated using real experimental data. In addition, the proposed Kalman Filter only estimates the pitch and roll angle of the orientation. The performance of the filter in the determination of yaw information was not addressed.

Luinge and Velthink [38] modelled the gyroscope offset as a first order Markov process and the external acceleration as a first order low-pass filtered white noise. An initial orientation estimate was first obtained by integrating the gyroscope output. The estimate of the vertical direction in the sensor coordinates obtained using the gyroscope was then combined with the accelerometer data using a Kalman filter. The states of the Kalman filter are the orientation error and the gyroscope offset error. However, the states are non-observable in the absence of external acceleration or in the presence of uniaxial external acceleration in their formulation. Experimental results showed that inclination error drift was improved compared

to that obtained from integration of the gyroscope output. However, since the estimate of the vertical direction used in the Kalman filter provides no information on rotation about the vertical axis, the drift in heading problem remained.

In [39], Luinge et al extended the work in [38] to determine the orientation of the arm limb. The orientation of the sensor's axes with respect to the arm limb was determined and used for calibration by making use of the gyroscope and the accelerometer output in predefined motions and arm positions. A constraint was also imposed on the orientation determined in [38] to minimize the adduction angle at the elbow joint. Experimental results show that the algorithm with the additional constraint was able to address orientation drift when the adduction axis is vertical, i.e. when the forearm was horizontal.

In [40], Zhang et al proposed a quaternion-based particle filter to fuse the accelerometer and gyroscope data to estimate the orientations of the upperarm and forearm in the first run. The particle filter was then run a second time to incorporate geometrical constraints in the abduction/adduction and range of flexion/extension and pronation/supination of the elbow joint to compensate for drift and improve the estimation accuracy. Experimental results showed that the adduction movements were kept small and that errors in the range of flexion/extension could be corrected.

In general, dynamic movements can be better estimated as compared with an accelerometer-only approach by using an additional gyroscope. The drawback is the high current consumption of MEMS gyroscopes (3–7 mA). In addition, the drift problem from the gyroscope remains in the determination of heading since the accelerometer is unable to differentiate rotations about the vertical axis. Moreover, the MEMS gyroscope's variation with temperature in the bias and sensitivity are much more significant. Temperature compensation is therefore required if the gyroscope is to be used over a range of temperatures. For this reason, many gyroscopes come with integrated temperature sensors.

2.3.3 Measurement using Accelerometer and Magnetometer

Since the accelerometer is unable to determine the heading information, a magnetometer is often added to detect the Earth's magnetic north and measure the horizontal component of orientation. The accelerometer compensates for the tilt of the magnetometer by determining the pitch and roll angles.

In a work done by Kemp et al [14], the vertical inclination and azimuth angles were computed by taking the ratios of the three axes outputs from a triad of orthogonally placed single-axis accelerometers and magnetometers. The advantage of their approach is that the determination of azimuth is independent of the magnetic dip angle and magnetic field strength. It is therefore not necessary to re-calibrate the sensors when used in locations with different earth-magnetic fields. The shortcoming of their work however is the absence of information on the rotation about the heading axis required for describing full three degrees of freedom orientation.

Gebre-Egziabher et al [41] described an attitude determination algorithm based on the earth magnetic field vector and gravity vector. An error quaternion was formulated based on the Wabha's problem [42] and solved using an iterated least square method. Without any angular rate information, the rate of change of the error quaternion was modelled using an exponentially correlated Gauss-Markov process model. The error quaternion can then be solved using a Kalman filter. Experimental results showed that the mean errors were less than 1° with the standard deviation of errors being 11° for yaw and 3° for pitch and roll.

Zhu et al [43] proposed an azimuth level detector which consisted of three nominally orthogonal MEMS accelerometers and three nominally orthogonal magnetometers. The Euler angles corresponding to roll, pitch and yaw were computed

using the direction cosine matrix. The non-orthogonality of the axes was modelled and a compensation of the error performed via arithmetic. A measurement accuracy of $\pm 0.5^\circ$ for tilt and $\pm 0.7^\circ$ for azimuth was claimed to be achieved in the tests conducted.

Yun et al. [44] developed a factored quaternion algorithm (FQA) to decouple accelerometer and magnetic data and eliminate the influence of magnetic variations on calculations that determine pitch and roll. Azimuth data calculations were based solely on magnetometer data. Experiments found that the accuracy of the FQA is similar to the QUEST algorithm for attitude determination [45] but it is 25% computationally more efficient.

With the current consumption of typical AMR magnetometers at 0.8–0.9 mA which are only slightly higher than the MEMS accelerometers and its cost lower in recent years [46], the integration of the magnetometer and the accelerometer is emerging in applications where power consumption and cost requirements are less stringent. However, the main problems of external acceleration with the accelerometer remains which limits the accuracy of this approach in dynamic motions. The output of the magnetometer is also affected by local magnetic interferences in the environment. The disturbances from the environment can be categorized into hard and soft iron distortions [47, 48]. The hard iron distortions arise from permanent magnets and magnetized substances in a fixed location relative to the magnetic sensors, for instance the platform on which the sensor is mounted. This distortion adds a constant bias to the sensor outputs and can be compensated by calibration. The soft iron distortions arise from the interaction of the earth's magnetic field and any magnetically soft material in the environment, for instance vehicles that move independently with respect to the magnetometer. These distortions are non-deterministic and the compensation is more difficult. The magnetic field caused by soft iron distortion is often modelled as proportionate to between the magnetic field applied to a soft iron and the resulting induced

magnetic field. As such, the approach using accelerometer and magnetometer is generally only suited for measurements with static or slow movements in a calibrated controlled environment or an environment free from magnetic disturbances.

2.3.4 Measurement using Inertial and Magnetic Sensors

Full three degrees of freedom orientation measurement is commonly performed using a combination of orthogonal triad gyroscopes, accelerometers and magnetometer. These sensors are usually used in a complementary manner where the gyroscope is used as a high frequency source of orientation information while the accelerometer and magnetometer are used as a low frequency orientation information source.

Foxlin [49] described a complementary extended Kalman filter using a rate gyroscope, fluid inclinometer and fluxgate compass for the determination of the orientation of a head tracker for virtual reality applications. Estimation of the bias of the rate-gyro was decoupled from the estimation of Euler angles in the filter states using Friedland's formulation [50]. By testing for the time in which the tracker is in nonzero angular velocity, the effect of linear accelerations in the inclinometer was accounted for by varying the covariance of the inclinometer measurements. Experimental results showed that the filter was drift free and was able to compensate for the drift of the rate-gyros using the output from the inclinometers.

Zhu and Zhou [16] proposed a Kalman filter in which the states are the gravitational acceleration and earth magnetic field vector, leading to a linear process equation in which the block diagonals of the state transition matrix are the skew-symmetric matrices of the angular velocities. Instead of finding the Euler angles corresponding to the orientation, the joint angle between the limb segments were determined. The position of the end of the lowerarm was also estimated using the orientation information. Experiments performed under constant orientation

showed that the algorithm did not have increasing drift compared to an integral algorithm. Dynamic rotations performed on a rotary table showed an error of 1°. However, the accuracy at various angular speeds of rotations were not investigated. Experimental results of position estimates along a horizontal and vertical axis showed an error of less than 1 cm. As the position estimate was derived using the orientations and positions of the corresponding segments, the accuracy of this approach is dependent on the measurement accuracy of all the sensors and physical dimensions of the limbs. In [51], Zhu and Rong integrated the output from their azimuth-level detector [43] utilizing a 3-axis accelerometer and magnetometer with the output from a 3-axis gyroscope in a strapdown system. The scale, skew and drift errors as defined in [52] were analyzed. Simulation and experimental results show that the hybrid system was able to restrain long-term drift and dynamic perturbations.

Bachmann et al. [53] proposed a quaternion-based attitude filter algorithm for orientation tracking with the purpose of inserting human postures into a virtual reality environment. Sensor modules were developed which made use of three orthogonal rate sensors, accelerometers and magnetometers in each sensor package. The sensor units were termed as Magnetic Angular Rate Gravity (MARG) sensors. Filter error correction of the algorithm was performed by using the Gauss-Newton iteration based on linearized least square regression analysis. In [54], the filter was improved by introducing a more efficient computation of the correction step which made use of the orthogonality of the correction step to preserve the unity of the quaternion. Conditions for a tunable parameter was derived in [55] for the convergence of the filter within a reasonable time period as well as for the suppression of maneuver noise.

In [56], Marins et al. proposed two different approaches to an extended Kalman filter (EKF). In both approaches, the 7-parameter state vector consists of the angular rate and quaternion representing the orientation. For the first approach,

the 9-parameter measurement vector consists of the 3D angular rate, acceleration and magnetic fields which leads to a nonlinear relationship between the state vector and the measurement vector. The second approach used either the Newton or Gauss-Newton method to estimate a quaternion using the accelerometer and magnetometer measurements. The estimated quaternion was then used together with the angular rates as the measurement vector. This leads to a linear relationship between the measurement vector and the state vector and a computationally more efficient Kalman filter design as compared to the first approach. In a follow up work by Yun et. al [57], a reduced-order implementation of the Gauss-Newton method in the second EKF was proposed to further improve the computational efficiency. In [58], the iterative Gauss-Newton method was replaced with the QUEST algorithm [45] and the closed-form factored quaternion algorithm developed in [44]. Experiments were then carried out using the MARG sensors with an on-board RISC controller [59]. Calibration was performed using either a Hass rotary table or by hand placing the sensor in predetermined orientations and subjecting the sensor to rotations about certain axes . Implementation of up to 15 MARG sensors with a central interface unit (CIU) and the design of the 3D human avatar in virtual reality was described in [60]. Experimental results summarized in [17] showed that the proposed EKF was able to better estimate the orientation during rotation motions compared to the QUEST algorithm while eliminating the jittering and spiking in QUEST estimates. Benchmarking with the Hass rotary table showed a static accuracy of 2° and dynamic accuracy of 9°.

Calusdian [61] proposed a complementary filtering algorithm which utilized a single gain parameter that can be adaptively adjusted based on the type of motion being measured. For low dynamic motion, a low gain can be chosen which relies more on the quaternion estimation using the factored quaternion algorithm in [44] based on the accelerometer and magnetometer output. In dynamic motion, a high gain can be chosen to place more weight on the estimated quaternion using the

gyroscope output. The detection of the type of motion was based on the magnitude of the angular rate sensor. Experiments performed on a pendulum showed a comparable accuracy to commercial sensor fusion algorithm. This was however achieved by switching between two gain values for maximum performance based on the collected experimental data. For real-time measurement, a systematic metric for categorizing the dynamics of motion to vary the gain parameter is desired.

Roetenberg et al [15, 62] extended the Kalman filter formulated in [38] by including the magnetometer data. The magnetic disturbance was modelled as a first order Markov process with a bandwidth larger than the gyroscope drift. A method for the compensation of magnetic disturbance was proposed. If the norm of the magnetic field differs from the undisturbed Earth's magnetic field strength, the variance of the magnetic disturbance noise in the Markov process model was increased. Similarly, if the calculated magnetic dip angle differs from the known location dip angle, the variance of the magnetic disturbance noise was increased. Experimental results showed that the error using the Kalman filter with magnetic compensation in the presence of magnetic disturbances was 2.7° rms while the Kalman filter without magnetic compensation was 11.8° rms.

Sabatini [63] proposed a quaternion based extended Kalman filter which included the biases of the accelerometer and gyroscope in the state vector. Observability of the biases is based on the assumption that most human motion exhibit rest periods of some duration during which there is zero attitude for gyroscope calibration and zero velocity for accelerometer bias capture. In addition, if the norm of the measured accelerometer is deviated from the gravitational acceleration, the variance of the accelerometer measurement noise was set to infinity (gating strategy). Similarly, if the norm of the magnetometer output is deviated from the known local magnetic field strength or the estimated magnetic dip angle is deviated from the known magnetic dip angle, the variance of the magnetometer measurement noise was set to infinity (gating). Experiments showed

that the proposed filter performed well in the presence of simulated motion and magnetic disturbances. Accuracy of the proposed filter was comparable with that of a commercial Inertial Cube2 sensor from InterSense.

In [64], Suh proposed a quaternion-based indirect Kalman filter to estimate the orientation error represented by an error quaternion. The Kalman filter is modified such that the magnetic sensor is used only for yaw estimation error compensation. Instead of using the norm of the accelerometer output for the detection of external acceleration, the external acceleration was estimated from the filter residual. The advantage of this approach is that the direction of the external acceleration can be estimated and compensated by using smaller weights to accelerometer values affected by it.

In [65], Zhang et al extended the work in [40] by including the magnetometer in addition to the accelerometer and gyroscope in the particle filter to determine the orientation of the upper limbs. The geometric constraint was included in the second run of the particle filter to limit the angle of abduction/ adduction of the elbow. Experimental results obtained by benchmarking the inertial/magnetic MTx sensor units with a BTS SMART-D optical motion capture system showed that the particle filter with geometrical constraint had a greater correlation in the upperlimb's Euler angles compared with the particle filter without the geometric constraint.

By using the orientation of the body segment together with knowledge of the segment length and joint characteristics, relative positions on the body and angles between the segments can be estimated. For instance, by using the Euler angles obtained from orientation estimates using an inertial sensor, Zhou et al [24] determined the position of the wrist using a kinematic model of the human arm filtered using weighted least square. A simulated annealing was also proposed by Zhou and Hu [66] to reduce the errors in measurement and to factor in a constraint on the length of the human arm. In [67], Zhou and Hu proposed a

Kalman filter based on the difference between the inclination measurements from the accelerometers and gyroscopes. This difference was used for the correction of the estimated orientation and turning rates. The drifts in measurement position of the wrist and elbow were found to be reduced after applying the proposed Kalman Filter.

2.3.5 Hybrid Approaches

To improve the tracking performance of inertial sensors or magnetometers, other types of sensors are often used together with an aiding method.

Foxlin et al [68] developed a tracking system using inertial sensors aided by ultrasonic time of flight range measurements to a constellation of wireless transponder beacons. Angular rates measured by the gyros were integrated to obtain the orientation. The orientation was then used to transform the acceleration measured by the accelerometers from the body referenced frame to the navigation frame. The gravitational acceleration was then offset from the acceleration and then doubly integrated to obtain position estimates. This was then combined with ultrasonic range measurements using an EKF to correct for position drifts. Simulations and experimental results showed that the tracker was capable of achieving 1-3mm accuracy in a tracking region of 9 ft along each direction.

Roetenberg et al [69] combined the inertial measurement unit developed in [15] with a portable magnetic tracking system developed in [70] for ambulatory determination of 3D position and orientation in human motion tracking. The magnetic tracking system consists of a magnetic source with three orthogonal coils which can be mounted onto the back of the human body. 3D sensors can be placed on the body segment to measure the field generated by the source. Since the field strength is a function of distance and orientation of the sensors with respect to the source, the position and orientation can be determined in the equations as described by Kuipers [71]. To ensure sufficient signal-to-noise ratios at the magnetic

sensors, a strong field is required at the source which required a continuous driving of a current up to 1.5A. This high current consumption therefore limited the update rate of the magnetic system to be set at a low rate of 1.7Hz. In between magnetic measurements, the position and orientation were determined from the inertial measurement unit. Experimental results showed that the accuracy was about 5 mm for position and 3° for orientation when benchmarked with a lab bound camera system.

Tao and Hu proposed a hybrid approach to 3D arm motion tracking for telerehabilitation application. In [72], an extended Kalman filter (EKF) was proposed to fuse data from visual and inertial sensors. An optimization framework was implemented after the EKF to factor in the arm length constraint and projection of the wrist joint and 2D image position. In [20], a particle filter (PF) was used instead of the EKF to fuse the data from inertial sensors and a camera in a probabilistic manner. A dynamic system model of constant acceleration was used to reduce the state space of the system by pruning. Since 2D image measurements information from the camera is insufficient to estimate the 3D position, a physical arm length constraint was introduced to fuse data in a layered manner. Experimental results benchmarked with a commercial marker-based Qualisys showed that the PF with constraint outperformed the EKF and PF without constraint.

2.4 Summary

In this chapter, a literature review on the recent research work in the use of inertial/magnetic sensors for human body motion tracking has been presented. Table 2.1 summarizes the advantages and drawbacks of the different approaches and the challenges and limitations during implementation. Determination of position by integration of accelerometer output and orientation by integration of gyroscope

angular rate output are generally difficult due to the time integration of bias associated with MEMS inertial sensors. Determination of orientation using either the accelerometer or magnetometer usually does not entail time integration and thus the drift problem does not exist. The gyroscope is seldom used alone and is usually used to complement the accelerometer and the magnetometer to account for dynamic motions. With information on the orientation of the body segment together with knowledge of the segment length and joint characteristics, relative positions of the body segments can be estimated. In integrating the inertial and magnetic sensors, the high power consumption of the gyroscope and the higher costs can be a drawback in cost and power sensitive applications. In addition, the problem of estimating the external acceleration from the gravity vector associated with the accelerometer and the problem of magnetic disturbances on the magnetometer still remain. The use of other technologies such as optical or ultrasonic sensors together with inertial/ magnetic sensors have been investigated to further improve the measurement accuracy. These hybrid methods though also bring forth problems associated with the technologies such as occlusion from optical sensors and multipath from ultrasonic sensors. The challenge in existing and future research work lies in an appropriate sensor fusion algorithm to complement the output from different sensors and address the associated problems.

In comparing the different approaches, an accelerometer approach for orientation determination is low in cost and power consumption. This makes it suitable for long term monitoring of human motion. In Chapter 3, the development of a wearable wireless sensor network based on triaxial accelerometer is described. The algorithms for tilt and orientation determination using the accelerometer is discussed in Chapter 4. An approach based on a single angle-axis quaternion is also presented for the determination of the orientation of the articulated human arm (upperarm and forearm) along a general plane.

Most of the works using inertial/ magnetic sensors are on the determination of

the absolute orientation of a single arm limb rather than the relative orientations between arm limbs. The main reason for this is if the algorithm allows for three degrees of freedom orientation determination, each limb segment can then be considered independently and the use of an articulated arm limb model is not required [17]. The use of the articulated arm model though has been used to address some of the limitations of the inertial sensors presented in the previous sections. The kinematic arm model has been used together with the length of the arm limb as a constraint to prevent the drifting in position estimates obtained [20, 66, 72]. The range of the flexion/extension and pronation/ supination of the elbow were also incorporated in a constraint in [40] to reduce the drift in the use of the gyroscope. The minimization of the abduction/adduction of the elbow joint was also used to compensate for the drift in heading as a result of using the gyroscope [39, 65]. For the use of the accelerometer alone though, orientation measurement is limited to two degrees as it cannot resolve rotations about the gravity axis, limiting measurement to half a 2D vertical plane. To address this limitation, the concept of a factorized quaternion approach as described in Kuipers [71] has been proposed in Chapter 5 to extend measurement of the forearm by making use of information on the orientation of the upperarm and to resolve any transient singularities associated with the use of the accelerometer. The use of the anatomical arm constraint in restricting the abduction/adduction of the elbow joint is also inherently incorporated with the problem formulation using factorized quaternions without the need for an additional constraint. Anatomical constraints adhering to the range of both the upperarm and forearm are incorporated to reduce the ambiguity in solutions.

Since the accelerometer is unable to determine rotations about the vertical and measure dynamic changes in orientation, a new proposed sensor fusion algorithm is also described in Chapter 6 to integrate information from the accelerometer

with an additional gyroscope and magnetometer. In contrast with the work presented on the use of Euler angles or quaternions, the new algorithm is based on elevation and heading angles which are visually intuitive and are independent on the temporal order of rotations. In addition, the proposed sensor fusion algorithm approaches the problem of magnetic disturbances in the monitoring environment by using magnetometer readings solely for the determination of heading information. The presence of magnetic disturbances thus affects only the accuracy of the heading angle and not the elevation angles. In addition, the gyroscope reading is used to estimate the external acceleration of the accelerometer by considering the kinematics of the arm motion. This external acceleration is then offset from the accelerometer reading in order to determine the gravity vector used for the estimation of elevation angles. A novel singularity avoidance strategy is also proposed to allow measurements through all possible orientations.

TABLE 2.1
USE OF INERTIAL/MAGNETIC SENSORS IN RELEVANT RESEARCH

	Features/ Advantages	Limitations/ Challenges	Relevant Work
Accelerometer	• Measurement of static 2DOF orientation • Low cost • Low power consumption	• Inability to determine rotation about vertical • Inability to measure dynamic changes in orientation • Time integration of bias leads to drift for position and velocity estimates	[27, 33, 34, 36]
Accelerometer & Gyroscope	• Measurement of dynamic 2DOF orientation • Drift in time integration of angular rate can be arrested in the Euler pitch and roll axes	• Drift in time integration of angular rate remains for rotation about vertical axis • High power consumption and cost of gyroscope	[37–40]
Accelerometer & Magnetometer	• Measurement of static 3DOF orientation • Relatively low cost	• Inability to measure dynamic changes in orientations • Magnetic disturbances from environment	[14, 41, 43, 44]
Accelerometer & Gyroscope & Magnetometer	• Measurement of dynamic 3DOF orientation	• Estimation of external acceleration from gravity • Magnetic disturbances from environment • Higher cost of sensors integration and data fusion • High power consumption of multiple sensors	[15–17, 49, 51, 53–65]

CHAPTER 3

Development of Wearable Wireless Sensor Network

3.1 Introduction

In Chapter 2, the use of the inertial/ magnetic sensors for measuring the human body motion in recent research work has been described. As mentioned, the development of micromachined system technology has made such sensors lighter, smaller and cheaper. Inertial/magnetic tracking is source-free unlike ultrasonic or magnetic systems which requires a transmission source. The approach also requires no light of sight as with visual tracking. There is no inherent latency and all latency are due to data processing and transmission. Many of the systems utilizing inertial/magnetic sensors at the initial time of this research work have wiring which poses a constraint on the body movement. As such, a wearable wireless sensor network based on inertial/magnetic sensors for the measurement of human body motion has been proposed to overcome these limitations. In this chapter, the development of the wearable wireless sensor network is presented. The configuration of the system is first described followed by the selection of the wireless standard and protocol in its design. The procedure for estimating the latency of the wireless measurement system is also explained for a single-node and multiple-node sensor network. This is followed by a description of an accurate calibration procedure for the triaxial accelerometer utilizing a precision rotary stage.

Wireless sensor network is a promising field that integrates sensor technologies, embedded system and wireless communication together to produce a low cost, low power and reliable system capable of monitoring specific events. A typical sensor network consists of a number of tiny, often battery powered computing devices scattered throughout a physical environment [18]. Each device is capable of sensing and/or actuating. It is generally applied in monitoring applications with non-critical data, where longer latency is not a critical issue. Such applications usually do not need high data throughput but emphasize on power saving to maximize battery life. It has been used in a variety of applications including commercial and industrial monitoring, home automation, consumer electronics, personal computer peripherals, home security, personal healthcare, games, automotive, agriculture etc [73].

The use of a wireless sensor network with inertial sensors for body motion tracking has the following advantages:

- The wireless feature enables unrestrained motion of the human body as opposed to a wired monitoring device, allowing more natural movements to be tracked.
- The subject is able to move freely in a home or office environment where wireless sensor nodes are deployed in a star or clustered tree network configuration. It overcomes the limitations of conventional systems which require the subject to be tied physically by wires to a desktop datalogger or personal computer.
- The small form factor and lightweight feature of the sensor nodes allow for easy attachment to different parts of the human body such as arm limbs, legs, thighs and sternum.
- The autonomous computing capability of each sensor node allows for distributed control architecture to be implemented.
- It is low in cost as compared to a visual tracking system with multiple

cameras.

- The low power consumption of each sensor node allows for long term monitoring.

3.2 System Configuration

In this research, a wearable wireless sensor network system equipped with inertial/magnetic sensors has been developed for monitoring patients undergoing rehabilitation in their home/ office environment. Fig. 3.1 shows the configuration of the system. It consists of a number of sensor nodes functioning as end devices that can communicate wirelessly either directly or via a coordinator to a central Personal Area Network (PAN) coordinator in a star/ cluster tree network topology. The PAN coordinator is in turn connected to a personal computer via a RS232 wired link. Fig. 3.2 shows a coordinator with a PIC18LF2620 microcontroller. The coordinator may use either a mains power or a 9V battery.

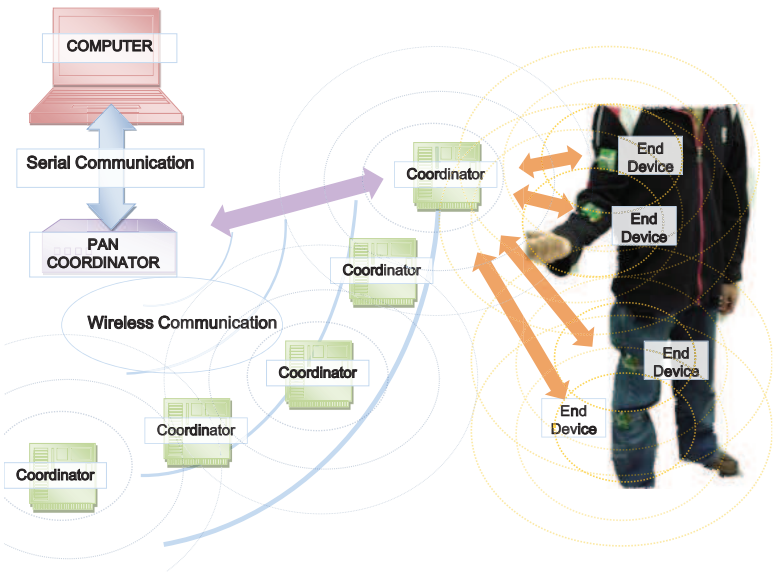

Figure 3.1. General configuration of system

Fig. 3.3 shows the picture of an initial prototype sensor node. The first prototype sensor node is equipped with a capacitive micromachined accelerometer (Freescale MMA7261QT) that can be used to detect tilt angle of up to 3 axes. (A

second prototype sensor node including an additional gyroscope and magnetometer is developed in 2010 and its specifications and use will be described in Section 6.3.) The sensor nodes are attached to the human limbs and operate completely untethered as shown in Fig 3.1. They are powered by a 3.6V rechargeable battery. The developed sensor node has a small form factor measuring 40 × 39 × 16 mm. It weighs only 19g without battery. The battery will add another 14g to the system. For the wireless communication, both the sensor node and coordinator use the Microchip 2.4 GHz RF transceiver MRF24J40 and an onboard PCB trace antenna that has a communication range of 10-50 metres.

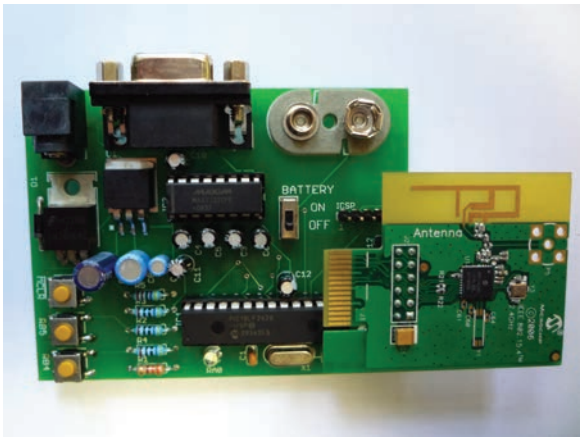

Figure 3.2. Photograph of a network coordinator

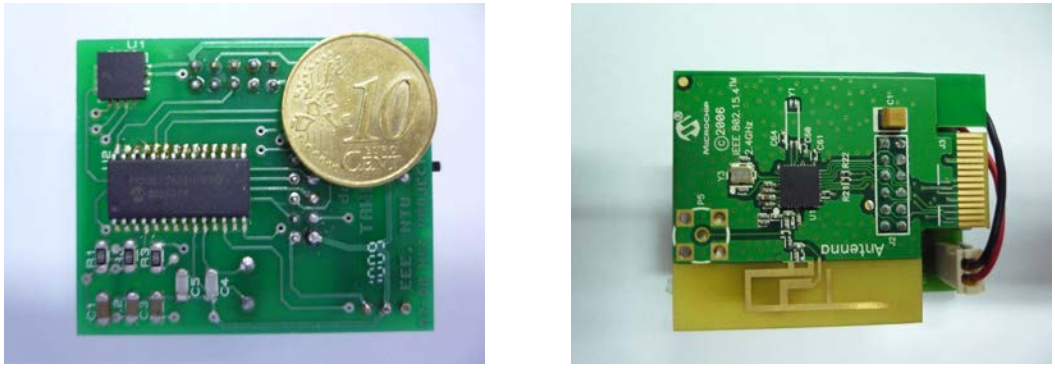

(a) (b)

Figure 3.3. Photographs of sensor node. (a) Front view, with a microcontroller unit and an accelerometer. (b) Back view, with Microchip's RF module

During operation, the accelerometer on each sensor node will measure the 3-axis (XYZ) acceleration. These measurements are then digitized via the built-in analog-to-digital converter (ADC) of the microcontroller and transmitted wirelessly using the RF transceiver to the network coordinator. The sampling rate for the ADC is configurable and is set to 10 Hz for a two-sensor node network system. The coordinator subsequently transfers the data to the personal computer (PC) via RS232 interface at a baud rate of 19200 bps for algorithmic computation and motion rendering. The MATLAB virtual reality toolbox is used for the motion rendering.

3.2.1 Selection of Wireless Standard

Two competing wireless standards, namely the Bluetooth (IEEE Standard 802.15.1) and IEEE 802.15.4, are possible candidates for our application. A summary is given in Table 3.1. From Table 3.1, the Bluetooth is superior in terms of data latency as it offers a higher data rate of 3Mbps instead of 250kps from the IEEE 802.15.4. However, this is achieved at an expense of higher power consumption and larger form factor. Even though the IEEE 802.15.4 offers a lower data rate, it is sufficient for the intended rehabilitation application. In addition, its low power solution is more suited for long term body motion monitoring. Thus the IEEE 802.15.4 is selected in the design of the prototype development.

3.2.2 Wireless Protocol

For the wireless networking protocol, the MiWi^{TM} protocol [74] from Microchip was chosen due to its small stack size. MiWi^{TM} is a proprietary protocol stack similar to the ZigBee in that both are based on the medium access control (MAC) and physical (PHY) layers of the IEEE 802.15.4 specification. The MiWi^{TM} aims at smaller applications that have relatively small network sizes, with few hops

TABLE 3.1
COMPARISON BETWEEN BLUETOOTH AND IEEE 802.15.4

	Bluetooth/IEEE 802.1.51™	**IEEE 802.15.4™**
Range	∼10 m (class 2) ∼100 m (class 3)	∼10 m
Data Rate	3 Mbps with EDR	≤ 250 kbps
Operating Frequency Band	2.4 GHz	868 MHz, 915 MHz and 2.4 GHz
Power Consumption	Low (typical current consumption of Tx 50mA)	Ultra Low (typical current consumption of Tx 20mA)
Size	Small (used in portable devices such as PC cards in laptops/ handphones/ PDAs)	Very Small (typically used in wireless sensor nodes/ stick on sensors)
Cost/ Complexity	Low (1)	Very Low (0.2)

between nodes and offers an alternative for applications that do not need inter-operability with other ZigBee devices. In addition, no certification is required for commercialization of the wireless sensor networks utilizing the MiWi™ networking protocol. Table 3.2 shows a comparison between MiWi™ and ZigBee.

TABLE 3.2
COMPARISON BETWEEN MIWI™ AND ZIGBEE PROTOCOL STACK

	MiWi™	**ZigBee**
IEEE Standard	802.15.4	802.15.4
Data Rate	250kbps @ 2.4 GHz	250kbps @ 2.4 GHz
Topography	Star/ Cluster-Tree/ Mesh	Star/Cluster-Tree/ Mesh
Hops	4	Infinite
Memory	7 KB - 17 KB	40 KB - 96 KB
Max Nodes	1024	65 536

MiWi™ supports a maximum of 1024 nodes on a network and a data rate of up to 250 kbps. Each coordinator is capable of having 127 children nodes, with a

maximum of 8 coordinators in a network. Packets can travel a maximum of 4 hops in the network and 2 hops maximum from the PAN coordinator. For a wearable sensor network which comprises of a small number of sensor nodes (in the range of $2 \sim 30$), the MiWi protocol is sufficient for the application needs.

3.3 Latency

The latency of a tracking system can be defined as the time (delay) between the motion is made and the time the motion is captured. In an ideal tracking system, the mean time delay after a motion is initiated until the corresponding data is transmitted should be less than 1 ms [8]. Moreover, the latency between the initiation of motion and the motion rendering should be less than 100 ms to avoid degradation of performance [75]. The use of a wireless system as opposed to a hardwired system implies a tradeoff of unhindered body motions for fast reliable data transmission. Thus, one of the challenges of the proposed wireless tracking system in this thesis is to ensure acceptable latency when multiple sensor nodes are in use.

To estimate the latency of the system, the main measurable time components contributing to the latency of the system with one sensor node is depicted in Fig. 3.4. The sampling interval, T_s, should be greater than the sum of the total latencies T_l. Thus, the latency of the system limits its maximum sampling rate. Given that the frequency spectrum of human body motion ranges from 2 to 20 Hz [76], the sampling rate of the system should ideally be greater than 40 Hz. For the case of arm flexion and extension motion, the FFT of the accelerometer signal mounted on a forearm undergoing normal and very fast flexion and extension motion shows that the majority of the frequency components fall under 1.0 Hz. Thus, a sampling frequency of 10 Hz is more than sufficient. From Fig. 3.4, the time components are related by

$$T_s \geq T_l = T_{pn} + T_{dr} + T_{pc} + T_{ds} + T_{ps} \tag{3.1}$$

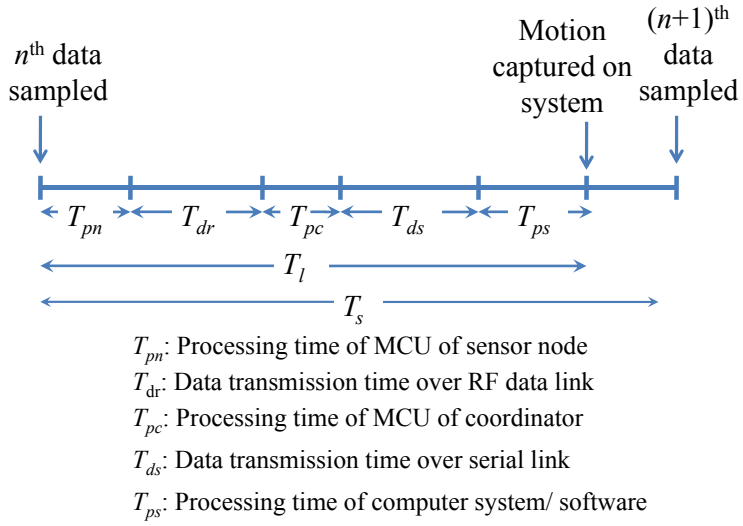

Figure 3.4. Latencies involved in the sample processing of real-time motion tracking (single node)

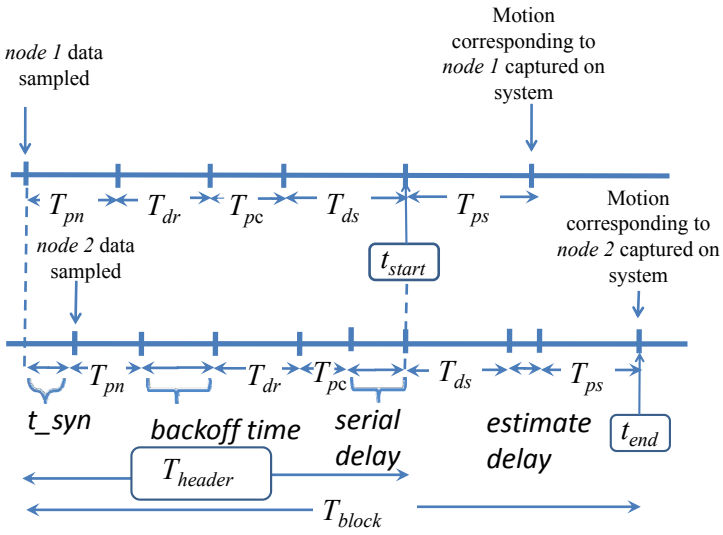

Figure 3.5. Latencies involved with two sensor nodes

Fig. 3.5 shows the latency of a network with two sensor nodes and one coordinator. With multiple nodes, the figure shows that there are additional delays such as the time difference between different sensor measurements (t_syn), backoff time, serial and estimate (delay) etc. In this case, the sampling rate has to be

greater than the latency of the system as below:

$$T_s \geq T_{block} \tag{3.2}$$

3.4 Calibration of Accelerometer

To improve the measurement accuracy, calibration is required to obtain the 0g offset values (λ_{Y_o} and λ_{Z_o}) for each accelerometer. One approach is to determine the ADC output when the accelerometer is at the 0g level position. However, such measurement is prone to error. Calibration can also be conducted by recording the ADC values during freefall. However, inaccuracies could arise due to unwanted rotation of the device during freefall.

From (4.13), the ADC values can be rewritten using (4.9)–(4.10) and (4.12) to give

$$\lambda_Y = Q\left[S_A g \sin\theta + \lambda_{Yo}\right] \tag{3.3}$$

$$\lambda_Z = Q\left[S_A g \cos\theta + \lambda_{Zo}\right] \tag{3.4}$$

where θ is the tilt angle and $S_A = \frac{2^n}{V^+{}_{REF} - V^-{}_{REF}} S$ is the sensitivity of the accelerometer (ADC bits/g).

From the sinusoidal relationship of λ_Y and λ_Z with respect to the tilt angle θ, it is observed that an estimate of λ_{Y_o} and λ_{Z_o} can be determined by taking the mean value of λ_Y and λ_Z over a 360° cycle. This method yields accurate result and requires no reference acceleration position that is difficult to determine in practice.

For calibration, the sensor node is mounted on a rotary stage as shown in Fig. 3.6. The rotary stage uses two ceramic motors. It has a resolution of 0.0001° and a maximum allowable velocity of 250 mm/s. Fig. 3.7 shows the experimental ADC values of the Y and Z axis of the accelerometer from 0° to 360° with a

step size of 5°. From the figure, it is observed that the ADC values for the $Y$and Z-axis follow a sine and cosine wave as in (3.3) and (3.4) respectively. The corresponding estimated 0g offsets, $\tilde{\lambda}_Y$ and $\tilde{\lambda}_Z$, are determined to be 127.8889° and 125.9306° respectively. This calibration can be repeated for the X-axis or another accelerometer as shown in Fig. 3.8–3.9.

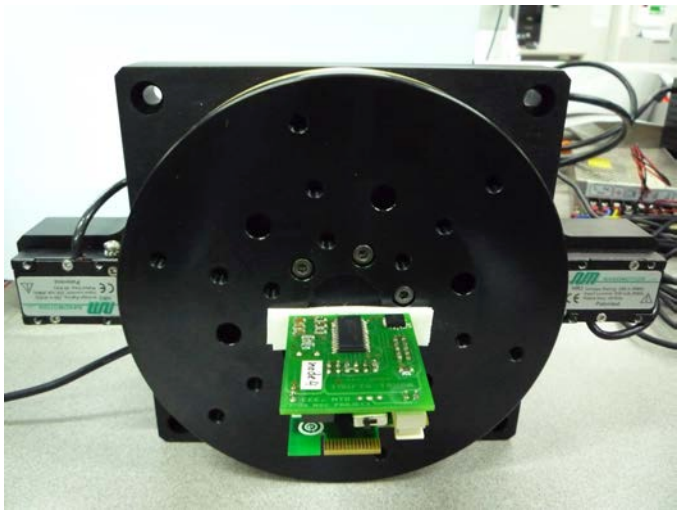

Figure 3.6. Mounting of a sensor node on a high precision rotary motor for determination of angular displacement

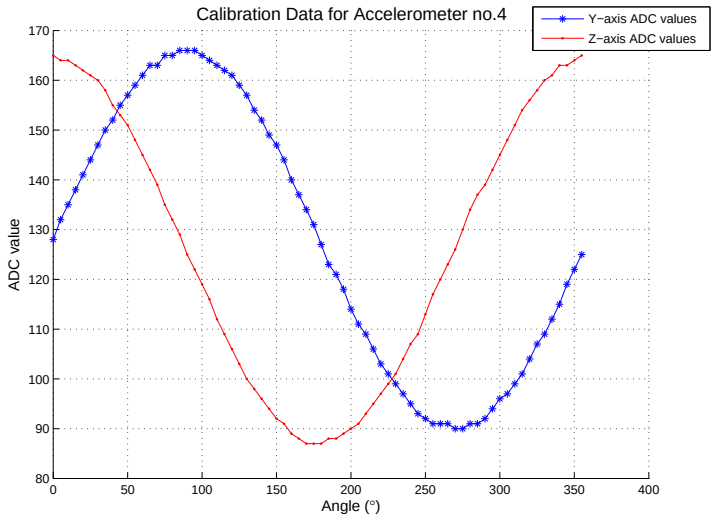

Figure 3.7. Calibration Data of a Typical Accelerometer (node id 4)

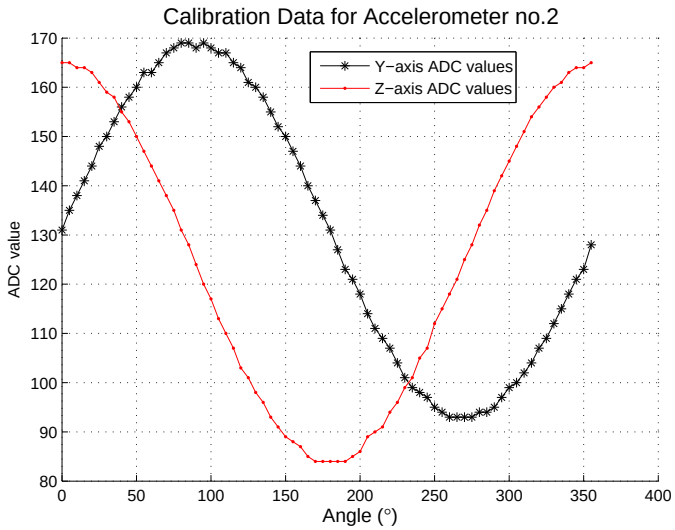

Figure 3.8. Calibration Data of Y-Z axes of Accelerometer (node id 2)

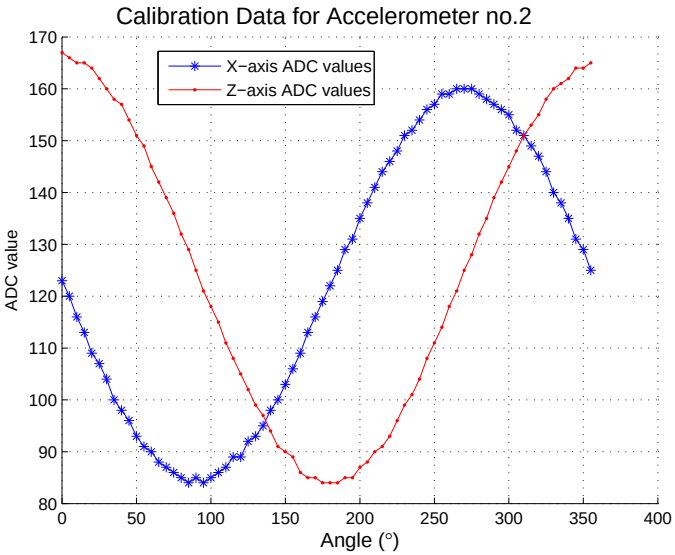

Figure 3.9. Calibration Data of X-Z axes of Accelerometer (node id 2)

3.5 Summary

In this chapter, the design and system implementation of a wearable wireless sensor network for tracking the human arm motion has been presented. Compared to other approaches based on transmission sources or visual tracking, the system developed is portable and easy to use. This system can be used for a rehabilitation application, in which a patient can be monitored without restraint and rehabilitation can be carried out in a home environment instead of a specialized laboratory in the hospital. Compared to a wired system with reliable data transmission, the data rate of wireless transmission of data is typically lower and is subjected to challenges such as loss of data packets due to fading and RF interference and contention of channel to avoid data collision. As such, a methodology is also described in this chapter to determine the latency of the wireless tracking system to ensure that it is acceptable when multiple sensor nodes are in use. In addition, to improve measurement accuracy, a calibration procedure is also described to determine an accurate 0g offset for the triaxial accelerometer using a precision rotary stage. In the next chapter, a tilt determination algorithm based on the triaxial accelerometer is described. The performance of the developed wearable wireless system is then evaluated in terms of accuracy, latency and power consumption.

CHAPTER 4

Accelerometer Based Upper Limb Measurements

4.1 Introduction

In Chapter 2, the use of the MEMS accelerometer for measuring the human body motion in relevant research work has been described. In Chapter 3, wearable wireless sensor nodes developed utilizing triaxial accelerometers were presented. The use of these miniature accelerometers offers a practical and low cost method to monitor human movements objectively. In addition, the low power consumption of these accelerometers has particular applicability to monitor free-living subjects over a long term [77]. By attaching an accelerometer to a human limb, the angle of the limb with respect to the vertical axis can be found. In this chapter, the determination of tilt information with a single degree of freedom is first presented. The performance of the developed wearable wireless system implementing the tilt measurement algorithm is evaluated experimentally under a set of common benchmarks for a motion tracking system, namely accuracy, latency and power consumption.

Measurement of the arm limb's orientation is then extended to two degrees of freedom. Two methods based on Euler angles are presented; one using rotation matrices and the other based on the method of quaternions. The problem of a single limb orientation is then extended to the determination of the orientation of the articulated human arm limb, i.e the upperarm and forearm. An approach

based on the use of a single angle-axis quaternion to describe the orientation of each limb is investigated. The performance of this approach is evaluated using numerical simulations and the results are presented at the end of this chapter.

4.2 Biomechanics of the Human Arm

In studying the human arm motion, it is useful to review the biomechanics of the human arm and the terminology used in describing the arm motions. This information will be used in the remaining part of this thesis. The universally used method of describing human movements is based on a system of planes [78]. As illustrated in Fig. 4.1, three imaginary cardinal planes are positioned through the body intersecting at right angles. The sagittal plane divides the body into left and right halves; the frontal plane divides the body into front and back; and the transverse plane divides the body into top and bottom. Fig. 4.1 also shows the human body in the anatomical position, which is commonly used as a standard reference point to describe joint movements.

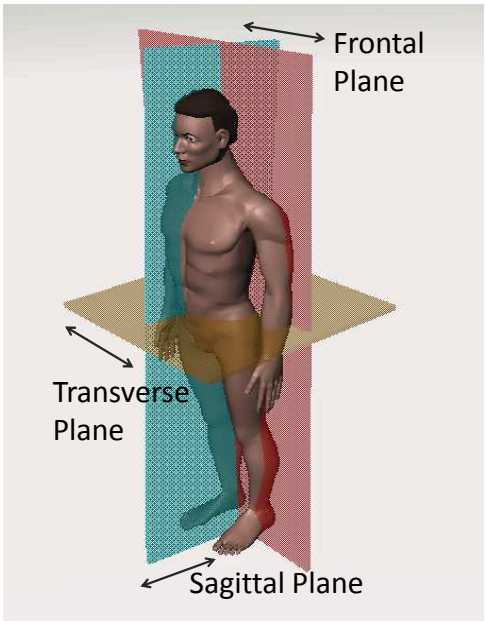

Figure 4.1. Planes on the human body which originate at the centre of gravity

There are six basic movements associated with the arm and they are shown in

Fig. 4.2. The first two movements are flexion and extension of the arm which occur along the sagittal plane and are commonly used for lifting actions. Abduction and adduction are a pair of movements that occur along the frontal plane. These movements are commonly used to maintain stability and balance. The last two movements are medial and lateral rotations which occur along the transverse plane and they are used commonly for throwing. There are also specialized types of movements associated with the arm. These specialized movements are essentially among the six basic movements. For example, the forearm can perform a pair of specialized movements known as supination and pronation. For the arm, it can also perform a combination of flexion and adduction known as horizontal adduction as well as a combination of extension and abduction known as horizontal abduction.

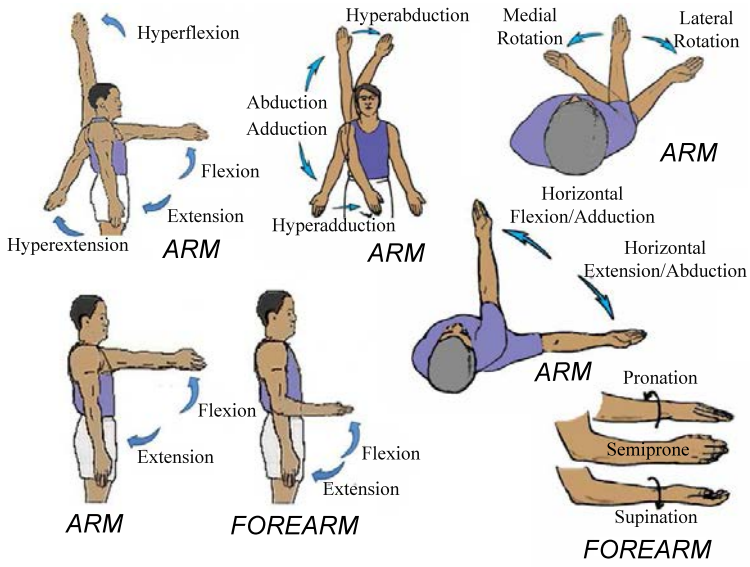

Figure 4.2. Different types of basic and specialized arm movements [78]

Fig. 4.3 shows the attachment of the developed accelerometer based sensor nodes described in Chapter 3 onto the upperarm and the forearm. The figure also shows the corresponding movements of the arm rendered in a virtual reality environment on the computer screen. Since the accelerometer is unable to determine the heading information, the movement of the human arm is investigated

along the sagittal plane, i.e. the plane that bisects the human body into left and right [78]. In general, the plane of motion can be chosen to be any vertical plane. The sagittal plane is chosen in this thesis since most planar analysis is concerned with motion in the sagittal plane.

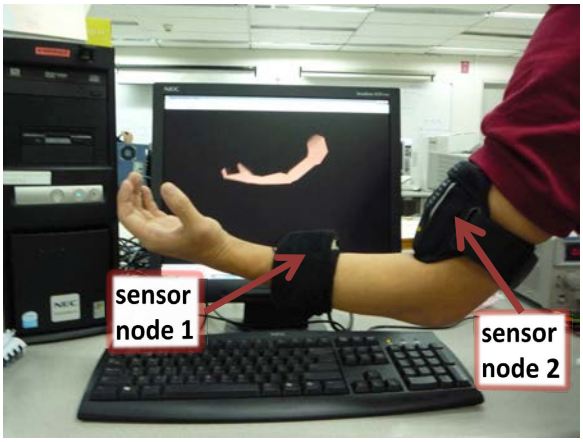

Figure 4.3. Attachment of accelerometer based sensor nodes on the human arm developed in this research

4.3 Measurement in a Single Degree of Freedom

MEMS accelerometers were first made available in the mid-1990s. They were single axis and could only measure acceleration along a single direction. Dual axes accelerometer came into the market in the early 2000s. It was only after 2005 that tri-axial accelerometers became available, alleviating the need for multiple devices. Much of the early work uses the accelerometer as an inclinometer for tilt determination with a single degree of freedom in a 2D plane. For the sagittal plane, this commonly corresponds to measurement of the flexion and extension movements of the forearm and the upperarm. Flexion is a bending movement in which the relative angle of the joint between the adjacent segments decreases. Extension is a straightening movement in which the relative angle of the joint between two adjacent segment increases as the joint returns to the reference anatomical position. For the physical therapist, the range of flexion/extension motion of the elbow and

shoulder joint of the patient is of particular interest for monitoring the rehabilitation progress. In this section, tilt measurement in a static condition where the arm is stationary is first examined, followed by tilt measurement under dynamic conditions where the arm is moving as measurement is taking place.

4.3.1 Principle of Operation of Accelerometer

To understand what an accelerometer actually measures, it is useful to first understand the principle of the accelerometer's operation. Fig 4.4 shows a simplified model of the accelerometer. An accelerometer is designed to measure the force required to maintain a proof mass within the accelerometer case. For an elementary linear accelerometer, the proof mass is suspended in the case by restoring springs that deflects in proportion to the force applied to the proof mass. This deflection is sensed by a transducer circuit and converted to the accelerometer output.

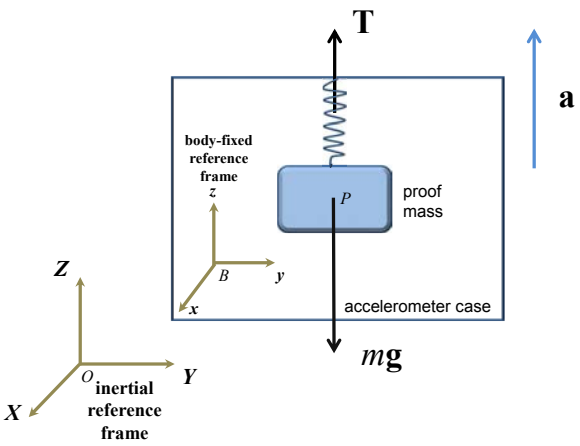

Figure 4.4. Simplified Accelerometer Model

In Fig. 4.4, **T** represents the tension vector of the restoring springs connecting the proof mass to the accelerometer case which is proportional to the accelerometer output by the mass of the proof mass, m. **g** is the gravity vector given by

$$\mathbf{g} = \begin{pmatrix} 0 \\ 0 \\ -g \end{pmatrix} \tag{4.1}$$

where g is the magnitude of the acceleration due to gravity and $\mathbf{a}$ is the acceleration vector of the accelerometer case relative to the inertial reference frame with origin O. A reference frame is said to be inertial if it can be used to apply Newton's second law of motion in the form of $\sum \mathbf{F} = m\mathbf{a}$, i.e. the sum of external forces, $\mathbf{F}$, on any object is equal to the product of the mass and the acceleration of its centre of mass [79]. The body-fixed reference frame with origin B which is also shown in Fig 4.4 is fixed with respect to the accelerometer casing and moves with the accelerometer. For a reference frame that rotate or accelerates relative to an inertial frame, Newton's second law can only be applied by carefully accounting for the acceleration and rotation. For the proof mass, Newton's second law can be applied as:

$$\sum \mathbf{F} = m\mathbf{a}_P \tag{4.2}$$

where $\mathbf{a}_P$ is the acceleration of the proof mass with respect to the fixed reference frame. $\mathbf{a}_P$ can be expressed in terms of the proof mass's acceleration relative to the body-fixed reference frame $\mathbf{a}_{P/B}$ and the acceleration of the origin of the body-fixed reference frame $\mathbf{a}_B$ by

$$\mathbf{a}_P = \mathbf{a}_B + \mathbf{a}_{P/B} \tag{4.3}$$

Taking into account the external forces acting on the proof mass, (4.2) can thus be written in the form given by

$$\mathbf{T} + m\mathbf{g} - m\mathbf{a}_B = m\mathbf{a}_{P/B} \tag{4.4}$$

which is Newton's second law expressed in terms of the body-fixed reference

frame moving relative to the inertial primary reference frame. If the output of the accelerometer, $\mathbf{u}_a$, is proportional to the tension vector by $\mathbf{u}_a = \mathbf{T}/m$, (4.4) can be expressed in terms of the accelerometer output and accelerations by

$$\mathbf{u}_a + \mathbf{g} - \mathbf{a}_B = \mathbf{a}_{P/B} \tag{4.5}$$

Since the proof mass is constrained by the restoring springs and is not moving relative to the accelerometer case, the value of $\mathbf{a}_{P/B}$ is zero. In addition, if the acceleration of the origin of the body-fixed reference frame is equal to that of the accelerometer, i.e. $\mathbf{a} = \mathbf{a}_B$, the general expression for the output of the accelerometer is then given by

$$\mathbf{u}_a = \mathbf{a} - \mathbf{g} \tag{4.6}$$

which means that the accelerometer actually measures the acceleration of the accelerometer minus the gravitational acceleration. This explains why a gravitational field component aligned with the same sensor axis direction will result in a negative accelerometer reading of $-1g$. A sensor axis positioned upwards will have an accelerometer reading of $+1g$.

In applications for measuring the earth's gravitational field, a convention sometimes adopted is for the accelerometer output to have a value of $+1g$ in an axis direction aligned with the direction of the earth's gravity field pointing downwards. In this case, the accelerometer's axes are defined such that the output and accelerations are given by

$$\mathbf{u}_a - \mathbf{g} + \mathbf{a}_B = -\mathbf{a}_{P/B} \tag{4.7}$$

and the general expression for the accelerometer output is

$$\mathbf{u}_a = \mathbf{g} - \mathbf{a} \tag{4.8}$$

In Chapter 4 and 5 of this thesis where the focus is on the measurement of the gravity vector and $\mathbf{u}_a \cong \mathbf{g}$, the direction of the accelerometer axes and its output are defined as in (4.7) – (4.8). In Chapter 6 where the estimation of the external acceleration of the accelerometer is performed, the direction of the accelerometer axes and its output as in (4.5)–(4.6) will be used. In general, the use of either convention is acceptable and the choice should be inferable from the context if not explicitly specified.

4.3.2 Static/ Tilt measurement

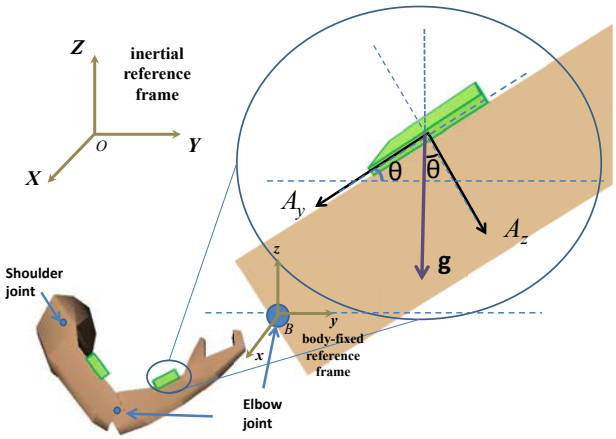

Figure 4.5. Static tilt angle measurement in the Y-Z plane

Fig. 4.5 shows an accelerometer mounted on the forearm. In the static condition where the arm is not moving, the acceleration of the accelerometer can be taken to be zero in (4.8). The tilt angle θ of the accelerometer can thus be determined from the accelerometer output which gives the component of the acceleration due to the gravity g. Using (4.8), the accelerometer output, A_Y in the Y-axis and A_Z in the Z-axis can be determined as:

$$A_Y = g \sin\theta \tag{4.9}$$

$$A_Z = g \cos\theta \tag{4.10}$$

From (4.9) and (4.10) the tilt angle can be determined as:

$$\theta = \tan^{-1}\frac{A_Y}{A_Z} \tag{4.11}$$

The quadrant of θ can be determined using the sign of A_Y.

The output voltage, V_{out}, of the accelerometer is related to the accelerometer output, A_i, of a particular axis ($i = Y$ or Z) by the following relationship

$$V_{\text{out}} = V_{\text{offset}} + S \times A_i \tag{4.12}$$

where $S = \Delta V/\Delta g$ is the sensitivity of the accelerometer in $V/(ms^{-2})$ and V_{offset} is the offset of the accelerometer at $0g$. The corresponding ADC value can be expressed as

$$\lambda_i = Q\left[\frac{2^n}{V_{REF}^+ - V_{REF}^-}V_{out}\right] \tag{4.13}$$

where n is the resolution of the ADC ($n = 8$ in this case) and V_{REF}^+ and V_{REF}^- are the reference voltage levels and $Q[\ ]$ is the quantizer function. The accelerometer is ratiometric, i.e. the output voltage and sensitivity scale linearly with the reference voltage. From (4.12) and (4.13), it is observed that the supply induced errors are cancelled in the analog to digital conversion process.

Substituting V_{out} from (4.12) into (4.13), the accelerometer output A_i is approximately proportional to λ_i after subtracting an equivalent ADC offset. As such, (4.11) can be rewritten as follows:

$$\theta = \tan^{-1}\frac{\lambda_Y - \lambda_{Yo}}{\lambda_Z - \lambda_{Zo}} \tag{4.14}$$

where λ_Y and λ_Z are the ADC output values of the accelerometer in the Y and Z axis respectively, and λ_{Yo} and λ_{Zo} are the offsets of the accelerometer at $0g$.

4.3.3 Dynamic Measurement

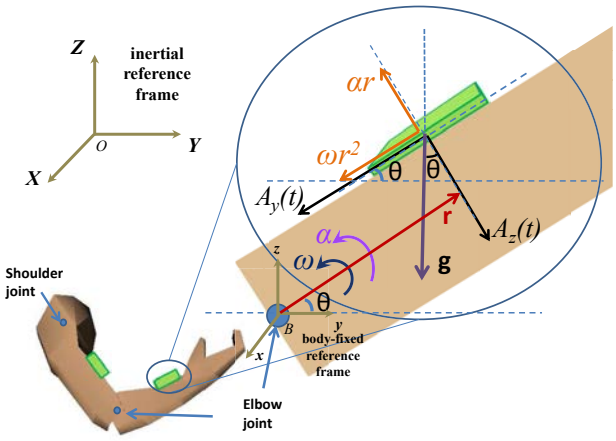

Figure 4.6. Dynamic tilt angle measurement in the Y-Z plane

In the dynamic condition, the rotation of the accelerometer can be modelled as a circular motion as shown in Fig. 4.6. It should be noted that the origin of the body-fixed reference frame, B, is taken to correspond to that of the centre of the rotation of the arm limb. Using (4.7) and assuming that the acceleration of the centre of rotation is zero, i.e. ($\mathbf{a}_B = \mathbf{0}$), the following expressions can be obtained for the time-changing accelerometer outputs $A_Y(t)$ and $A_Z(t)$ in the Y and Z-axes

$$A_Y(t) - g\sin\theta = -a_Y \tag{4.15}$$

$$A_Z(t) - g\cos\theta = -a_Z \tag{4.16}$$

where a_Y and a_Z are the accelerations in the directions of Y and the Z-axis of the accelerometer respectively. The distance from the centre of mass of the accelerometer to the centre of rotation (elbow joint in this case) is given by the vector $\mathbf{r}$. In planar circular motion [79], the tangential component of acceleration is given by the product of the angular acceleration, α, and the magnitude of the distance vector r. The normal component of acceleration is given by the product

of the square of the magnitude of the angular velocity, ω, and the magnitude of the distance vector r. As such, (4.15) and (4.16) can be expressed as

$$A_Y(t) - g\sin\theta = -r\omega^2 = -r\left(\frac{d\theta}{dt}\right)^2 \tag{4.17}$$

$$A_Z(t) - g\cos\theta = r\alpha = r\frac{d^2\theta}{dt^2} \tag{4.18}$$

Rearranging (4.17)–(4.18) produces

$$A_Y(t) = g\sin\theta - r\left(\frac{d\theta}{dt}\right)^2 \tag{4.19}$$

$$A_Z(t) = g\cos\theta + r\frac{d^2\theta}{dt^2} \tag{4.20}$$

From (4.19) and (4.20), it is observed that $A_Y(t)$ is affected by the angular velocity while $A_Z(t)$ is affected by the angular acceleration. Equations (4.19) and (4.20) are non-linear in nature and a solution is non-trivial. In applications such as rehabilitation where the arm motion is slow, the angular acceleration and velocity of the human arm motion are generally small. The maximum angular velocity of the arm for a patient undergoing rehabilitation is about 10 $^\circ/s$ or 0.17 rad/s [80]. For the angular acceleration, it is typically less than 1 rad/s^2 for most of the time during arm flexion and extension motion [81]. With $r = 0.15$ m, these translate to an additional acceleration of 0.0043 m/s^2 in the Y-axis and 0.15 m/s^2 in the Z-axis which are much less than the acceleration due to gravity (9.81 m/s^2). In addition, it is observed that the derivative terms are also multiplied by r. This suggests that the effects of the additional derivative terms can be minimized by placing the sensor close to the centre of rotation. Hence, the derivative terms can be neglected when determining the tilt angle. The error due to this assumption will be determined through experiments described in Section 4.4 by subjecting the sensor to varying angular rates of rotation.

4.4 Experimental Evaluation

4.4.1 Accuracy

To investigate the accuracy of the tilt measurement approach in Section 4.3, the sensor node is first mounted on a rotary stage as shown in Fig. 3.6. The stage is programmed to produce a swinging motion between $\pm 90°$ with an angular speed varied from $10°/s$ to $190°/s$. This emulates the arm swinging at different rates. The ADC accelerometer reading with respect to time is captured. Fig. 4.7 shows the mean error and variances of the angle of rotation. From the experimental results, it is observed that the mean error is close to 0° at very low speeds of oscillation ($\leq$ 20°/s). The mean error fluctuates between 0.5° and 1.0° for increasing speeds of oscillation. The standard deviation on the other hand shows an increasing trend from 2° to 3.7°. This is due to the effect of neglecting the additional acceleration term besides the gravity in (4.19)–(4.20). From this test, it is concluded that an accuracy of 0.52 ° is achievable.

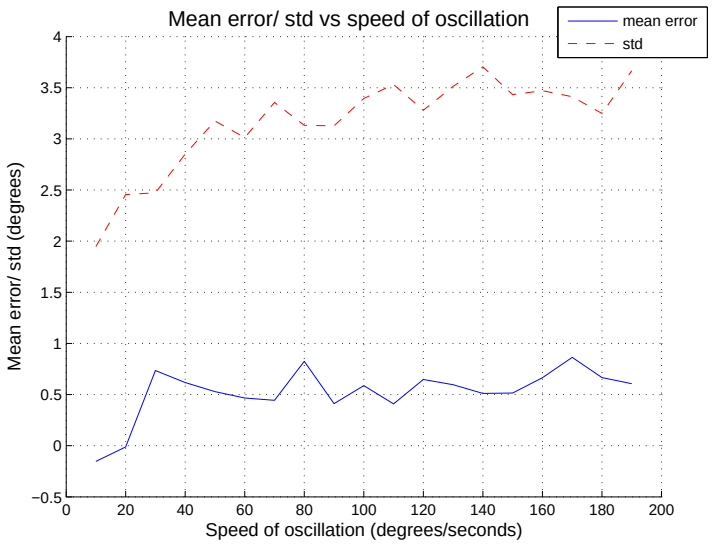

Figure 4.7. Mean error and variance of accelerometer readings at different speeds of oscillation

4.4.2 Latency of Sensor Node

To estimate the latency of the system, 10,000 data samples have been collected from experiment based on one sensor node and one coordinator. The PC used in the experiments runs on a Pentium IV 640 CPU with a clock speed of 3.2 GHz. As shown in Fig. 3.4, the latencies to be considered are the processing time of the sensor node T_{pn}, the processing time of the coordinator T_{pc} and the processing time of the computer T_{ps} in computing the rotation angle. These latency times can be determined using the timer module of the microcontroller and the CPU clock in PC. The data transmission time of the RF data link, T_{dr}, and the data transmission time over the serial link, T_{ds} can be calculated using the RF data rate and serial link baud rate. For this system, the data rate and baud rate are 250 kbps and 19.2 kbps respectively. The data propagation time over air can be neglected since the RF signal is transmitting at 3×10^8 m/s and the time over the typical distances (10 - 50m) is insignificant. The mean value of total latency time T_l obtained from this experiment is shown in Table 4.1.

From Table 4.1, the processing time of the PC is much greater than the coordinator and the sensor node. The major latency contributing to the system comes from the serial link. Thus, the total latency can be improved by employing a faster serial baud rate. A test on the system shows that the maximum supported baud rate is 57,600bps, which can give a much improved total latency T_l of 7.574 ms.

TABLE 4.1
LATENCIES ASSOCIATED WITH A SINGLE SENSOR NODE

	T_{pn}	T_{pc}	T_{ps}	T_{ds}	T_{dr}	T_l
mean time (μs)	107	90	3981	6250	1312	11740

Next, the latency of the system with multiple sensor nodes is investigated.

The system is configured as a non-beacon multi-access network. Hence, all the nodes have equal access to the communication medium. Moreover, the nodes are allowed to transmit at any time as long as the channel is idle. Each sensor employs a CSMA-CA protocol to avoid collisions. To determine the latency of the network with multiple sensor nodes attached to the arm, the analysis in Fig. 3.5 which shows the case for two sensor nodes is used. Fig 3.5 showed that the latency, T_{block}, is equivalent to the sum of (t_{end} - t_{start}) + T_{header}. t_{start} and t_{end} can be determined using the CPU clock in software while T_{header} can be obtained from the sum of T_{pn}, T_{dr}, T_{pc}, and T_{ds} as in the case for a single sensor node. The latency for three or more sensor nodes can be determined in a similar manner. 1000 block data samples are taken for each network with one to ten sensor nodes in a star network configuration. The result from this experiment is shown in Fig. 4.8. The error bars indicate $\pm\sigma$ values.

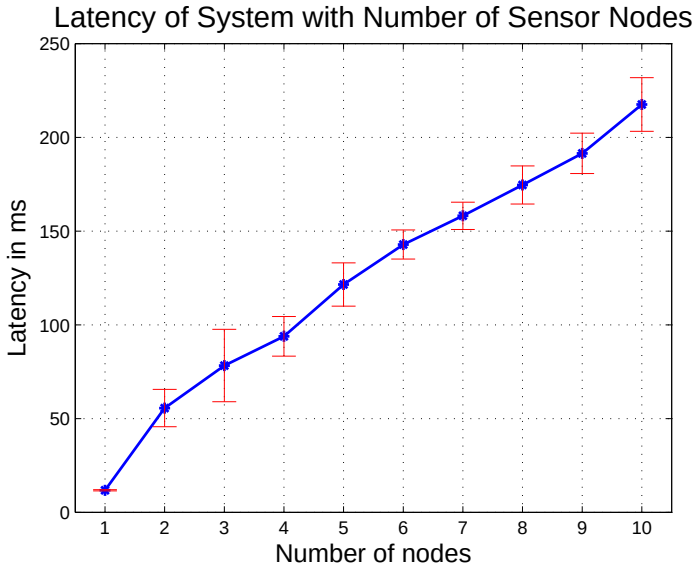

Figure 4.8. Latency of a system with multiple sensor nodes

From the figure, it is observed that the average latency increases by about 20-40 ms with an addition of one sensor node to the existing network. From (3.2), the latency of the system must be less than the sampling period to meet the processing requirements. Thus, a sampling rate of 10 Hz is chosen for our two

sensor node single arm network. The 50 to 90 ms average latency for a 2 to 4 sensor node network is within the acceptable latency of 100 ms for a virtual reality based tracking system. To improve the latency performance, methods such as the use of beacons to minimize coordinator-to-network device latency or the use of pipelining for efficient data computation can be employed.

4.4.3 Power Consumption

Table 4.2 gives a breakdown of a typical average power consumption of a sensor node in operation (at a sampling rate of 10 Hz)

TABLE 4.2
BREAKDOWN OF CURRENT/ POWER CONSUMPTION OF A TYPICAL SENSOR NODE

	Average Current Consumption	**Average Power Consumption**
PICLF2620 microcontroller	4.95mA	16.34mW
MMA7261QT 3-axis accelerometer	500uA	1.65mW
MRF24J40 RF transceiver	20mA	66mW
Entire sensor node	27mA	89mW

Using a 3.6V rechargeable battery with a nominal capacity of 500 mAh, the sensor node should ideally last for 18.5 hours. As observed from Table 4.2, the main power consumption comes from the RF transceiver which consumes 20 mA of current in active mode. When placed in the sleep mode, the transceiver consumes only 2uA. As such, the power management can be further improved by configuring the RF transceiver module to sleep when it is not transmitting. In this case, the average current consumption drops to 8.4 mA. This would prolong the battery life to about 59.5 hours of continuous operation. Assuming a typical usage of 8 hours per day, a single charge of the battery would allow it to be used for one week.

4.4.4 Benchmarking of Proposed Approach With Goniometer Measurements

In Section 4.4.1 of the experimental study, the accuracy of the sensor node for tilt angle determination has been demonstrated under a controlled environment. In this section, the performance of the sensor nodes attached onto a human arm is benchmarked with the readings from a goniometer probe (PS-2137 from PASCO). As shown in Fig. 4.9, the goniometer is a medical measurement device which consists of two metal arm links and a potentiometer. As the angle between the arm changes, the resistance of the potentiometer changes. The accuracy of the goniometer is $\pm 1^{\circ}$ when calibrated, with a resolution of 0.042° at a sampling rate of 500 Hz. The attachment of the goniometer and sensor node to the arm is shown in Fig. 4.9. The data logger for the goniometer is also shown on the left of Fig. 4.9. The sensor nodes are attached to the side of the goniometer so that measurements can be made with respect to the same reference frame for comparison.

Figure 4.9. Attachment of the sensor nodes and goniometer to a human arm

The subject is then asked to perform flexion and extension of his forearm for 100 s. The flexion and extension motion is then repeated 15 times. The subject is instructed to vary the speed of his motion in each time from the slowest in the first

trial to the fastest in the last trial using a metronome as a reference. The mean error and standard deviation over the computed mean angular speed from these experiments are shown in Fig. 4.10. The offset in angle between the proposed system and the goniometer is found by taking the average of the difference in the readings at the maximum flexion and extension point of the forearm.

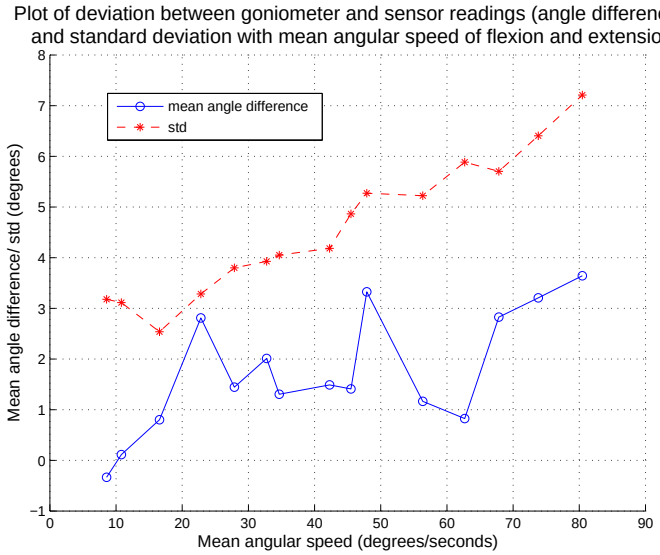

Figure 4.10. Angle between the forearm and the upperarm obtained using the sensor nodes and a goniometer attached at different speeds

From Fig. 4.10, the mean difference in angle between the goniometer and the proposed system shows a linear increasing trend from close to 0° at a mean angular speed of $10°/s$ to 3.5° at a mean angular speed of $80°/s$. The standard deviation also increases in a linear manner from 2.5° to 7° over the range of mean angular speeds. This result is similar to the experimental results in Section 4.4.1 based on the rotary stage but is more pronounced when performed on the human arm. Several factors could have contributed to this effect. In the study, the flexion and extension of the arm is modeled as a rotating motion about a fixed axis and the arm is assumed to be a rigid body. In reality, there will be momentary changes in rotation axis due to muscles and joint movements during flexion and extension movements. Furthermore, the arm rotation may not be restricted in a 2D plane.

4.5 Measurement with Two Degrees of Freedom

With a tri-axial accelerometer, the measurement of the human arm's motion can be generally be performed with two degrees of freedom. Orientation can be determined in 3D albeit with a fixed heading. In this section, two different approaches will be investigated, namely the method of Euler angles using rotation matrices and the method of quaternion. In this study, the accelerometer is assumed to be in a static or slow dynamic condition where the main acceleration is due to gravity.

4.5.1 Method of Euler Angles using Rotation Matrices

One of the most widely used method to describe a rotation is based on the Euler's theorem, which states that any two independent orthonormal coordinate frames can be related by a sequence of rotations (not more than three) about coordinate axes, where no two successive rotations may be about the same axis [71, 82]. As such, a sequence of rotations about coordinate axes can be used to describe an equivalent rotation about an axis with an angle which takes the first coordinate frame to the second coordinate frame. The angle of rotation about a coordinate axis is called an Euler angle. A sequence of such rotations is called an Euler angle sequence. These rotations can be performed using rotation matrices given by

$$\mathbf{R}_{\phi}^{x} = \begin{bmatrix} 1 & 0 & 0 \\ 0 & \cos\phi & \sin\phi \\ 0 & -\sin\phi & \cos\phi, \end{bmatrix}, \mathbf{R}_{\theta}^{y} = \begin{bmatrix} \cos\theta & 0 & -\sin\theta \\ 0 & 1 & 0 \\ \sin\theta & 0 & \cos\theta \end{bmatrix}, \mathbf{R}_{\psi}^{z} = \begin{bmatrix} \cos\psi & \sin\psi & 0 \\ -\sin\psi & \cos\psi & 0 \\ 0 & 0 & 1 \end{bmatrix} \tag{4.21}$$

where $\mathbf{R}_{\phi}^{x}$ refers to a rotation about the x-axis by the angle ϕ, $\mathbf{R}_{\theta}^{y}$ refers to a rotation about the y-axis by the angle θ and $\mathbf{R}_{\psi}^{z}$ refers to a rotation about the z-axis by the angle ψ. In general, a 3×3 matrix is a rotation operator in $\mathbb{R}^3$ if and only if it is an orthogonal matrix and has a determinant of $+1$.

A common Euler angle sequence used in aeronautics is the aerospace rotation sequence [71, 83]. In this sequence, the order of rotation is first a rotation about the z axis by a heading angle of ψ, followed by a rotation of the new y-axis by a pitch angle of θ and then finally a rotation about the new x-axis by a roll angle of ϕ. This can be expressed as the matrix product

$$\mathbf{R}=\mathbf{R}_{\phi}^{x}\mathbf{R}_{\theta}^{y}\mathbf{R}_{\psi}^{z} \tag{4.22a}$$

$$=\begin{bmatrix} 1 & 0 & 0 \\ 0 & c\phi & s\phi \\ 0 & -s\phi & c\phi \end{bmatrix}\begin{bmatrix} c\theta & 0 & -s\theta \\ 0 & 1 & 0 \\ s\theta & 0 & c\theta \end{bmatrix}\begin{bmatrix} c\psi & s\psi & 0 \\ -s\psi & c\psi & 0 \\ 0 & 0 & 1 \end{bmatrix} \tag{4.22b}$$

$$=\begin{bmatrix} c\psi c\theta & s\psi c\theta & -s\theta \\ c\psi s\theta s\phi - s\psi c\phi & s\psi s\theta s\phi + c\psi c\phi & c\theta s\phi \\ \mathrm{c}\psi\mathrm{s}\theta\mathrm{c}\phi + \mathrm{s}\psi\mathrm{s}\phi & s\psi s\theta c\phi - c\psi s\phi & c\theta c\phi \end{bmatrix} \tag{4.22c}$$

where the notations $s\chi = \sin\chi$ and $c\chi = \cos\chi$ are used for the angles $\chi = \phi, \theta, \psi$ and $-180° < \psi \leq 180°, -90° < \theta < 90°, -180° < \phi \leq 180°$.

The Euler rates $(\dot{\phi}, \dot{\theta}, \dot{\psi})$ are related to the non-inertial body rates (p, q, r) in body fixed coordinates by [84]

$$\begin{bmatrix} \dot{\phi} \\ \dot{\theta} \\ \dot{\psi} \end{bmatrix} = \begin{bmatrix} 1 & s\phi s\theta/c\theta & c\phi s\theta/c\theta \\ 0 & c\phi & -s\phi \\ 0 & s\phi/c\theta & c\phi/c\theta \end{bmatrix}\begin{bmatrix} p \\ q \\ r \end{bmatrix} \tag{4.23}$$

Fig. 4.11 shows the inertial and sensor coordinate frames. The X-axis of the inertial frame is defined to be pointing in the posterior direction of the subject. To preserve the heading of the accelerometer, the rotation of the accelerometer can be described by an Euler sequence of a rotation about the sensor y-axis by a pitch angle θ followed by a rotation about the sensor x-axis by a roll angle ϕ. Define the normalized accelerometer output, $\mathbf{a}$, by

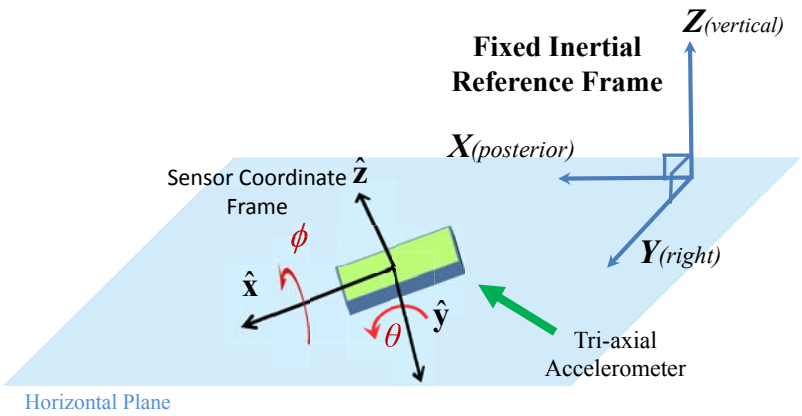

Figure 4.11. Inertial reference and sensor coordinate frames

$$\mathbf{a} = \begin{pmatrix} a_x \\ a_y \\ a_z \end{pmatrix} \tag{4.24}$$

and the normalized gravity vector, $\mathbf{g}$, as

$$\mathbf{g} = \begin{pmatrix} 0 \\ 0 \\ -1 \end{pmatrix} \tag{4.25}$$

Using the rotation matrices, the accelerometer output is related to the gravity vector by the following relationship

$$\mathbf{R}_{\phi}^{x}\mathbf{R}_{\theta}^{y}\mathbf{g} = \mathbf{a} \tag{4.26}$$

Substituting (4.21), (4.24) and (4.25) into (4.26) produces

$$\begin{pmatrix} \sin\theta \\ -\sin\phi\cos\theta \\ -\cos\phi\cos\theta \end{pmatrix} = \begin{pmatrix} a_x \\ a_y \\ a_z \end{pmatrix} \tag{4.27}$$

From (4.27), it is noticed that the value of ϕ cannot be determined when $\theta = \pm 90°$. Geometrically, this means that any subsequent rotation about the x-axis is a rotation about the vertical axis which cannot be resolved using the accelerometer. Consequently, the orientation measurement using the accelerometer is always limited to half the vertical plane, i.e. for $-90° < \theta < 90°$.

From (4.27), θ and ϕ can be solved as

$$\theta = \text{atan}\left(\frac{a_x}{\sqrt{{a_y}^2 + a_z^2}}\right) \tag{4.28}$$

$$\phi = \text{atan2}\left(-a_y, -a_z\right) \tag{4.29}$$

where $-90° < \theta < 90°$ and $-180° < \phi \leq 180°$, atan is the 2-quadrant arctangent function while atan2(y,x) is the 4-quadrant arctangent function that computes the arctangent using both the signs of x and y. The solution space is also restricted to half of the Cartesian 3D space since there are two orientations of the accelerometer with the same output signal given the single plane restriction. These two orientations differ only by a rotation about the vertical axis by 180°. The equivalent rotation matrix is given by:

$$\mathbf{R} = \mathbf{R}_\phi^x \mathbf{R}_\theta^y = \begin{pmatrix} r_{11} & r_{12} & r_{13} \\ r_{21} & r_{22} & r_{23} \\ r_{31} & r_{32} & r_{33} \end{pmatrix} = \begin{pmatrix} \cos\theta & 0 & -\sin\theta \\ \sin\theta\sin\phi & \cos\phi & \cos\theta\sin\phi \\ \sin\theta\cos\phi & -\sin\phi & \cos\theta\cos\phi \end{pmatrix} \tag{4.30}$$

The equivalent axis, $\mathbf{v}$, and angle, ϕ_v, of rotation can be obtained using the general formulas [71]

$$\mathbf{v} = \begin{pmatrix} r_{23} - r_{32} \\ r_{31} - r_{13} \\ r_{12} - r_{21} \end{pmatrix} \tag{4.31}$$

$$\phi_v = \cos^{-1}\left(\frac{tr\,(\mathbf{R}) - 1}{2}\right) \tag{4.32}$$

where $tr()$ denotes the trace of a matrix.

4.5.2 Method of Quaternion

Inherent in every minimal Euler angle rotation sequence in the special orthogonal group, SO(3) (the group of 3 by 3 orthogonal matrices with determinant 1), is at least one singularity [71]. This can be illustrated with the aerospace angle sequence given in (4.22) as an example. The domain for the Euler angles in the aerospace angle sequence is $-180° < \psi \leq 180°, -90° < \theta < 90°, -180° < \phi \leq 180°$. If the angle θ increases from $90° - \epsilon$ to $90° + \epsilon$, the angle ϕ must go instantaneously from ϕ to $\phi + 180°$. This is necessary to ensure the uniqueness of solutions for ϕ and θ. In addition, the value of ϕ is undefined when $\theta = \pm 90°$. Therefore, $\theta = \pm 90°$ are known as singular points and are to be avoided. This singularity can also be observed from the relationship of the Euler rates to the noninertial body rates in (4.23). The behaviour of tracking algorithms is often erratic in the neighbourhood of these singular points with serious transient errors in determining the Euler Angles. This condition is also known as the Gimbal Lock. For instance, a gunner operating a barrel gun tracking an aircraft may find himself having to suddenly change his azimuth by 180° as the aircraft flies overhead. Gimbal Lock can be considered as a loss of degree of freedom. For the Aerospace Sequence, the x-axis (roll axis) is aligned with the initial z-axis (yaw axis) when $\theta = \pm 90°$, i.e. any rotation about the roll axis is equivalent to rotation about the initial yaw axis. As such, a degree of freedom is lost.

Since a rotation can be described by an equivalent axis and angle of rotation, three parameters are sufficient in a rotation operator. For instance, the axis of rotation can be described by using a unit normal vector while the angle of rotation can be described by varying the magnitude of the vector. Thus, the rotation

matrix (4.22) with nine parameters has a high level of redundancy. As such, the 4-element tuple known as the quaternion [85] is commonly used as an alternative. The quaternion method can lead to linear equations that are simpler to solve as compared to the three-parameter methods [86]. The quaternion operator is singularity-free and can relate any two independent coordinate frames in $\mathbb{R}^3$. It is also useful as the trigonometric functions are avoided.

The equivalent angle and axis of rotation of the accelerometer can be represented by a quaternion, q, given by

$$q = \begin{pmatrix} q_0 \\ q_1 \\ q_2 \\ q_3 \end{pmatrix} = \begin{pmatrix} q_0 \\ \mathbf{q} \end{pmatrix} = \begin{pmatrix} \cos\frac{\theta_v}{2} \\ \mathbf{v}\sin\frac{\theta_v}{2} \end{pmatrix} \tag{4.33}$$

The first element q_0 of q denotes the scalar part of the quaternion and is related to the angle of rotation, θ_v, by

$$q_0 = \cos\left(\frac{\theta_v}{2}\right) \tag{4.34}$$

The second to last elements of the quaternion, q, denote the vector part, $\mathbf{q}$, of the quaternion and is related to the axis of rotation, $\mathbf{v}$, by

$$\mathbf{q} = \begin{pmatrix} q_1 \\ q_2 \\ q_3 \end{pmatrix} = \mathbf{v}\sin\left(\frac{\theta_v}{2}\right) \tag{4.35}$$

In addition, the quaternion rotation operator, $L_q(\mathbf{u})$, is defined following the notation in [71] as

$$L_q(\mathbf{u}) = q\mathbf{u}q^* = \left({q_0}^2 - \|\mathbf{q}\|^2\right)\mathbf{u} + 2(\mathbf{q}^T\mathbf{u})\mathbf{q} + 2q_0(\mathbf{q}\times\mathbf{u}) \tag{4.36}$$

where (*) is the quaternion conjugate operator and $\times$ refers to the vector

product. The quaternion operator $L_q(\mathbf{u})$ in (4.36) may be interpreted as a rotation of the vector, $\mathbf{u}$, through an angle θ_v with the vector $\mathbf{v}$ as the axis of rotation.

On the other hand, the quaternion rotation operator, $L_{q*}(\mathbf{u})$, is defined as

$$L_{q*}(\mathbf{u}) = q^*\mathbf{u}q = \left({q_0}^2 - \|\mathbf{q}\|^2\right)\mathbf{u} + 2(\mathbf{u}^T\mathbf{q})\mathbf{q} + 2q_0(\mathbf{u}\times\mathbf{q}) \tag{4.37}$$

The quaternion rotation operator $L_{q*}(\mathbf{u})$ in (4.37) can be interpreted as a coordinate frame rotation through an angle θ_v with the vector $\mathbf{v}$ as the axis of rotation, giving the representation of the vector $\mathbf{u}$ with respect to the rotated coordinate frame.

Closed-Form Quaternions based on Euler Angles

In this section, a closed-form algorithm to determine the orientation of the accelerometer is developed. This method is similar to the method of Euler angles except that the quaternions are used to represent the Euler angles rotations.

Let the quaternion, s, represents a rotation about the sensor x-axis by an angle ϕ and the quaternion, t, represents a rotation about the sensor y-axis by an angle θ. These quaternions are determined using (4.33) as

$$s = \begin{pmatrix} s_1 \\ s_2 \\ 0 \\ 0 \end{pmatrix} = \begin{pmatrix} \cos\frac{\phi}{2} \\ \sin\frac{\phi}{2} \\ 0 \\ 0 \end{pmatrix}, \quad t = \begin{pmatrix} t_1 \\ 0 \\ t_2 \\ 0 \end{pmatrix} = \begin{pmatrix} \cos\frac{\theta}{2} \\ 0 \\ \sin\frac{\theta}{2} \\ 0 \end{pmatrix} \tag{4.38}$$

Let $q = st$ and using (4.37), the normalized gravity vector, $\mathbf{g}$, in (4.25) is then related to the accelerometer output by

$$s^*t^*\mathbf{g}ts = \begin{pmatrix} a_x \\ a_y \\ a_z \end{pmatrix} \tag{4.39}$$

Substituting (4.38) into (4.39) and simplifying gives the following

$$\begin{pmatrix} 2t_1t_2 \\ -2s_1s_2\left({t_1}^2-{t_2}^2\right) \\ -\left(s_1^2-s_2^2\right)\left(t_1^2-t_2^2\right) \end{pmatrix} = \begin{pmatrix} a_x \\ a_y \\ a_z \end{pmatrix} \tag{4.40}$$

From (4.40) and the condition of unity norm for the quaternions, the closed-form solution for the elements of the quaternions s and t can be derived as

$$t_1 = \sqrt{\frac{1}{2}\left(1+\sqrt{1-{a_x}^2}\right)} \tag{4.41a}$$

$$t_2 = sign\left(a_x\right)\sqrt{1-{t_1}^2} \tag{4.41b}$$

$$s_1 = \sqrt{\frac{1}{2}\left(1-sign\left(a_z\right)\sqrt{\frac{{a_z}^2}{{a_y}^2+{a_z}^2}}\right)} \tag{4.42a}$$

$$s_2 = -sign\left(a_y\left(2t_1^2-1\right)\right)\sqrt{1-s_1^2} \tag{4.42b}$$

where $sign()$ is the signum function. The resultant quaternion, q, can be determined by the quaternion product of ts as

$$q = ts = \begin{pmatrix} t_1s_1 \\ t_1s_2 \\ t_2s_1 \\ -t_2s_2 \end{pmatrix} \tag{4.43}$$

The equivalent axis of rotation, $\mathbf{v}$ and the angle of rotation $\theta_{\mathbf{v}}$ can be found using (4.33) and (4.43) as

$$\theta_v = 2\cos^{-1}\left(t_1s_1\right) \tag{4.44}$$

$$\mathbf{v} = \begin{cases} \frac{1}{\sin\left(\theta_v/2\right)} \begin{pmatrix} t_1 s_2 \\ t_2 s_1 \\ -t_2 s_2 \end{pmatrix}, & \text{for } \sin\left(\theta_v/2\right) \neq 0 \\ \begin{pmatrix} 0 \\ 0 \\ 0 \end{pmatrix}, & \text{for } \sin\left(\theta_v/2\right) = 0 \end{cases} \tag{4.45}$$

Since the quaternions perform the Euler angle sequence as discussed in Section 4.5.1, it can be observed from (4.42a) that a similar singularity will occur when $a_y^2 + a_z^2 = 0$ which is equivalent to the case when $\theta = \pm 90°$. However it should be noted that the quaternion rotation operator is singular-free and can relate any two independent coordinate frames in R^3.

4.6 Determination of the Orientation of the Articulated Human Arm Limbs

In the previous section, the orientation determination of a single accelerometer node was presented. In this section, the orientation of an articulated arm limb, i.e the upperarm and the forearm is investigated. For this study, one accelerometer node is attached to the upperarm while another is attached to the forearm. Fig. 4.12 illustrates the fixed inertial reference frame and the locations of the two triaxial accelerometers. In the remaining section, a new approach based on single axis-angle quaternions with constrained optimization to determine the orientations of the upperarm and forearm is presented.

4.6.1 Determination of the Upperarm's Orientation

To determine the upperarm's orientation, the equivalent angle and axis of rotation of the accelerometer attached to the upperarm is represented by a quaternion, q,

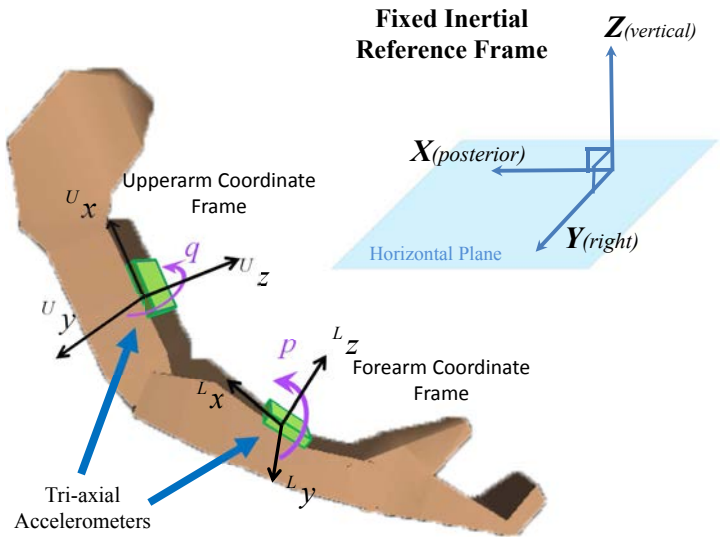

Figure 4.12. Reference frame showing the quaternions representing rotations of upperarm and forearm

as shown in Fig. 4.12 by

$$q = \begin{pmatrix} q_0 \\ q_1 \\ q_2 \\ q_3 \end{pmatrix} \tag{4.46}$$

Define ${}^{U}\mathbf{a}$ as the normalized output of the accelerometer attached to the upperarm as

$${}^{U}\mathbf{a} = \begin{pmatrix} {}^{U}a_x \\ {}^{U}a_y \\ {}^{U}a_z \end{pmatrix} \tag{4.47}$$

then using the quaternion operator defined in (4.37), the accelerometer output, ${}^{U}\mathbf{a}$, can be related to the quaternion, q, and the normalized gravity vector, $\mathbf{g}$ by

$$q^* \mathbf{g} q = {}^U\mathbf{a} \tag{4.48}$$

Substituting (4.46) and (4.47) into (4.48) produces

$$\begin{pmatrix} 2q_0q_2 - 2q_1q_3 \\ -2q_0q_1 - 2q_2q_3 \\ -{q_0}^2 + {q_1}^2 + {q_2}^2 - {q_3}^2 \end{pmatrix} = \begin{pmatrix} {}^Ua_x \\ {}^Ua_y \\ {}^Ua_z \end{pmatrix} \tag{4.49}$$

In the presence of noise and errors due to factors such as offset and temperature biases of the accelerometer, (4.49) can be modified as

$$\begin{pmatrix} 2q_0q_2 - 2q_1q_3 \\ -2q_0q_1 - 2q_2q_3 \\ -{q_0}^2 + {q_1}^2 + {q_2}^2 - {q_3}^2 \end{pmatrix} = \begin{pmatrix} {}^Ua_x \\ {}^Ua_y \\ {}^Ua_z \end{pmatrix} + \begin{pmatrix} {}^U\eta_x \\ {}^U\eta_y \\ {}^U\eta_z \end{pmatrix} \tag{4.50}$$

where ${}^U\eta_x$, ${}^U\eta_y$, ${}^U\eta_z$ are the noise and error components in the respective x, y and z-axis of the accelerometer.

Consider that the ${}^Ux$-axis is limited to the X-Z plane, and the ${}^Ux$-axis is rotated by an angle ρ with respect to the X-axis, the following relationship can be obtained using the quaternion operator in (4.36)

$$q \begin{pmatrix} 1 \\ 0 \\ 0 \end{pmatrix} q^* = \begin{pmatrix} \cos\rho \\ 0 \\ \sin\rho \end{pmatrix} \tag{4.51a}$$

$$\Rightarrow \begin{pmatrix} {q_0}^2 + {q_1}^2 - {q_2}^2 - {q_3}^2 \\ 2q_1q_2 + 2q_0q_3 \\ 2q_1q_3 - 2q_0q_2 \end{pmatrix} = \begin{pmatrix} \cos\rho \\ 0 \\ \sin\rho \end{pmatrix} \tag{4.51b}$$

The first and third rows of (4.51b) are equivalent to the property that the norm of the quaternion is equal to one. The second row of (4.51b) on the other

hand gives the constraint for heading. This constraint can also be observed from the quaternion q in (4.43) where $q_1q_2 + q_0q_3$ is equal to zero.

In summary, the following constrained optimization problem based on (4.50) – (4.51b) can be defined as follows:

Constraint Optimization

$$\min_{q} {}^{U}f(q) \text{ subject to } {}^{U}c(q) = \mathbf{0} \tag{4.52}$$

where ${}^{U}f : \mathbb{R}^4 \to \mathbb{R}$, ${}^{U}c : \mathbb{R}^4 \to \mathbb{R}^2$ and ${}^{U}f(q)$ is defined as

$${}^{U}f(q) = {}^{U}A^2 + {}^{U}B^2 + {}^{U}C^2 \tag{4.53}$$

where ${}^{U}A$, ${}^{U}B$, and ${}^{U}C$ are variables defined as

$${}^{U}A = 2q_0q_2 - 2q_1q_3 - {}^{U}a_x \tag{4.54a}$$

$${}^{U}B = -2q_0q_1 - 2q_2q_3 - {}^{U}a_y \tag{4.54b}$$

$${}^{U}C = -{q_0}^2 + {q_1}^2 + {q_2}^2 - {q_3}^2 - {}^{U}a_z \tag{4.54c}$$

and ${}^{U}c(q)$ describes the following constraint

$${}^{U}c(q) = \begin{bmatrix} {q_0}^2 + {q_1}^2 + {q_2}^2 + {q_3}^2 - 1 \\ q_1q_2 + q_0q_3 \end{bmatrix} = \mathbf{0} \tag{4.55}$$

The first constraint is required to satisfy the unity norm property of the quaternion. The second constraint is to limit the upperarm's motion to the sagittal, X-Z, plane.

For the optimization, the constraint local minimum is a critical point of the Lagrangian function

$${}^{U}\mathcal{L}\left(q, {}^{U}\boldsymbol{\lambda}\right) = {}^{U}f\left(q\right) - {}^{U}\boldsymbol{\lambda}^{T\,U}c\left(q\right) \tag{4.56}$$

where ${}^{U}\boldsymbol{\lambda} \in \mathbb{R}^2$ is the vector of Lagrange multipliers. For this problem, the first-order necessary condition for a critical point of the Lagrangian function can be derived as

$$\nabla^{U}\mathcal{L}\left(q, {}^{U}\boldsymbol{\lambda}\right) = \begin{bmatrix} \nabla^{U} f\left(q\right) - {}^{U}\mathbf{J_c}^{T}\left(q\right) {}^{U}\boldsymbol{\lambda} \\ {}^{U}c\left(q\right) \end{bmatrix} = 0 \tag{4.57}$$

where $\nabla^{U} f(q)$ is the gradient of function ${}^{U}f(q)$

$$\nabla^{U} f(q) = 4 \begin{bmatrix} q_2 {}^{U}A - q_1 {}^{U}B - q_0 {}^{U}C \\ -q_3 {}^{U}A - q_0 {}^{U}B + q_1 {}^{U}C \\ q_0 {}^{U}A - q_3 {}^{U}B + q_2 {}^{U}C \\ -q_1 {}^{U}A - q_2 {}^{U}B - q_3 {}^{U}C \end{bmatrix} \tag{4.58}$$

and ${}^{U}\mathbf{J_c}(q)$ is the Jacobian of the function ${}^{U}c(q)$ given by

$${}^{U}\mathbf{J_c}(q) = 2 \begin{bmatrix} q_0 & q_1 & q_2 & q_3 \\ q_3 & q_2 & q_1 & q_0 \end{bmatrix} \tag{4.59}$$

From an initial estimate $(q_0, {}^{U}\boldsymbol{\lambda}_0)$, the Newton's method [87] can be used to solve for the non-linear system of equations. The linearized system to be solved at the k^{th} iteration for the Newton step can be derived as

$$\begin{bmatrix} {}^{U}\mathbf{B}\left(q_k, \boldsymbol{\lambda}_k\right) {}^{U}\mathbf{J_c}^{T}\left(q_k\right) \\ {}^{U}\mathbf{J_c}\left(q_k\right) \qquad \mathrm{O} \end{bmatrix} \begin{bmatrix} {}^{U}\mathbf{s}_k \\ {}^{U}\delta_k \end{bmatrix} = - \begin{bmatrix} \nabla^{U} f(q_k) - {}^{U}\mathbf{J_c}^{T}\left(q_k\right) {}^{U}\boldsymbol{\lambda}_k \\ {}^{U}c\left(q_k\right) \end{bmatrix} \tag{4.60}$$

where ${}^{U}\mathbf{s}_k$ and ${}^{U}\delta_k$ are the step sizes for q_k and ${}^{U}\boldsymbol{\lambda}_k$ respectively and

$${}^{U}\mathbf{B}\left(q, \boldsymbol{\lambda}\right) = {}^{U}\mathbf{H}_f\left(q\right) + \sum_{i=1}^{2} {}^{U}\lambda_i {}^{U}\mathbf{H}_{c_i}\left(q\right) \tag{4.61}$$

with ${}^{U}H_f$ the Hessian of ${}^{U}f(q)$ given by

$$
{}^{U}\mathbf{H}_f\left(q\right) = 4\begin{bmatrix} n_q + 2q_0 + {}^{U}a_z & {}^{U}h_{1q} & {}^{U}h_{2q} & 2q_0q_3 \\ {}^{U}h_{1q} & n_q + 2q_1 - {}^{U}a_z & 2q_1q_2 & {}^{U}h_{3q} \\ {}^{U}h_{2q} & 2q_1q_2 & n_q + 2q_2 - {}^{U}a_z & {}^{U}h_{4q} \\ 2q_0q_3 & {}^{U}h_{3q} & {}^{U}h_{4q} & n_q + 2q_3 + {}^{U}a_z \end{bmatrix} \tag{4.62}
$$

where

$$n_q = {q_0}^2 + {q_1}^2 + {q_2}^2 + {q_3}^2 \tag{4.63a}$$

$${}^{U}h_{1q} = 2q_0q_1 + {}^{U}a_y \tag{4.63b}$$

$${}^{U}h_{2q} = 2q_0q_2 - {}^{U}a_x \tag{4.63c}$$

$${}^{U}h_{3q} = 2q_1q_3 + {}^{U}a_x \tag{4.63d}$$

$${}^{U}h_{4q} = 2q_2q_3 + {}^{U}a_y \tag{4.63e}$$

and

$${}^{U}\mathbf{H}_{c_1} = 2\mathbf{I}_4 \tag{4.64a}$$

$${}^{U}\mathbf{H}_{c_2} = 2\begin{bmatrix} 0 & 0 & 0 & 1 \\ 0 & 0 & 1 & 0 \\ 0 & 1 & 0 & 0 \\ 1 & 0 & 0 & 0 \end{bmatrix} \tag{4.64b}$$

where $\mathbf{I}_4$ is the 4×4 identity matrix.

The pseudocode for the implementation is given in Algorithm 4.1.

4.6.2 Determination of the Forearm's Orientation

The formulation in section 4.6.1 restricts the ${}^{U}x$-axis of the upperarm to be fixed in the X-Z plane of the body. If the upperarm was to perform either a medial

Algorithm 4.1: Single Angle-Axis Quaternion Algorithm for Determination of Upperarm's Orientation

Choose an initial pair $(q_0, {}^{U}\boldsymbol{\lambda}_0)$, set $k \leftarrow 0$
repeat
  Evaluate $\nabla {}^{U}f(q_k)$ from (4.58),${}^{U}\mathbf{B}\,(q_k, {}^{U}\boldsymbol{\lambda}_k)$ from (4.61)–(4.64), ${}^{U}c(q_k)$ from (4.55) and ${}^{U}\mathbf{J_c}(q_k)$ from (4.59)
  Solve (4.60) to obtain ${}^{U}\mathbf{s}_k$ and ${}^{U}\delta_k$
  Set $q_{k+1} \leftarrow q_k + {}^{U}\mathbf{s}_k$ and ${}^{U}\boldsymbol{\lambda}_{k+1} \leftarrow {}^{U}\boldsymbol{\lambda}_k + {}^{U}\delta_k$
  $k \leftarrow k + 1$
until *a convergence test is satisfied*

or lateral rotation while keeping its ${}^{U}x$-axis along the X-Z plane, the ${}^{L}x$-axis of the forearm will no longer remain in the X-Z plane. In this section, a solution is presented to determine the forearm's orientation under this circumstance.

From Fig. 4.12, the rotation of the accelerometer attached to the forearm is represented by the quaternion, p, given by

$$p = \begin{pmatrix} p_0 \\ p_1 \\ p_2 \\ p_3 \end{pmatrix} \tag{4.65}$$

The normalized output of the accelerometer, ${}^{L}\mathbf{a}$, attached to the forearm can be expressed as

$${}^{L}\mathbf{a} = \begin{pmatrix} {}^{L}a_x \\ {}^{L}a_y \\ {}^{L}a_z \end{pmatrix} \tag{4.66}$$

Using (4.37), the accelerometer output ${}^{L}\mathbf{a}$, is related to the quaternion, p, and the normalized gravity vector, $\mathbf{g}$ by

$$p^* \mathbf{g} p = {}^{L}\mathbf{a} \tag{4.67}$$

Note that the plane of motion of the upperarm, i.e the ${}^{U}x$-${}^{U}z$ plane, can be described by

$$\mathbf{r}^T\mathbf{v}_\perp = \mathbf{r}^T \begin{pmatrix} 0 \\ 1 \\ 0 \end{pmatrix} = 0 \tag{4.68}$$

where $\mathbf{r}$ is any vector that lies in the ${}^{U}x$-${}^{U}z$ plane and $\mathbf{v}_\perp$ is the vector that is perpendicular to the ${}^{U}x$-${}^{U}z$ plane, which in this case is the ${}^{U}y$-axis. A rotation of the upperarm with quaternion q yields the vector $\mathbf{v}_\perp$:

$$\mathbf{v}_\perp = q \begin{pmatrix} 0 \\ 1 \\ 0 \end{pmatrix} q^* \tag{4.69a}$$

$$\Rightarrow \begin{pmatrix} v_{\perp 1} \\ v_{\perp 2} \\ v_{\perp 3} \end{pmatrix} = \begin{pmatrix} 2q_1q_2 - 2q_0q_3 \\ q_0^2 - q_1^2 + q_2^2 - q_3^2 \\ 2q_2q_3 + 2q_0q_1 \end{pmatrix} \tag{4.69b}$$

The ${}^{L}x$-axis of the forearm should remain perpendicular to the vector $\mathbf{v}_\perp$, thus

$$\left[p \begin{pmatrix} 1 \\ 0 \\ 0 \end{pmatrix} p^* \right]^T \mathbf{v}_\perp = 0$$

$$\Rightarrow \begin{pmatrix} p_0^2 + p_1^2 - p_2^2 - p_3^2 \\ 2p_1p_2 + 2p_0p_3 \\ 2p_1p_3 - 2p_0p_2 \end{pmatrix}^T \begin{pmatrix} v_{\perp 1} \\ v_{\perp 2} \\ v_{\perp 3} \end{pmatrix} = 0 \tag{4.70}$$

Eqn (4.70) gives the constraint for the forearm to stay in a fixed plane which is dependent on the upperarm's orientation. Together with the constraint for unity norm, the overall constraint for the forearm can be written as

$$
{}^{L}\mathbf{c}(p) = \begin{bmatrix} p_0^2 + p_1^2 + p_2^2 + p_3^2 - 1 \\ v_{\perp 1}\left(p_0^2 + p_1^2 - p_2^2 - p_3^2\right) + v_{\perp 2}\left(2p_1p_2 + 2p_0p_3\right) + v_{\perp 3}\left(2p_1p_3 - 2p_0p_2\right) \end{bmatrix} = \mathbf{0} \tag{4.71}
$$

In (4.71), the values of $v_{\perp 1}$, $v_{\perp 2}$ and $v_{\perp 3}$ can be determined using the estimated value of q from Section 4.6.1. The cost function ${}^{L}f(p)$ for constrained optimization for the forearm is similar to (4.52) with the elements of q replaced by p. Hence, the following optimization problem can be obtained:

Constraint Optimization

$$
\min_{p} {}^{L}f(p) \text{ subject to } {}^{L}c(p) = \mathbf{0} \tag{4.72}
$$

where ${}^{L}f : \mathbb{R}^4 \to \mathbb{R}$, ${}^{L}c : \mathbb{R}^4 \to \mathbb{R}^2$ and ${}^{L}f(p)$ is defined as

$$
{}^{L}f(p) = {}^{L}A^2 + {}^{L}B^2 + {}^{L}C^2 \tag{4.73}
$$

where ${}^{L}A$, ${}^{L}B$, and ${}^{L}C$ are variables defined as

$$
{}^{L}A = 2p_0p_2 - 2p_1p_3 - {}^{L}a_x \tag{4.74a}
$$

$$
{}^{L}B = -2p_0p_1 - 2p_2p_3 - {}^{L}a_y \tag{4.74b}
$$

$$
{}^{L}C = -{p_0}^2 + {p_1}^2 + {p_2}^2 - {p_3}^2 - {}^{L}a_z \tag{4.74c}
$$

and the constraint function ${}^{L}c(p)$ is as given in (4.71)

The problem (4.71) - (4.74) is solved in a similar manner as the upperarm using Newton's method with an initial estimate $(p_0, {}^{L}\boldsymbol{\lambda}_0)$.

The gradient $\nabla {}^{L}f(p)$ of function ${}^{L}f(p)$ is similar to (4.58) and is given by

$$
\nabla {}^{L}f(p) = 4 \begin{bmatrix} p_2{}^{L}A - p_1{}^{L}B - p_0{}^{L}C \\ -p_3{}^{L}A - p_0{}^{L}B + p_1{}^{L}C \\ p_0{}^{L}A - p_3{}^{L}B + p_2{}^{L}C \\ -p_1{}^{L}A - p_2{}^{L}B - p_3{}^{L}C \end{bmatrix} \tag{4.75}
$$

Since the constraint for the plane of motion has changed, the Jacobian of ${}^{L}\mathbf{J_c}(p)$ is now determined as

$$ {}^{L}\mathbf{J_c}(p) = 2 \begin{bmatrix} p_0 & v_{\perp 1}p_0 + v_{\perp 2}p_3 - v_{\perp 3}p_2 \\ p_1 & v_{\perp 1}p_1 + v_{\perp 2}p_2 + v_{\perp 3}p_3 \\ p_2 & -v_{\perp 1}p_2 + v_{\perp 2}p_1 - v_{\perp 3}p_0 \\ p_3 & -v_{\perp 1}p_3 + v_{\perp 2}p_0 + v_{\perp 3}p_1 \end{bmatrix}^T \tag{4.76} $$

The linearized system to be solved at the k^{th} iteration for the Newton step is given by

$$ \begin{bmatrix} {}^{L}\mathbf{B}\left(p_k, {}^{L}\boldsymbol{\lambda}_k\right) {}^{L}\mathbf{J_c}^{T}\left(p_k\right) \\ {}^{L}\mathbf{J_c}\left(p_k\right) \qquad \mathrm{O} \end{bmatrix} \begin{bmatrix} {}^{L}\mathbf{s}_k \\ {}^{L}\delta_k \end{bmatrix} = - \begin{bmatrix} \nabla {}^{L}f(p_k) - {}^{L}\mathbf{J_c}^{T}\left(p_k\right) {}^{L}\boldsymbol{\lambda}_k \\ {}^{L}c\left(p_k\right) \end{bmatrix} \tag{4.77} $$

where ${}^{L}\mathbf{s}_k$ and ${}^{L}\delta_k$ are the step sizes for p_k and ${}^{L}\boldsymbol{\lambda}_k$ respectively and

$$ {}^{L}\mathbf{B}\left(p, \boldsymbol{\lambda}\right) = {}^{L}\mathbf{H}_f\left(p\right) + \sum_{i=1}^{2} {}^{L}\lambda_i {}^{L}\mathbf{H}_{c_i}\left(p\right) \tag{4.78} $$

with ${}^{L}H_f$ the Hessian of ${}^{L}f(p)$ given by

$$ {}^{L}\mathbf{H}_f\left(p\right) = 4 \begin{bmatrix} n_p + 2p_0 + {}^{L}a_z & {}^{L}h_{1p} & {}^{L}h_{2p} & 2p_0p_3 \\ {}^{L}h_{1p} & n_p + 2p_1 - {}^{L}a_z & 2p_1p_2 & {}^{L}h_{3p} \\ {}^{L}h_{2p} & 2p_1p_2 & n_p + 2p_2 - {}^{L}a_z & {}^{L}h_{4p} \\ 2p_0p_3 & {}^{L}h_{3p} & {}^{L}h_{4p} & n_p + 2p_3 + {}^{L}a_z \end{bmatrix} \tag{4.79} $$

where

$$n_p = {p_0}^2 + {p_1}^2 + {p_2}^2 + {p_3}^2 \tag{4.80a}$$

$${}^{L}h_{1p} = 2p_0p_1 + {}^{L}a_y \tag{4.80b}$$

$${}^{L}h_{2p} = 2p_0p_2 - {}^{L}a_x \tag{4.80c}$$

$${}^{L}h_{3p} = 2p_1p_3 + {}^{L}a_x \tag{4.80d}$$

$${}^{L}h_{4p} = 2p_2p_3 + {}^{L}a_y \tag{4.80e}$$

and

$${}^{L}\mathbf{H}_{c_1} = 2\mathbf{I}_4 \tag{4.81a}$$

$${}^{L}\mathbf{H}_{c_2} = \begin{bmatrix} v_{\perp 1} & 0 & -v_{\perp 3} & v_{\perp 2} \\ 0 & v_{\perp 1} & v_{\perp 2} & v_{\perp 3} \\ -v_{\perp 3} & v_{\perp 2} & -v_{\perp 1} & 0 \\ v_{\perp 2} & v_{\perp 3} & 0 & -v_{\perp 1} \end{bmatrix} \tag{4.81b}$$

Again, (4.79) - (4.81a) is similar to (4.62) - (4.64a) with q replaced by p. The expression for ${}^{L}\mathbf{H}_{c_2}$ in (4.81b) is different from (4.64b) due to the change in the second constraint of ${}^{L}\mathbf{c}(p)$.

The pseudocode for the implementation is given in Algorithm 4.2.

Algorithm 4.2: Single Angle-Axis Quaternion Algorithm for Determination of Forearm's Orientation

Obtain estimate of q from Algorithm 4.1 and evaluate $\mathbf{v}_\perp$ using (4.69)
Choose an initial pair $(p_0, {}^{L}\boldsymbol{\lambda}_0)$, Set $k \leftarrow 0$
repeat
  Evaluate $\nabla {}^{L}f(p_k)$ from (4.75), ${}^{L}\mathbf{B}\,(p_k, \lambda_k)$ from (4.78) - (4.81), ${}^{L}c(p_k)$ from (4.71) and ${}^{L}\mathbf{J}_{\mathbf{c}}(p_k)$ from (4.76)
  Solve (4.77) to obtain ${}^{L}\mathbf{s}_k$ and ${}^{L}\delta_k$
  Set $p_{k+1} \leftarrow p_k + {}^{L}\mathbf{s}_k$ and ${}^{L}\boldsymbol{\lambda}_{k+1} \leftarrow {}^{L}\boldsymbol{\lambda}_k + {}^{L}\delta_k$
  $k \leftarrow k + 1$
until *a convergence test is satisfied*

The main disadvantage of this approach is that the estimate of q or p will tend to diverge at the singular states when either the upperarm or forearm is in a vertical position. To avoid these singular states, the measurement of an arm limb's motion is conventionally limited to one half of the plane.

4.7 Simulation Studies

To investigate the performance of the single angle-axis quaternion algorithm, numerical simulations were performed. In the single angle-axis quaternion approach, a quaternion corresponding to the orientation for each of the arm limbs is computed. For ease of comparison, this computed quaternion is transformed into the equivalent Euler angles. The range of the Euler angles are -90° < yaw < 90°, -180° < pitch ≤ 180° and -180° < roll ≤ 180°. A zero-mean white Gaussian noise of standard deviation 0.03 (as estimated from actual accelerometer signal) is also simulated in the accelerometer output. The sampling rate of the accelerometers is 10 Hz.

4.7.1 Upperarm Singularities

Fig. 4.13a-b shows the simulated flexion/extension and medial/lateral rotation of the left upperarm with the estimated roll, pitch and yaw angles obtained using the single angle-axis quaternion approach. The corresponding arm positions is also shown in Fig. 4.13c for ease of visualization. The estimated yaw angle is observed to be zero throughout the simulation, as the arm movement is restricted to the sagittal plane. In this simulation, the upperarm is initially in the horizontal position with the palm facing up. It then performs a flexion movement until the arm is raised almost vertically (pitch = 89°) with a simultaneous medial rotation from roll = 0° to −90°. Following that, it is extended until it is just beside the body (pitch = −89°) while performing a lateral rotation to 90°. The upperarm is

then flexed and medially rotated back to the horizontal position at the 40^{th} data sample. Up to this point, the upperarm is simulated to perform motion within half the sagital plane, i.e. for $-90° < \theta < 90°$ and $-90° < \phi < 90°$. It can be observed that the estimated pitch follows closely the true pitch value. The estimated roll angle also follows closely the true roll angle except when the pitch angle is close to $\pm 90°$ at the 10^{th} and 30^{th} data sample where the estimated roll angle diverges away from the true roll angle. This demonstrates the limitation of the single angle-axis quaternion approach in determining the upperarm's orientation even at the neighbourhood of the singularity points of pitch $= \pm 90°$.

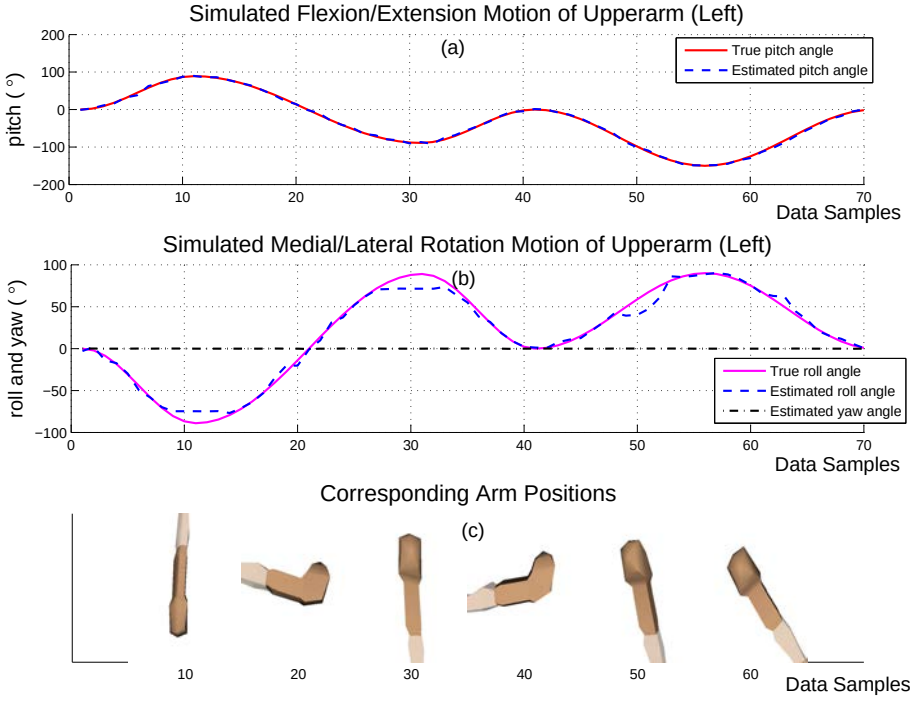

Figure 4.13. Simulated combination of flexion/ extension and medial/ lateral rotation of upperarm using the single angle-axis quaternion approach

From the 40^{th} data sample onwards, the upperarm performs an extension to $150°$ below the horizontal while performing a medial rotation, extending the motion beyond the half-sagittal plane. It is then finally flexed and lateral rotated back to the horizontal position. As expected, it is observed that the roll angle again diverges from the true angle at the singular points of pitch $= -90°$. To avoid

these singular points, the measurement of the motion of the upperarm is limited to half the sagittal plane when using the single angle-axis quaternion approach.

4.7.2 Forearm Singularities

In this simulation, the performance of the single angle-axis quaternion approach in determining the forearm's orientation in a series of motion together with the upperarm is investigated. Fig 4.14a shows the simulated angles of flexion/extension and medial/lateral rotation of the upperarm while the corresponding simulated angles of flexion/extension and pronation/supination of the forearm is shown in Fig. 4.14b. The corresponding arm positions are shown in Fig. 4.14f. The left arm is assumed to be used in this simulation.

At the start of the simulation, both the upperarm and forearm are held in the horizontal position. The upperarm first flexes to 45° above the horizontal position at the 60^{th} data sample. It then extends to 90° below the horizontal at the 240^{th} data sample followed by a flexion back to the horizontal position at the 360^{th} data sample. Thereafter, the upperarm performs a medial rotation to 90° at the 420^{th} data sample. This is followed by a lateral rotation to 45° at 540^{th} data sample. At the same time from the 480^{th} data sample, the upperarm performs an extension to 45° below the horizontal at the 540^{th} data sample and remains in that position till the end of the simulation.

For the forearm, it first performs a flexion from 0° at the start to 45° at the 60^{th} data sample. It remains in that flexion position for 60 data samples. Thereafter it continues the flexion to 135° at the 180^{th} data sample. Following that, the forearm performs an extension back to 0° at the 240^{th} data sample. During this time, the forearm performs a pronation movement to -180° at the 120^{th} data sample followed by supination back to 0° at the 240^{th} data sample. From the 240^{th} data sample, the forearm performs a flexion to 45 ° at the 300^{th} data sample and extension back to 0° at the 360^{th} data sample, while doing a

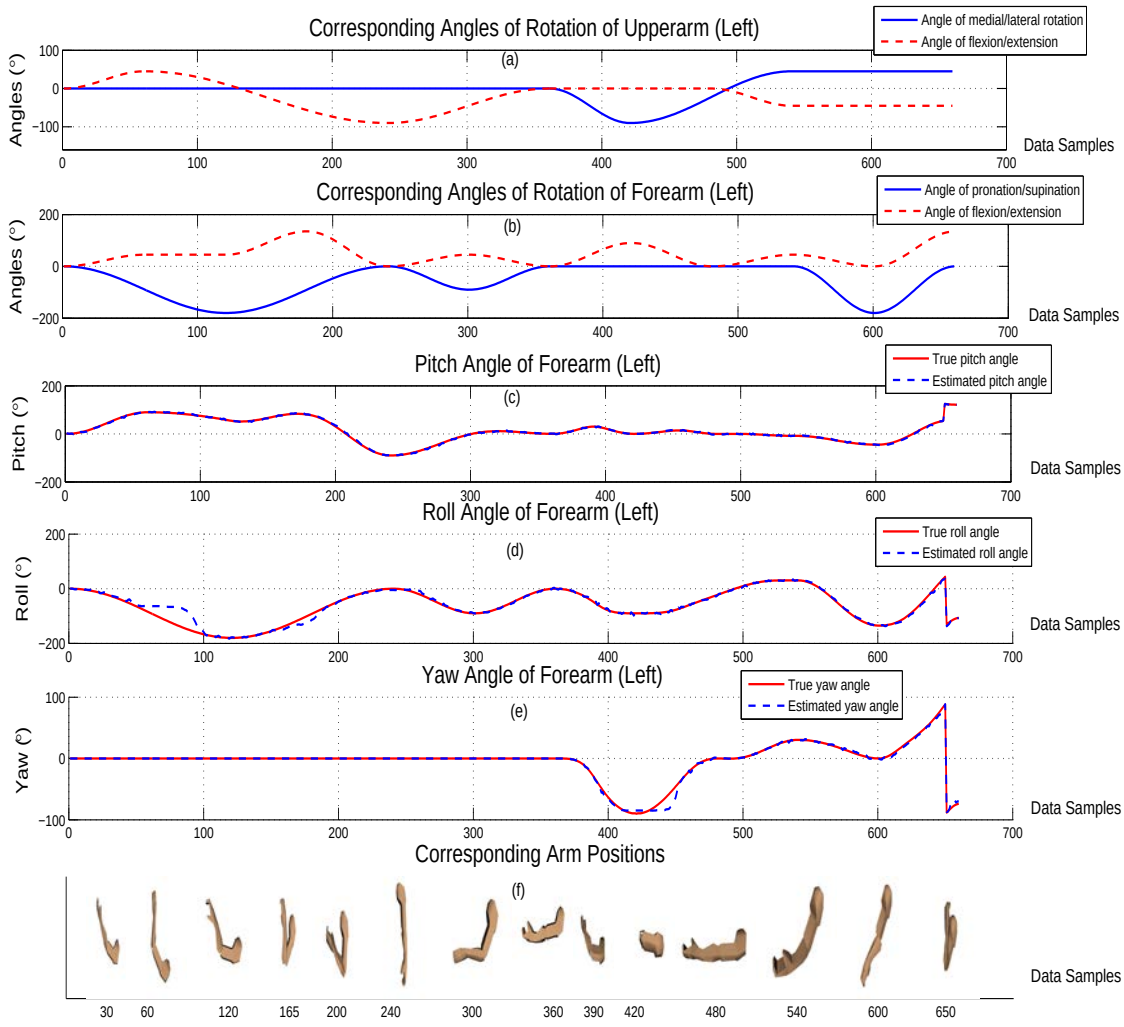

Figure 4.14. Simulated combination of flexion/ extension and pronation/ supination of forearm using the single angle-axis quaternion approach

pronation/supination motion to -90° and back to 0° at the same time. From 360th data sample, the upperarm performs a medial rotation and the forearm performs a flexion to 90° at the 420th data sample and extension back to 0° at the 480th data sample. From 480th data sample, while the arm is in a plane tilted from the vertical, the forearm undergoes a flexion to 90°, extension back to 0° and flexion to 135° at the end of the simulation. From 540th data sample, while the upperarm is laterally rotated 45°, the forearm performs a pronation/supination movement to -180° and back to 0° at the end of the simulation.

The equivalent roll, pitch and yaw angles of the forearm obtained using the single angle-axis quaternion method are shown in Fig 4.14c-e. It can be observed that the estimated pitch angle follows the true pitch angle closely. For the roll angle, it can be observed that when the the forearm is held up vertically at the 60th and 165th data sample (pitch angle = 90°) and held down vertically at the 240th data sample (pitch angle = -90°), the estimated roll angle diverges from the true roll angle. This is because the positions are in the singular states and any roll movement is a strict change of heading that cannot be measured using the accelerometer.

From the 360th data sample onwards, the upperarm is laterally and medially rotated, causing the plane of motion to be tilted from the vertical. This can be observed from the change in the yaw angle. It is noted that the estimated yaw angle still follows closely the true yaw angle, demonstrating that the measurement of the forearm is possible along a slanted plane by making use of the upperarm orientation. In addition, when the arm is medially rotated by 90° at the 420th data sample, the estimated yaw angle diverges from the true yaw angle. At this singular state, the forearm is horizontal and any subsequent flexion/extension movement is a strict change of heading which again cannot be measured using the accelerometer.

4.7.3 Ambiguity of Solutions

In this simulation study, the ambiguity of solutions obtained using the single angle-axis quaternion approach is investigated. The angles of flexion/extension and medial/lateral rotation of the upperarm are shown in Fig. 4.15a while the angles of flexion/extension and pronation/supination of the forearm are shown in Fig. 4.15b. The actual arm positions at different data samples are also depicted in Fig. 4.15e. The left upperarm first flexes from the horizontal position to 45° above the horizontal at the 20^{th} data sample. It is then extended to -90° at the 80^{th} data sample. No medial/lateral rotation of the upperarm is performed in this simulation. At the same time, the left forearm flexes from 0° to 45° at the 20^{th} data sample. It remains at the flexion position for 20 data samples and then continue its flexion to 135° at the 60^{th} data sample. Finally it is extended back to 0° at the 80^{th} data sample. During this time, the forearm simultaneously undergoes a pronation to -180° followed by supination back to 0°. The equivalent true and estimated pitch and roll angles of the forearm are shown in Fig. 4.15c-d. The plot of the yaw angle is omitted since it's value is zero throughout the simulation.

In this study, the forearm is in a vertical position with a pronation of -90° at the 20^{th} data sample. From the previous simulations, the behavior of the single angle-axis quaternion approach is known to be unpredictable in this singular state. It can be seen from Fig. 4.15c-d that the estimated pitch and roll angles are different from the true values from this point onwards. The estimated arm positions using the single angle-axis quaternion approach is depicted in Fig 4.15f. In this case, the estimated forearm positions differ only by a 180° rotation about the vertical axis from the actual forearm positions, where they are still in the same plane of motion but with a different heading. In addition, the estimated forearm starts to assume positions that are anatomically impossible for the human arm from the 50^{th} data sample. The results of this simulation demonstrate the limitation of

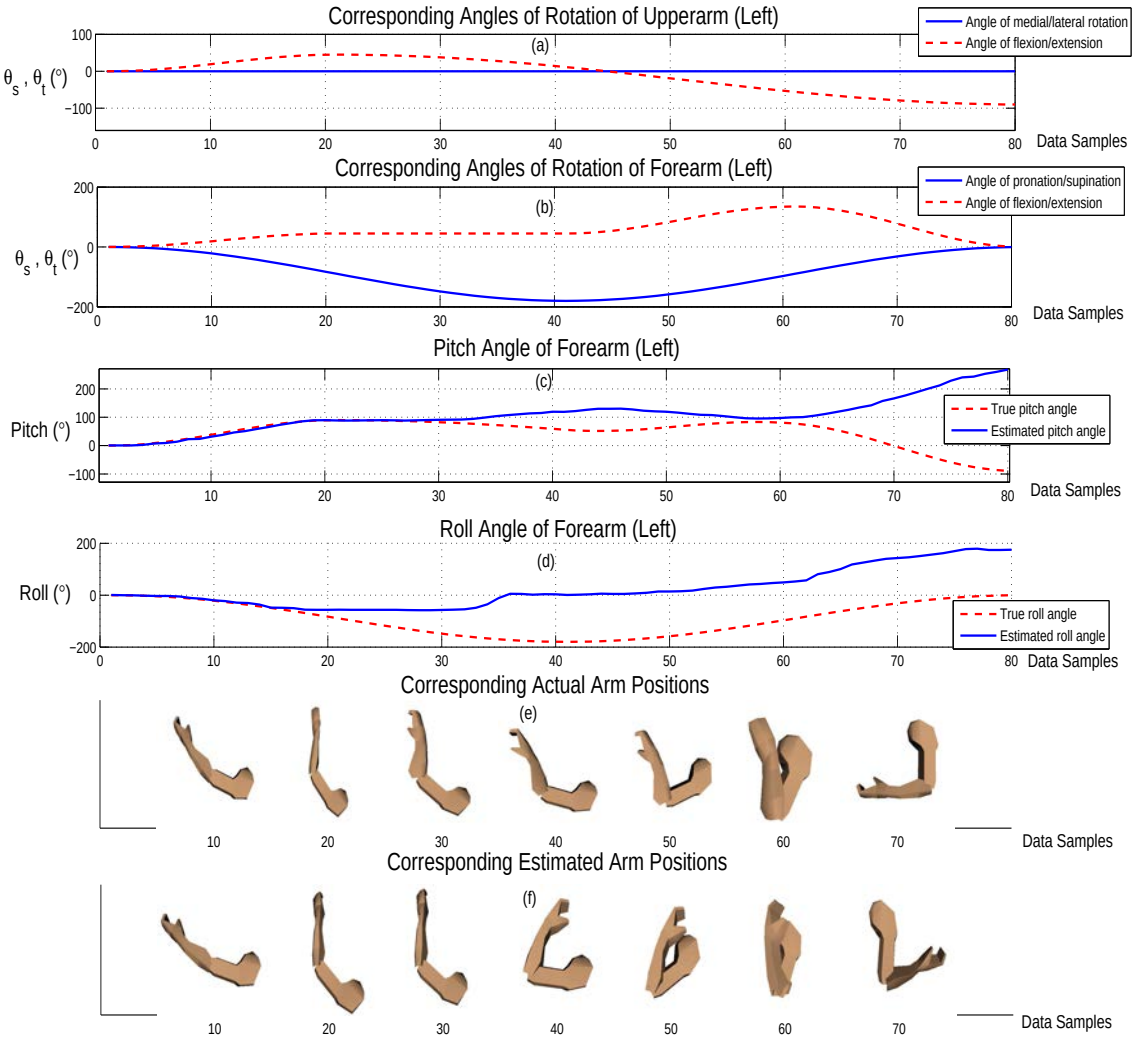

Figure 4.15. Ambiguity of solutions of forearm's orientation using the single angle-axis quaternion approach

the single angle-axis quaternion approach in resolving the ambiguity of solutions and the need for an approach that can reduce the ambiguity of solutions while factoring in the anatomical constraints of the human arm.

4.8 Summary

In this chapter, measurement of the human arm motions using the accelerometer has been investigated. Measurement in a single degree of freedom involves the determination of the inclination of the arm limb with respect to the vertical axis. In the static condition when the arm is stationary, the tilt measurement is performed by finding the component of the gravitational acceleration along the accelerometer's axes. When the arm is moving, measurement is possible if the acceleration due to the arm is negligible as compared to the gravitational acceleration. In addition, the effects of the angular velocity and acceleration of the arm can be minimized by placing the accelerometer close to the arm joints corresponding to the centre of rotation.

The accuracy of the wearable wireless sensor network system implementing the tilt determination algorithm has been evaluated under controlled rotations as well as benchmarked with a goniometer on an actual arm limb. Latency measurement of the system with multiple nodes demonstrate the ability of the system to model the human arm limb movements in real time. In addition, the low power consumption of each sensor node allows for long term monitoring of the subject.

Measurement of the arm's limb motion can be extended to two degrees of freedom but the measurement is limited to half the vertical plane. The orientation of the accelerometer node can be determined using either the method of rotation matrices or quaternions. Closed-form solutions using both methods have been presented. As a comparison, the method of quaternion uses a four-element tuple as compared to the nine elements using a rotation matrix and avoids the use of

trigonometric functions. Most importantly, the quaternion operator is inherently singularity free and can relate any two independent coordinate frames in $\mathbb{R}^3$.

The orientation measurement of the articulated human arm limbs, i.e the upperarm and forearm, has been investigated. The single angle-axis quaternion approach is presented where the single quaternion corresponding to the orientation of each arm limb is determined using constrained optimization. The motion of the upperarm is limited to the sagittal plane while the plane of motion of the forearm is determined by making use of the orientation of the upperarm. Numerical simulation results demonstrate the limitation of the single angle-axis approach in determining the arm limb's orientation in the singular states. Moreover, this approach is not able to resolve the ambiguity of solutions. The use of the single angle-axis quaternion approach will therefore entail the measurement of the arm motion to be restricted to half a plane.

In the next chapter, a factorized quaternion approach is proposed to overcome the limitations of the single angle-axis quaternion approach in the determination of the orientation of the articulated arm limb.

CHAPTER 5

Factorized Quaternion Approach for Determination of Arm Orientation

5.1 Introduction

In Chapter 4, several algorithms were proposed using the accelerometer for tilt measurement with single degree of freedom and measurement of orientation with two degrees of freedom. One of the major shortcomings of these methods is the occurrence of singularity when the heading axis of the accelerometer is vertical. This corresponds to the case that either the upperarm or forearm is in a vertical position. Consequently, the range of measurement is restricted to half a plane. In addition, the single angle-axis quaternion method was presented to determine the orientation of the upperarm and forearm. This method also suffers from the problem of divergence of solutions near the singular states and the inability to resolve the ambiguity of solutions.

To address the shortcomings of these methods, a novel factorized quaternion approach is proposed in this chapter for determining the arm orientation. In this approach, the single angle-axis quaternions as described in Section 4.6 is factorized into two principal axes quaternions corresponding to two equivalent arm motions. The main advantages of this new approach are:

1) Singularities arising from the use of the accelerometers can be detected and resolved for a transient state.

2) Anatomical constraints adhering to the range of arm motions can be incorporated to reduce the ambiguity in solutions.

3) Measurement of the arm movements can be limited to a single plane without the need for an additional optimization constraint.

In this chapter, the limitations of the accelerometer and the constraints of the human arm motion will first be reviewed. Subsequently, the problem formulation and the solution using factorized quaternion approach will be presented first for the upperarm and followed by the forearm. Detail simulation and experimental results evaluating the performance of the algorithm are presented at the end of this chapter.

5.2 Constraints Based on Accelerometer Limitation and Arm Anatomy

5.2.1 Limitations of the Accelerometer

In this chapter, the measurement is assumed to be conducted in static or slow-dynamics conditions where the external acceleration is negligible as compared to the acceleration due to gravity. This assumption is valid in applications such as rehabilitation since the motion of the patient is generally slow (with angular velocity less than $10°/s$). As the component of gravity along the axes is the same when the accelerometer is rotated about the vertical axis, the accelerometer is unable to determine the heading with respect to the vertical axis. Given this constraint, the typical tracking of the arm motion is restricted to a single plane.

5.2.2 Range of Motion of the Human Arm

In section 4.2, different types of arm movements have been described. In this section, the range of these movements with a view of incorporating this information

into the determination of arm movements shall be examined.

Tables 5.1 and 5.2 summarize the anatomical range of motion for the arm (shoulder joint) and forearm (elbow joint) [78] together with the constraints to be imposed for optimization. The range of motion can be either active in which the joint movement is caused by voluntary contraction of the muscles or passive in which the muscles are relaxed and the segment is moved by an external force, for example, that exerted by another person. For the forearm, both the active and passive range of flexion motion are given.

For the upperarm, it can move through approximately 165° to 180° of flexion and 30° to 60° of hyperextension in the sagittal plane. The amount of flexion is limited if the shoulder joint is externally rotated. With the shoulder joint maximally rotated, the arm can be flexed about 30°. It can also rotate internally and externally 60° to 90° for a total of 120° to 180° of rotation. The range of motion at the elbow in flexion and extension is approximately 145° for active flexion, 160° for passive flexion and 5° to 10° for hyperextension. The range of motion for supination and pronation is approximately 85° and 70° respectively [78].

TABLE 5.1
RANGE OF MOTION OF UPPERARM AND CONSTRAINTS IMPOSED

Arm (Shoulder Joint)	**Flexion**	**Hyperextension**	**Medial/Lateral Rotation**
Range of Motion	165° – 180°	30° – 60°	60° – 90°
Constraint Imposed	none	none	90°

Note: All angles are with respect to anatomical position

5.2.3 Summary of Constraints

Section 4.2 described the sagittal, transverse and frontal cardinal planes. In practice, there is no restriction for the number of planes through the body as long as

TABLE 5.2
RANGE OF MOTION OF FOREARM AND CONSTRAINTS IMPOSED

Forearm (Elbow Joint)	**Flexion**	**Hyper-extension**	**Pronation**	**Supination**
Range of Motion	145° (active) 160° (passive)	$5° - 10°$	70°	85°
Constraint Imposed	170°	10°	90°	90°

Note: All angles are with respect to anatomical position

it is useful for describing the joint or limb movements. In limiting the plane of motion for the upperlimb in this study, the sagittal plane was chosen since most planar or 2D analysis are concerned with motion in the sagittal plane. Notwithstanding, if it is desired to measure the motion in any other planes, it is possible to restrict the motion to another plane, e.g. the frontal plane for measurement of abduction/ adduction plane. Thus, the analysis in the sequel is also applicable with slight modification.

In determining the orientation of the upperarm, its internal and external rotation shall be restricted to 90° each for a total of 180° of rotation. No constraint is set for the flexion and extension of the shoulder joint.

The forearm's plane of motion is determined by the internal/external rotation of the upperarm. If there is no rotation of the upperarm, its plane of motion is the same as the upperarm, i.e. the sagittal plane. If the upperarm undergoes a lateral/medial rotation, the plane of motion is also rotated about the vertical. If the upperarm undergoes a flexion/extension in addition to lateral/medial rotation, the motion plane of the forearm is slanted with respect to the horizontal. The constraint of the forearm for its motion plane is therefore to be updated dynamically based on information of the upperarm's orientation.

For the anatomical constraint of the forearm, the maximum range of motion for pronation and supination is set to 90°. For the elbow joint, the range of motion

is limited to 10° of hyperextension to 170° of flexion.

5.3 Factorized Quaternion Approach

Given the sensor and anatomical constraints presented in Section 5.2, a new factorized quaternion algorithm is proposed in this section to determine the orientation of the arm limbs taking into consideration of these constraints.

Let the coordinate frames of the accelerometer attached to the upperarm and forearm be $\{^{U}x,^{U}y,^{U}z\}$ and $\{^{L}x,^{L}y,^{L}z\}$ respectively as shown in Fig. 5.1. The Z-axis of the fixed inertial reference frame is defined as pointing vertically. The X and Y-axes are defined as lying in the horizontal plane with X-axis pointing in the posterior direction of the human anatomical position.

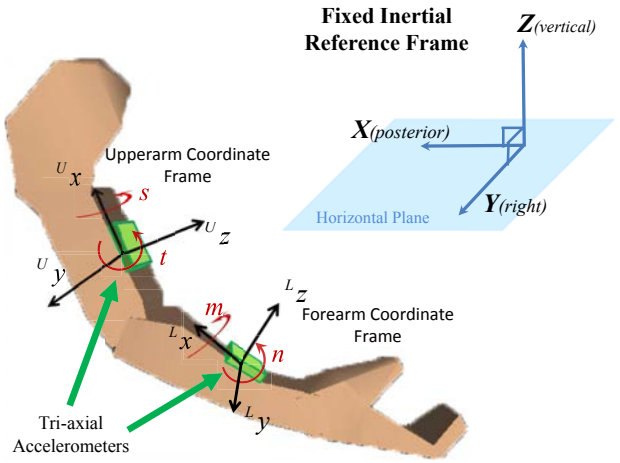

Figure 5.1. Diagram of right arm showing body and fixed inertial reference frames

5.3.1 Determination of Upperarm's Orientation

Problem Formulation

To address the shortcomings of the single angle-axis quaternion approach, the quaternion of the upperarm's rotation is factorized into its two principal axis quaternions as shown in Fig. 5.1. The quaternion s represents a rotation about the

${}^{U}x$-axis of the upperarm (corresponding to medial/lateral rotation). The quaternion t represents a rotation about the ${}^{U}y$-axis of the upperarm (corresponding to flexion/extension). The quaternions s and t are expressed as

$$s = \begin{pmatrix} s_1 \\ s_2 \\ 0 \\ 0 \end{pmatrix}, \quad t = \begin{pmatrix} t_1 \\ 0 \\ t_2 \\ 0 \end{pmatrix} \tag{5.1}$$

The corresponding angles of rotation for the upperarm can be calculated using (4.34) as

$$\theta_s = 2sign\,(s_2)\cos^{-1}s_1 \tag{5.2a}$$

$$\theta_t = 2sign\,(t_2)\cos^{-1}t_1 \tag{5.2b}$$

where $-90^\circ \leq \theta_s \leq 90^\circ$, $-180^\circ < \theta_t \leq 180^\circ$ and $sign\,()$ is the signum function.

Using the quaternion rotation operator as defined in (4.37), the output signal of the accelerometer expressed in terms of the gravitational acceleration is then given by:

$$s^*t^*\mathbf{g}ts = {}^{U}\mathbf{a} \tag{5.3}$$

where $\mathbf{g}$ is the normalized gravitational acceleration as in (4.25) and ${}^{U}\mathbf{a}$ is the normalized output signal of the accelerometer attached to the upperarm as in (4.47). They are reproduced below for ease of reference:

$$\mathbf{g} = \begin{pmatrix} 0 \\ 0 \\ -1 \end{pmatrix}, {}^{U}\mathbf{a} = \begin{pmatrix} {}^{U}a_x \\ {}^{U}a_y \\ {}^{U}a_z \end{pmatrix} \tag{5.4}$$

Substituting (5.1) into (5.3) and expanding the terms gives:

$$\begin{pmatrix} 2\left\|s\right\|_2^2 t_1 t_2 \\ -2s_1 s_2 \Delta_t \\ -\Delta_s \Delta_t \end{pmatrix} = \begin{pmatrix} {}^{U}a_x \\ {}^{U}a_y \\ {}^{U}a_z \end{pmatrix} \tag{5.5}$$

where

$$\Delta_s = s_1^2 - s_2^2 \tag{5.6a}$$

$$\Delta_t = t_1^2 - t_2^2 \tag{5.6b}$$

From (5.5), it is observed that when the upperarm is rotated about the ${}^{U}y$-axis by 90° or -90°, the value of Δ_t equals to zero. Thus the value of the quaternion s (rotation of the arm) cannot be determined. This agrees with the limitation that at this point any internal/external rotation of the upperarm is strictly a rotation about the vertical axis which cannot be resolved using an accelerometer. In the presence of noise and errors due to factors such as the offset and temperature biases of the accelerometer, (5.5) can be modified as

$$\begin{pmatrix} 2\left\|s\right\|_2^2 t_1 t_2 \\ -2s_1 s_2 \Delta_t \\ -\Delta_s \Delta_t \end{pmatrix} = \begin{pmatrix} {}^{U}a_x \\ {}^{U}a_y \\ {}^{U}a_z \end{pmatrix} + \begin{pmatrix} {}^{U}\eta_x \\ {}^{U}\eta_y \\ {}^{U}\eta_z \end{pmatrix} \tag{5.7}$$

where ${}^{U}\eta_x$, ${}^{U}\eta_y$, ${}^{U}\eta_z$ are the noise and error components in the respective x, y and z- axis of the accelerometer. From (5.7) the following constrained optimization problem is formulated:

Constraint Optimization

$$\min_{s,t} {}^{U}f(s,t) \;\text{ subject to } {}^{U}c(s,t) = \mathbf{0} \tag{5.8}$$

where ${}^{U}f : \mathbb{R}^4 \to \mathbb{R}$, ${}^{U}c : \mathbb{R}^4 \to \mathbb{R}^2$ and ${}^{U}f(s,t)$ is defined as

$${}^{U}f(s,t) = A^2 + B^2 + C^2 \tag{5.9}$$

where A, B, and C are variables defined as

$$A = 2\left\|s\right\|_2^2 t_1 t_2 - {}^{U}a_x \tag{5.10a}$$

$$B = 2s_1 s_2 \Delta_t + {}^{U}a_y \tag{5.10b}$$

$$C = \Delta_s \Delta_t + {}^{U}a_z \tag{5.10c}$$

and ${}^{U}c(s,t)$ describes the following constraint

$${}^{U}c(s,t) = \begin{bmatrix} \left\|s\right\|_2^2 - 1 \\ \left\|t\right\|_2^2 - 1 \end{bmatrix} \tag{5.11}$$

The constraints in (5.11) are to preserve the unity norm of the factorized quaternions. The local minimum is a critical point of the Lagrangian function

$${}^{U}\mathcal{L}\left(s,t,{}^{U}\boldsymbol{\lambda}\right) = {}^{U}f\left(s,t\right) - {}^{U}\boldsymbol{\lambda}^{T}\,{}^{U}c\left(s,t\right) \tag{5.12}$$

where ${}^{U}\boldsymbol{\lambda} \in \mathbb{R}^2$ is the vector of Lagrange multipliers. The first-order necessary condition for a critical point of the Lagrangian function can be expressed as

$$\nabla^{U}\mathcal{L}\left(s,t,{}^{U}\boldsymbol{\lambda}\right) = \begin{bmatrix} \nabla^{U}f\left(s,t\right) - {}^{U}\mathbf{J}_c{}^{T}\left(s,t\right){}^{U}\boldsymbol{\lambda} \\ {}^{U}c\left(s,t\right) \end{bmatrix} = \mathbf{0} \tag{5.13}$$

where $\nabla^{U}f(s,t)$ is the gradient of function ${}^{U}f(s,t)$ given by

$$\nabla^{U}f(s,t) = 4\begin{bmatrix} 2s_1 t_1 t_2 A - \Delta_t(s_2 B + s_1 C) \\ 2s_2 t_1 t_2 A - \Delta_t(s_1 B - s_2 C) \\ \left\|s\right\|_2^2 t_2 A - 2s_1 s_2 t_1 B - \Delta_s t_1 C \\ \left\|s\right\|_2^2 t_1 A + 2s_1 s_2 t_2 B + \Delta_s t_2 C \end{bmatrix} \tag{5.14}$$

and ${}^{U}\mathbf{J}_c(s,t)$ is the Jacobian of the function ${}^{U}c(s,t)$ as follow:

$${}^{U}\mathbf{J}_c(s,t) = 2\begin{bmatrix} s_1 & s_2 & 0 & 0 \\ 0 & 0 & t_1 & t_2 \end{bmatrix} \tag{5.15}$$

Newton's Method for Solving Constrained Optimization

With an initial estimate $(s_0, t_0, {}^U\boldsymbol{\lambda}_0)$, the Newton's method [87, 88] can be used to solve the constrained optimization problem (5.8)–(5.11). The linearized system to be solved at the k^{th} iteration for the Newton step is given by

$$\begin{bmatrix} {}^U\mathbf{B}\left(s_k, t_k, {}^U\boldsymbol{\lambda}_k\right) & -{}^U\mathbf{J}_c{}^T\left(s_k, t_k\right) \\ {}^U\mathbf{J}_c\left(s_k, t_k\right) & \mathrm{O} \end{bmatrix} \begin{bmatrix} {}^U\mathbf{p}_k \\ {}^U\boldsymbol{\lambda}_{k+1} \end{bmatrix} = - \begin{bmatrix} \nabla {}^Uf(s_k, t_k) \\ {}^Uc\left(s_k, t_k\right) \end{bmatrix} \tag{5.16}$$

where

$${}^U\mathbf{B}\left(s, t, {}^U\boldsymbol{\lambda}\right) = {}^U\mathbf{H}_f\left(s, t\right) - \sum_{i=1}^{2} \lambda_i {}^U\mathbf{H}_{c_i}\left(s, t\right) \tag{5.17}$$

In (5.17), ${}^UH_f\left(s, t\right)$ is the Hessian of ${}^Uf(s, t)$ given by

$${}^U\mathbf{H}_f(s, t) = 4\left({}^U\mathbf{D}_{H_f}\left(s, t\right) + {}^U\mathbf{H}_o(s, t) + {}^U\mathbf{H}_o{}^T(s, t)\right) \tag{5.18}$$

where

$${}^U\mathbf{H}_o(s, t) = \begin{bmatrix} 0 & {}^Uh_{12} & {}^Uh_{13} & {}^Uh_{14} \\ 0 & 0 & {}^Uh_{23} & {}^Uh_{24} \\ 0 & 0 & 0 & {}^Uh_{34} \\ 0 & 0 & 0 & 0 \end{bmatrix} \tag{5.19}$$

$${}^U\mathbf{D}_{H_f}\left(s, t\right) = diag \begin{pmatrix} 2\left[t_1t_2(A + 4s_1^2t_1t_2) + \Delta_t(\|s\|_2^2\,\Delta_t - \frac{1}{2}C)\right] \\ 2\left[t_1t_2(A + 4s_2^2t_1t_2) + \Delta_t(\|s\|_2^2\,\Delta_t + \frac{1}{2}C)\right] \\ 2\left[\|s\|_2^4\,t_2^2 + t_1^2(4s_1^2s_2^2 + \Delta_s^2) - s_1s_2B\right] - \Delta_sC \\ 2\left[\|s\|_2^4\,t_1^2 + t_2^2(4s_1^2s_2^2 + \Delta_s^2) + s_1s_2B\right] + \Delta_sC \end{pmatrix} \tag{5.20}$$

$$^{U}h_{12}=8s_1s_2t_1^2t_2^2 - \Delta_t B \tag{5.21a}$$

$$^{U}h_{13}=2\left[s_1t_2A - t_1(s_2B + s_1C) + s_1t_1\left\|s\right\|_2^2\left\|t\right\|_2^2\right] \tag{5.21b}$$

$$^{U}h_{14}=2\left[s_1t_1A + t_2(s_2B + s_1C) + s_1t_2\left\|s\right\|_2^2\left\|t\right\|_2^2\right] \tag{5.21c}$$

$$^{U}h_{23}=2\left[s_2t_2A - t_1(s_1B - s_2C) + s_2t_1\left\|s\right\|_2^2\left\|t\right\|_2^2\right] \tag{5.21d}$$

$$^{U}h_{24}=2\left[s_2t_1A + t_2(s_1B - s_2C) + s_2t_2\left\|s\right\|_2^2\left\|t\right\|_2^2\right] \tag{5.21e}$$

$$^{U}h_{34}=\left\|s\right\|_2^2 A \tag{5.21f}$$

Moreover, the values of the elements of the matrices $^{U}\mathbf{H}_{c_1}$ and $^{U}\mathbf{H}_{c_2}$ are constant and are given by

$$^{U}\mathbf{H}_{c_1} = 2\begin{bmatrix} 1 & 0 & 0 & 0 \\ 0 & 1 & 0 & 0 \\ 0 & 0 & 0 & 0 \\ 0 & 0 & 0 & 0 \end{bmatrix} \tag{5.22a}$$

$$^{U}\mathbf{H}_{c_2} = 2\begin{bmatrix} 0 & 0 & 0 & 0 \\ 0 & 0 & 0 & 0 \\ 0 & 0 & 1 & 0 \\ 0 & 0 & 0 & 1 \end{bmatrix} \tag{5.22b}$$

Eqn (5.16) can be regarded as a sequential quadratic programming problem with the 2×2 block matrix known as the *Karush-Kuhn-Tucker (KKT)* matrix [88]. To solve (5.16) directly while making use of the symmetry of the *KKT* matrix is to use a symmetric indefinite factorization since the *KKT* matrix is always indefinite when the number of contraints is greater than or equal to one. The symmetric indefinite factorization requires suitable permutation matrix which could be complicated. In this study, (5.16) is solved based on an indirect method known as the null space method [87]. The QR factorization of $^{U}\mathbf{J}_c^T(s_k, t_k)$ is first computed as

$$ {}^{U}\mathbf{J}_c{}^{T}(s_k, t_k) = \mathbf{Q}_k \begin{bmatrix} \mathbf{R}_k \\ \mathbf{O} \end{bmatrix} = \begin{bmatrix} \mathbf{Y}_k & \mathbf{Z}_k \end{bmatrix} \begin{bmatrix} \mathbf{R}_k \\ \mathbf{O} \end{bmatrix} \tag{5.23} $$

where $\mathbf{Y}_k$ and $\mathbf{Z}_k$ are 4×2 matrices. The columns of $\mathbf{Y}_k$ form an orthonormal basis for the range space of ${}^{U}\mathbf{J}_c{}^{T}(s_k, t_k)$ while the columns of $\mathbf{Z}_k$ form an orthonormal basis for the null space of ${}^{U}\mathbf{J}_c(s_k, t_k)$. As such, ${}^{U}\mathbf{p}_k$ can be partitioned into two components as

$$ {}^{U}\mathbf{p}_k = \mathbf{Y}_k \mathbf{p}_{Y_k} + \mathbf{Z}_k \mathbf{p}_{Z_k} \tag{5.24} $$

Substituting (5.24) into the second block row of the KKT system in (5.16) gives

$$ {}^{U}\mathbf{J}_c(s_k, t_k) \left(\mathbf{Y}_k \mathbf{p}_{Y_k} + \mathbf{Z}_k \mathbf{p}_{Z_k} \right) = \mathbf{R}_k^T \mathbf{p}_{Y_k} = -{}^{U}c(s_k, t_k) \tag{5.25} $$

which can be solved for ${}^{U}\mathbf{p}_{Y_k}$. Premultiplying the first block row of (5.16) by $\mathbf{Z}_k^T$ produces

$$ \left(\mathbf{Z}_k^T {}^{U}\mathbf{B}(s_k, t_k, {}^{U}\boldsymbol{\lambda}_k) \mathbf{Z}_k \right) \mathbf{p}_{Z_k} = -\mathbf{Z}_k^T \left(\nabla {}^{U}f(s_k, t_k) + {}^{U}\mathbf{B}(s_k, t_k, {}^{U}\boldsymbol{\lambda}_k) \mathbf{Y}_k {}^{U}\mathbf{p}_{Y_k} \right) \tag{5.26} $$

which can be solved for ${}^{U}\mathbf{p}_{Z_k}$. The reduced-Hessian matrix $\mathbf{Z}_k^T {}^{U}\mathbf{B}(s_k, t_k, {}^{U}\boldsymbol{\lambda}_k)\mathbf{Z}_k$ in (5.26) is not always positive definite if it started away from the constrained minimum. A modified Cholesky factorization on the KKT matrix on the null space method is adopted so that the Newton step is in a descent direction. An alternative is to use a Reduced-Hessian Quasi-Newton method to approximate the value of $\mathbf{Z}_k^T {}^{U}\mathbf{B}(s_k, t_k, {}^{U}\boldsymbol{\lambda}_k)\mathbf{Z}_k$ which may be more efficient by doing away with the calculation of second order derivatives. However, since the problem is small here, a modified Cholesky factorization approach is simpler and should more than suffice. Finally, premulitplying the first block row by $\mathbf{Y}_k^T$ yields

$$ \boldsymbol{R}_k {}^{U}\boldsymbol{\lambda}_{k+1} = \mathbf{Y}_k{}^{T} \left(\nabla {}^{U}f(s_k, t_k) + {}^{U}\mathbf{B}(s_k, t_k, {}^{U}\boldsymbol{\lambda}_k) {}^{U}\mathbf{p}_k \right) \tag{5.27} $$

which can be solved for ${}^{U}\boldsymbol{\lambda}_{k+1}$. The use of orthogonal matrices in the null space method avoids the potential loss of information and degradation of conditioning associated with methods such as the range-space method.

A ℓ_1 merit function is used to control the step size of the Newton step which takes the following form

$$\phi_1\left(s_k, t_k, \mu\right) = {}^{U}f\left(s_k, t_k\right) + \mu \left\| {}^{U}c\left(s_k, t_k\right)\right\|_1 \tag{5.28}$$

where $\mu > 0$ is the penalty parameter. The step length $\alpha_k {}^{U}\mathbf{p}_k$ is accepted if the following sufficient decrease condition holds for some $\rho \in (0, 1)$:

$$\phi_1\left(s_{k+1}, t_{k+1}, \mu\right) \leqslant \phi_1\left(s_k, t_k, \mu\right) + \rho\alpha_k D\left(\phi_1\left(s_k, t_k, \mu\right); {}^{U}\mathbf{p}_k\right) \tag{5.29}$$

where $D\left(\phi_1\left(s_k, t_k, \mu\right); {}^{U}\mathbf{p}_k\right)$ denotes the directional derivative of $\phi_1\left(s_k, t_k, \mu\right)$ in the direction of ${}^{U}\mathbf{p}_k$. It can be shown to be

$$D\left(\phi_1\left(s_k, t_k, \mu\right); {}^{U}\mathbf{p}_k\right) = \nabla {}^{U}f(s_k, t_k)^{T} {}^{U}\mathbf{p}_k - \mu \left\| {}^{U}c(s_k, t_k)\right\|_1 \tag{5.30}$$

The initial estimate for α is set to 1 to allow full Newton steps to be taken if the sufficient decrease condition is met.

Enhancing the accuracy of the estimate

When using the ℓ_1 merit function, a phenomenon known as the Maratos effect may impede the progress of the optimization algorithm [89]. The Maratos effect happens when a step is computed that makes good progress towards a solution but is rejected as it fails to reduce the merit function. This can slow the optimization process by interfering with good steps away from the solution and preventing superlinear convergence. A second-order correction strategy computed at ${}^{U}c((s_k, t_k) + \mathbf{p}_k)$ that decreases the constraint violation is used and is described as follows. Suppose a step has been computed using (5.16). If this step yields

an increase in the merit function $\phi_1(s_k, t_k, \mu)$, one possible reason is that the first order linear approximation to the constraints is not sufficiently accurate or is insignificant. To overcome this, (5.16) is resolved by replacing the linear terms, ${}^{U}c_i(s_k, t_k) + \nabla {}^{U}c_i(s_k, t_k)^T \mathbf{p}$, in the second block row corresponding to the constraints with the quadratic approximation

$$ {}^{U}c_i(s_k, t_k) + \nabla {}^{U}c_i(s_k, t_k)^T \mathbf{p} + \frac{1}{2}\mathbf{p}^T \mathbf{H}_{c_i}(s_k, t_k)\mathbf{p} \tag{5.31} $$

for $i = 1, 2$. Instead of solving for $\mathbf{p}$ in the quadratic constraints in (5.31), the constraints at $(s_k, t_k) + {}^{U}\mathbf{p}_k$ are evaluated and the following approximations shall be used. From Taylor's theorem,

$$ {}^{U}c_i\left((s_k, t_k) + {}^{U}\mathbf{p}_k\right) \approx {}^{U}c_i(s_k, t_k) + \nabla {}^{U}c_i(s_k, t_k)^T {}^{U}\mathbf{p}_k + \frac{1}{2} {}^{U}\mathbf{p}_k{}^T {}^{U}\mathbf{H}_{c_i}(s_k, t_k) {}^{U}\mathbf{p}_k \tag{5.32} $$

Assuming that the second-order step $\mathbf{p}$ is not too far off from ${}^{U}\mathbf{p}_k$, the last term in (5.31) can be approximated as

$$ \mathbf{p}^T {}^{U}\mathbf{H}_{c_i}(s_k, t_k)\mathbf{p} = {}^{U}\mathbf{p}_k{}^T {}^{U}\mathbf{H}_{c_i}(s_k, t_k) {}^{U}\mathbf{p}_k \tag{5.33} $$

Substituting (5.33) in (5.31) and using (5.32), the new constraints for the second-order correction subproblem can be obtained as

$$ \nabla {}^{U}c_i(s_k, t_k)^T \mathbf{p} + d_i = 0 \tag{5.34} $$

where $d_i = {}^{U}c_i((s_k, t_k) + {}^{U}\mathbf{p}_k) - \nabla {}^{U}c_i(s_k, t_k)^T {}^{U}\mathbf{p}_k$ for $i = 1, 2$.

The cost of this second-order correction includes the evaluation of the constraints at $(s_k, t_k) + {}^{U}\mathbf{p}_k$ and the linear algebra required to solve for $\mathbf{p}$. Therefore, it is not recommended to implement it everytime the merit function increases. The strategy applied here is that if the full step $\alpha_k = 1$ does not produce the decrease in the merit function, the second order correction step is performed before

modifying α_k. The second order correction step is discarded if it does not produce a reduction in the merit function.

The pseudocode for the implementation of the factorized quaternion approach for determination of the upperarm's orientation is given in Algorithm 5.1.

5.3.2 Determination of Forearm's Orientation

For the forearm, the movements are not restricted to a vertical plane unlike the upperarm. When the upperarm undergoes a flexion/extension followed by a medial/lateral rotation, the plane of motion of the forearm for flexion/extension and medial/lateral rotations will be along a slanted plane. This implies that the heading of the forearm will change with respect to the vertical. Even though the accelerometer is unable to determine the heading, it shall be shown that the orientation of the forearm along the slanted plane can still be obtained based on the orientation of the upperarm if the rotation is not strictly about a vertical axis. This novel approach is presented in the following section.

Problem Formulation

To determine the orientation of the forearm, the three factorized principal axis quaternions, m, n and n_0, are defined as

$$m = \begin{pmatrix} m_1 \\ m_2 \\ 0 \\ 0 \end{pmatrix}, \quad n = \begin{pmatrix} n_1 \\ 0 \\ n_2 \\ 0 \end{pmatrix}, \quad n_0 = \begin{pmatrix} \cos 5^\circ \\ 0 \\ -\sin 5^\circ \\ 0 \end{pmatrix} \tag{5.35}$$

where m is the principal axis quaternion representing the rotation about the ${}^Lx$-axis of the forearm (pronation/supination), n is the principal axis quaternion representing a rotation about the ${}^Ly$-axis of the forearm (flexion/extension) and n_o is a quaternion representing an offset rotation of -10° about the ${}^Ly$-axis as

Algorithm 5.1: Factorized Quaternion Algorithm for Determination of Upperarm's Orientation

Choose parameters $\rho \in (0,1)$, $\tau \in (0,1)$ and $\mu > 0$
Choose initial estimates $(s_0, t_0, {}^{U}\boldsymbol{\lambda}_0)$, Set $k \leftarrow 0$
repeat
  Evaluate $\nabla {}^{U}f(s_k,t_k)$,${}^{U}\mathbf{B}\left(s_k,t_k,{}^{U}\boldsymbol{\lambda}_k\right)$, ${}^{U}c(s_k,t_k)$ and ${}^{U}\mathbf{J}_c(s_k,t_k)$
  `// Null Space Method`
  begin
    Compute QR factorization of ${}^{U}\mathbf{J}_c(s_k,t_k)$ to obtain $\mathbf{Y}_k$,$\mathbf{Z}_k$ and $\boldsymbol{R}_k$.
    Solve (5.25) to obtain $\mathbf{p}_{Y_k}$
    if $\mathbf{Z}_k^{T\,U}\mathbf{B}(s_k,t_k,{}^{U}\boldsymbol{\lambda}_k)\mathbf{Z}_k \leq 0$
      Perform modified Cholesky factorization on $\mathbf{Z}_k^{T\,U}\mathbf{B}(s_k,t_k,{}^{U}\boldsymbol{\lambda}_k)\mathbf{Z}_k$
    endif
    Solve (5.26) to obtain $\mathbf{p}_{Z_k}$
    Set ${}^{U}\mathbf{p}_k \leftarrow \mathbf{Y}_k\mathbf{p}_{Y_k} + \mathbf{Z}_k\mathbf{p}_{Z_k}$
    Solve (5.27) to obtain ${}^{U}\boldsymbol{\lambda}_{k+1}$
    Set ${}^{U}\delta_k \leftarrow {}^{U}\boldsymbol{\lambda}_{k+1} - {}^{U}\boldsymbol{\lambda}_k$
  end
  `// Line Search`
  begin
    Set $\alpha_k \leftarrow 1$
    `// Check for sufficient decrease condition`
    if $\phi_1\left((s_k,t_k) + \alpha_k {}^{U}\mathbf{p}_k, \mu\right) > \phi_1\left(s_k,t_k,\mu\right) + \rho\alpha_k D\left(\phi_1\left(s_k,t_k,\mu\right); {}^{U}\mathbf{p}_k\right)$
      `// Second-order Correction`
      Compute $\mathbf{p}$ using (5.34) in (5.16)
      if $\phi_1\left((s_k,t_k)+\mathbf{p},\mu\right) \leqslant \phi_1\left(s_k,t_k,\mu\right) + \rho D\left(\phi_1\left(s_k,t_k,\mu\right); {}^{U}\mathbf{p}_k\right)$
        Set $(s_{k+1},t_{k+1}) \leftarrow (s_k,t_k) + \mathbf{p}$
      else
        while
        $\phi_1\left((s_k,t_k) + \alpha_k {}^{U}\mathbf{p}_k, \mu\right) > \phi_1\left(s_k,t_k,\mu\right) + \rho\alpha_k D\left(\phi_1\left(s_k,t_k,\mu\right); {}^{U}\mathbf{p}_k\right)$
          $\alpha_k \leftarrow \tau\alpha_k$ `// Backtracking`
        endw
        Set $(s_{k+1},t_{k+1}) \leftarrow (s_k,t_k) + \alpha_k {}^{U}\mathbf{p}_k$
      endif
    else
      Set $(s_{k+1},t_{k+1}) \leftarrow (s_k,t_k) + \alpha_k {}^{U}\mathbf{p}_k$
    endif
    Set ${}^{U}\boldsymbol{\lambda}_{k+1} \leftarrow {}^{U}\boldsymbol{\lambda}_k + \alpha_k {}^{U}\delta_k$
  end
  $k \leftarrow k+1$
until *a convergence test is satisfied*

shown in Fig. 5.1. Using the quaternion rotation operator as defined in (4.37), the normalized accelerometer (attached to the forearm) output, ${}^{L}\mathbf{a}$, in terms of the gravitational acceleration, upperarm principal axes quaternions and forearm principal axes quaternions is given by

$$m^{*}n^{*}{n_o}^{*}\left(s^{*}t^{*}\mathbf{g}ts\right)n_o nm={}^{L}\mathbf{a} \tag{5.36}$$

The corresponding angle of rotations for the forearm can be determined using (4.34) as

$$\theta_m = 2sign\left(m_2\right)\cos^{-1}m_1 \tag{5.37a}$$

$$\theta_n = 2sign\left(n_2\right)\cos^{-1}n_1 \tag{5.37b}$$

$$\theta_{n-} = \theta_n - 10^{\circ} \tag{5.37c}$$

where $0^{\circ} \leq \theta_m \leq 180^{\circ}$ for the right forearm, $-180^{\circ} \leq \theta_m \leq 0^{\circ}$ for the left forearm , $0^{\circ} \leq \theta_n \leq 180^{\circ}$ and $-10^{\circ} \leq \theta_{n-} \leq 170^{\circ}$ (same for both left and right forearms).

Using the principal quaternions calculated for the upperarm (with a hat sign to denote estimated values), the vector $\mathbf{v}$ is defined as

$$\mathbf{v} = \begin{pmatrix} v_1 \\ v_2 \\ v_3 \end{pmatrix} = {n_o}^{*}\hat{s}^{*}\hat{t}^{*}\mathbf{g}\hat{t}\hat{s}n_o \tag{5.38}$$

Combining (5.36) and (5.38) and taking into account the presence of noise, the following expression is obtained:

$$m^{*}n^{*}\mathbf{v}nm={}^{L}\mathbf{a}+{}^{L}\eta \tag{5.39}$$

Substituting (5.35) and (5.38) into (5.39) produces

$$\Rightarrow \begin{pmatrix} \|m\|_2^2 \, \sigma \\ \Delta_m \beta + 2 m_1 m_2 \gamma \\ -2 m_1 m_2 \beta + \Delta_m \gamma \end{pmatrix} = \begin{pmatrix} {}^L a_x \\ {}^L a_y \\ {}^L a_z \end{pmatrix} + \begin{pmatrix} {}^L \eta_x \\ {}^L \eta_y \\ {}^L \eta_z \end{pmatrix} \tag{5.40}$$

where

$$\Delta_m = m_1^2 - m_2^2 \tag{5.41a}$$

$$\Delta_n = n_1^2 - n_2^2 \tag{5.41b}$$

$$\sigma = (v_1 \Delta_n - 2 v_3 n_1 n_2) \tag{5.41c}$$

$$\beta = v_2 \, \|n\|_2^2 \tag{5.41d}$$

$$\gamma = (v_3 \Delta_n + 2 v_1 n_1 n_2) \tag{5.41e}$$

The formulation in (5.40) allows for observation of the singularities that arise when using accelerometers to determine the orientation of the forearm. The first singularity occurs when $v_1 = v_3 = 0$ which makes the value of the quaternion n undeterminable. This is the case when the upperarm is in the horizontal position and medially rotated 90° and any flexion/extension of the forearm is thus a pure rotation about the vertical axis. The second singularity occurs when $v_2 = 0$ and $\gamma = 0$ which makes the value of the quaternion m unresolvable. This is the case when the forearm is in the vertical position and thus any pronation/supination motion is a rotation about the vertical axis. The constrained optimization problem can now be stated as follows:

Constraint Optimization

$$\min_{m,n} {}^L f(m, n) \text{ subject to } {}^L c(m, n) = \mathbf{0} \tag{5.42}$$

where ${}^{L}f : \mathbb{R}^4 \to \mathbb{R}$, ${}^{L}c : \mathbb{R}^4 \to \mathbb{R}^2$ and ${}^{L}f(m,n)$ is defined as

$$ {}^{L}f(m,n) = D^2 + E^2 + F^2 \tag{5.43} $$

where

$$ D = \|m\|_2^2 \sigma - {}^{L}a_x \tag{5.44a} $$

$$ E = \Delta_m \beta + 2m_1 m_2 \gamma - {}^{L}a_y \tag{5.44b} $$

$$ F = -2m_1 m_2 \beta + \Delta_m \gamma - {}^{L}a_z \tag{5.44c} $$

and ${}^{L}c(m,n)$ describes the equality constraint and is given by

$$ {}^{L}c(m,n) = \begin{bmatrix} \|m\|_2^2 - 1 \\ \|n\|_2^2 - 1 \end{bmatrix} \tag{5.45} $$

Solving the Constraint Optimization Problem

With the given optimization problem (5.42) - (5.45), it can be solved using the Newton's method similar to the upperarm with the exception that the gradient function of ${}^{L}f(m,n)$ is now given by

$$ \nabla {}^{L}f(m,n) = 4 \begin{bmatrix} Dm_1\sigma + E\zeta_1 + F\zeta_2 \\ Dm_2\sigma + E\zeta_2 - F\zeta_1 \\ D\|m\|_2^2 \delta_1 + E\Omega_1 + F\Lambda_1 \\ -D\|m\|_2^2 \delta_2 + E\Omega_2 + F\Lambda_2 \end{bmatrix} \tag{5.46} $$

where

$$\delta_1 = v_1 n_1 - v_3 n_2 \tag{5.47a}$$

$$\delta_2 = v_3 n_1 + v_1 n_2 \tag{5.47b}$$

$$\zeta_1 = m_1 \beta + m_2 \gamma \tag{5.47c}$$

$$\zeta_2 = -m_2 \beta + m_1 \gamma \tag{5.47d}$$

$$\Omega_1 = v_2 \Delta_m n_1 + 2 m_1 m_2 \delta_2 \tag{5.47e}$$

$$\Omega_2 = v_2 \Delta_m n_2 + 2 m_1 m_2 \delta_1 \tag{5.47f}$$

$$\Lambda_1 = -2 v_2 m_1 m_2 n_1 + \Delta_m \delta_2 \tag{5.47g}$$

$$\Lambda_2 = -2 v_2 m_1 m_2 n_2 + \Delta_m \delta_1 \tag{5.47h}$$

and the new Hessian function is

$${}^{L}\mathbf{H}_f(m,n) = 4\left({}^{L}\mathbf{D}_{H_f}(m,n) + {}^{L}\mathbf{H}_o(m,n) + {}^{L}\mathbf{H}_o{}^{T}(m,n)\right) \tag{5.48}$$

where

$${}^{L}\mathbf{D}_{H_f}(m,n) = diag \begin{pmatrix} 2\left[(m_1\sigma)^2 + {\zeta_1}^2 + {\zeta_2}^2\right] + D\sigma + E\beta + F\gamma \\ 2\left[(m_2\sigma)^2 + {\zeta_1}^2 + {\zeta_2}^2\right] + D\sigma - E\beta - F\gamma \\ \|m\|_2^2\left(2\|m\|_2^2{\delta_1}^2 + Dv_1\right) + 2\left({\Omega_1}^2 + {\Lambda_1}^2\right) + E(v_2\Delta_m + 2v_3 m_1 m_2) + F(v_3\Delta_m - 2v_2 m_1 m_2) \\ \|m\|_2^2\left(2\|m\|_2^2{\delta_2}^2 - Dv_1\right) + 2\left({\Omega_2}^2 + {\Lambda_2}^2\right) + E(v_2\Delta_m - 2v_3 m_1 m_2) - F(v_3\Delta_m + 2v_2 m_1 m_2) \end{pmatrix} \tag{5.49}$$

$${}^{L}\mathbf{H}_o(m,n) = \begin{bmatrix} 0 & {}^{L}h_{12} & {}^{L}h_{13} & {}^{L}h_{14} \\ 0 & 0 & {}^{L}h_{23} & {}^{L}h_{24} \\ 0 & 0 & 0 & {}^{L}h_{34} \\ 0 & 0 & 0 & 0 \end{bmatrix} \tag{5.50}$$

$$^{L}h_{12}=2m_1m_2\sigma^2+E\gamma-F\beta \tag{5.51a}$$

$$^{L}h_{13}=2\big[m_1\big(\|m\|_2^2\sigma+D\big)\delta_1+\Omega_1\zeta_1+\Lambda_1\zeta_2+E(v_2m_1n_1+m_2\delta_2)+F(-v_2m_2n_1+m_1\delta_2)\big] \tag{5.51b}$$

$$^{L}h_{14}=2\big[-m_1\big(\|m\|_2^2\sigma+D\big)\delta_2+\Omega_2\zeta_1+\Lambda_2\zeta_2+E(v_2m_1n_2+m_2\delta_1)+F(-v_2m_2n_2+m_1\delta_1)\big] \tag{5.51c}$$

$$^{L}h_{23}=2\big[m_2\big(\|m\|_2^2\sigma+D\big)\delta_1+\Omega_1\zeta_2-\Lambda_1\zeta_1+E(-v_2m_2n_1+m_1\delta_2)-F(v_2m_1n_1+m_2\delta_2)\big] \tag{5.51d}$$

$$^{L}h_{24}=2\big[-m_2\big(\|m\|_2^2\sigma+D\big)\delta_2+\Omega_2\zeta_2-\Lambda_2\zeta_1+E(-v_2m_2n_2+m_1\delta_1)-F(v_2m_1n_2+m_2\delta_1)\big] \tag{5.51e}$$

$$^{L}h_{34}=-\|m\|_2^2\big(2\|m\|_2^2\delta_1\delta_2+Dv_3\big)+2(\Omega_1\Omega_2+\Lambda_1\Lambda_2+Ev_1m_1m_2)+Fv_1\Delta_m \tag{5.51f}$$

The Jacobian function and Hessian of $^{L}c(m,n)$ are similar to the upperarm case as in (5.15) and (5.22) with the quaternions s and t, replaced by m and n respectively. It can also be observed that this formulation is the same as the upperarm if $v_1 = v_2 = 0$ and $v_3 = -1$. Thus the problem for the forearm can be treated as a general case.

The pseudocode for the implementation is given in Algorithm 5.2.

5.3.3 Implementation Considerations and Singularity Resolution

During system startup, the initial estimate for the quaternions can be taken as (1,0,0,0) while keeping the arm horizontally. Thereafter, the initial estimate for each data set for both accelerometers is taken to be the estimate of the quaternions from the previous sample.

Singularity Resolution

One key advantage of the proposed factorized quaternion approach over the single angle-axis quaternion approach is that the singularities arising from the use of the accelerometer can be resolved. Assuming that the motion of the upperarm is continuous and the singularity is transient, the value of s_{k+1} is set to that of the

Algorithm 5.2: Factorized Quaternion Algorithm for Determination of Forearm's Orientation

Obtain estimates of s and t from Algorithm 5.1 and evaluate $\mathbf{v}$ using (5.38)
Choose parameters $\rho \in (0,1)$, $\tau \in (0,1)$ and $\mu > 0$
Choose initial estimates $(m_0, n_0, {}^{L}\boldsymbol{\lambda}_0)$, Set $k \leftarrow 0$
repeat
  Evaluate $\nabla {}^{L}f(m_k, n_k)$,${}^{L}\mathbf{B}\,(m_k, n_k, {}^{L}\boldsymbol{\lambda}_k)$, ${}^{L}c(m_k, n_k)$ and ${}^{L}\mathbf{J}_c(m_k, n_k)$
  `// Null Space Method`
  begin
    Compute QR factorization of ${}^{L}\mathbf{J}_c(m_k, n_k)$ to obtain $\mathbf{Y}_k$,$\mathbf{Z}_k$ and $\boldsymbol{R}_k$.
    Solve $\mathbf{R}_k^T \mathbf{p}_{Y_k} = -{}^{L}c(m_k, n_k)$ to obtain $\mathbf{p}_{Y_k}$
    if $\mathbf{Z}_k^T {}^{U}\mathbf{B}(m_k, n_k, {}^{L}\boldsymbol{\lambda}_k)\mathbf{Z}_k \leq 0$
      Perform modified Cholesky factorization on $\mathbf{Z}_k^T {}^{L}\mathbf{B}(s_k, t_k, {}^{L}\boldsymbol{\lambda}_k)\mathbf{Z}_k$
    endif
    Solve (5.26), replacing ${}^{U}\mathbf{B}(s_k, t_k, {}^{U}\boldsymbol{\lambda}_k)$ with ${}^{L}\mathbf{B}(m_k, n_k, {}^{L}\boldsymbol{\lambda}_k)$ and $\nabla {}^{U}f(s_k, t_k)$ with $\nabla {}^{L}f(m_k, n_k)$ to obtain $\mathbf{p}_{Z_k}$
    Set ${}^{L}\mathbf{p}_k \leftarrow \mathbf{Y}_k \mathbf{p}_{Y_k} + \mathbf{Z}_k \mathbf{p}_{Z_k}$
    Solve (5.27), replacing ${}^{U}\mathbf{B}(s_k, t_k, {}^{U}\boldsymbol{\lambda}_k)$ with ${}^{L}\mathbf{B}(m_k, n_k, {}^{L}\boldsymbol{\lambda}_k)$, $\nabla {}^{U}f(s_k, t_k)$ with $\nabla {}^{L}f(m_k, n_k)$ and ${}^{U}\mathbf{p}_k$ with ${}^{L}\mathbf{p}_k$ to obtain ${}^{L}\boldsymbol{\lambda}_{k+1}$
    Set ${}^{L}\delta_k \leftarrow {}^{L}\boldsymbol{\lambda}_{k+1} - {}^{L}\boldsymbol{\lambda}_k$
  end
  `// Line Search`
  begin
    Set $\alpha_k \leftarrow 1$
    `// Check for sufficient decrease condition`
    if
    $\phi_1\left((m_k, n_k) + \alpha_k {}^{L}\mathbf{p}_k, \mu\right) > \phi_1\left(m_k, n_k, \mu\right) + \rho\alpha_k D\left(\phi_1\left(m_k, n_k, \mu\right); {}^{L}\mathbf{p}_k\right)$
      `// Second-order Correction`
      Compute $\mathbf{p}$ using $\nabla {}^{L}c_i(m_k, n_k)^T \mathbf{p} + d_i = 0$ where
      $d_i = {}^{L}c_i((m_k, n_k) + {}^{L}\mathbf{p}_k) - \nabla {}^{L}c_i(m_k, n_k)^T {}^{L}\mathbf{p}_k$ for $i = 1, 2$.
      if $\phi_1\left((m_k, n_k) + \mathbf{p}, \mu\right) \leqslant \phi_1\left(m_k, n_k, \mu\right) + \rho D\left(\phi_1\left(m_k, n_k, \mu\right); {}^{L}\mathbf{p}_k\right)$
        Set $(m_{k+1}, n_{k+1}) \leftarrow (m_k, n_k) + \mathbf{p}$
      else
        while
        $\phi_1\left((m_k, n_k) + \alpha_k {}^{L}\mathbf{p}_k, \mu\right) > \phi_1\left(m_k, n_k, \mu\right) + \rho\alpha_k D\left(\phi_1\left(m_k, n_k, \mu\right); {}^{L}\mathbf{p}_k\right)$
          $\alpha_k \leftarrow \tau\alpha_k$ `// Backtracking`
        endw
        Set $(m_{k+1}, n_{k+1}) \leftarrow (m_k, n_k) + \alpha_k {}^{L}\mathbf{p}_k$
      endif
    else
      Set $(m_{k+1}, n_{k+1}) \leftarrow (m_k, n_k) + \alpha_k {}^{L}\mathbf{p}_k$
    endif
    Set ${}^{L}\boldsymbol{\lambda}_{k+1} \leftarrow {}^{L}\boldsymbol{\lambda}_k + \alpha_k {}^{L}\delta_k$
  end
  $k \leftarrow k + 1$
until *a convergence test is satisfied*

quaternion at the previous sample, s_k, when $\Delta_t < \epsilon_u$ where ϵ_u is a small value. Similarly for the forearm, when $v_1 < \epsilon_{v_1}$ and $v_3 < \epsilon_{v_3}$, n_{k+1} takes on the value of n_k. When $v_2 < \epsilon_{v_2}$ and $\gamma < \epsilon_\gamma$, the value of m_{k+1} is taken as m_k.

Ambiguity Resolution

For motion limited to a single plane, each accelerometer reading corresponds to two different orientation. Implementing the constraint given in Section 5.2.3 on the range of motion has then the advantage of reducing the ambiguity by reducing the solution space that is outside of the anatomical limits. This can be incorporated in the factorized quaternion approach as shown in Table 5.3.

For the upperarm, if $\theta_s > 90°$, it is capped as $90°$. Likewise if $\theta_s < -90°$, it is taken as $-90°$. For the forearm, if $\theta_n > 180°$, θ_n is taken to be $360° - \theta_n$. Similarly if $\theta_n < 0°$, it is also taken to be $-\theta_n$. For θ_m, it is taken to be $0°$ if $\theta_m < 0$ (right forearm) or $\theta_m > 0$ (left forearm). Implemented in terms of the factorized quaternions, $s = (1, 0, 1, 0)/\sqrt{2}$ if $s_2 > 1/\sqrt{2}$ and $s = (1, 0, -1, 0)/\sqrt{2}$ if $s_2 < -1/\sqrt{2}$, $n_2 = -n_2$ if $n_2 < 0$ and $m = (1, 0, 0, 0)$ if $m_2 < 0$ (right forearm) or $m_2 > 0$ (left forearm). This strategy inverts the estimated value of θ_n onto another solution space so that the next iteration will yield the value of θ_n and θ_m in the desired solution space.

TABLE 5.3
STRATEGY FOR AMBIGUITY RESOLUTION

Angle	**Factorized Quaternion**
$\theta_s > 90° \rightarrow \theta_s = 90°$ $\theta_s < -90° \rightarrow \theta_s = -90°$	$s_2 > 1/\sqrt{2} \rightarrow s = (1, 0, 1, 0)/\sqrt{2}$ $s_2 < -1/\sqrt{2} \rightarrow s = (1, 0, -1, 0)/\sqrt{2}$
$\theta_n > 180° \rightarrow \theta_n = 360° - \theta_n$ $\theta_n < 0° \rightarrow \theta_n = -\theta_n$	$n_2 < 0 \rightarrow n_2 = -n_2$
$\theta_m < 0°$ (right forearm) $\theta_m > 0°$ (left forearm) $\rightarrow \theta_m = 0°$	$m_2 < 0$ (right forearm) $m_2 > 0$ (left forearm) $\rightarrow m = (1, 0, 0, 0)$

5.4 Simulation Studies

To investigate the performance of the new algorithm presented in Section 5.3, numerical simulations have been conducted. For ease of comparison, the angles of rotation corresponding to the flexion/ extension, θ_t, and medial/ lateral rotation, θ_s, of the upperarm and angles of rotation corresponding to the flexion/ extension, θ_{n-}, and pronation/ supination, θ_m, of the forearm are compared. A Gaussian white noise of zero mean and standard deviation of 0.03 (as estimated from actual accelerometer signal) is simulated to corrupt the accelerometer output in (5.7) and (5.39). The sampling rate of the accelerometer is assumed to be 10Hz.

5.4.1 Singularity Resolution

Upperarm

A simulation of a possible combination of flexion/extension and medial/lateral motion of the upperarm over the normal range of motion is performed. Fig. 5.2a shows the true and estimated angles of flexion/extension, θ_t, of the upperarm while Fig. 5.2b shows the true and estimated angles of medial/lateral rotation, θ_s. The corresponding arm positions at certain data points are also shown in Fig. 5.2c. The left upperarm is simulated to perform first a flexion motion from $\theta_t = 0^\circ$ to $\theta_t = 90^\circ$, followed by a extension to $\theta_t = -150^\circ$ and finally a flexion movement back to $\theta = 0^\circ$. At the same time, the upperarm first performs a medial rotation from $\theta_s = 0^\circ$ to $\theta_s = -90^\circ$, followed by a lateral rotation to $\theta_s = 90^\circ$ and then a medial rotation to $\theta_s = -90^\circ$. The upperarm is finally rotated laterally back to $\theta_s = 0^\circ$.

The angle of flexion/ extension, θ_t, is shown in the Fig. 5.2(a) and it can be observed that the estimated angle follows closely the true angle with a mean error of -0.0690° and standard deviation of 6.5598°. For the medial/lateral rotation

motion shown in the Fig. 5.2(b), it can be observed that when no singularity resolution is performed, the value of the estimated angle, θ_s, follows the true angle closely except for a tendency to drift away when the flexion/extension angle is 90° at the 15^{th} data sample and −90° at the 42^{th} and 67^{th} data sample. A mean error of −0.3084° and standard deviation of 9.5338° for the value of θ_s is obtained in this case. By "locking" in the value of the quaternion s when $\Delta_t < 0.05$, the value of the estimated θ_s are smoothen at the singularity points resulting in a mean error of −1.1420° and a much improved standard deviation of 7.4642°. The accuracy of the estimated value of θ_t with singularity resolution is also slightly improved with a mean error of −0.0201° and standard deviation of 6.4244°. The result of this numerical simulation for the upperarm validates the use of the singularity resolution strategy in transient singularity states for the upperarm.

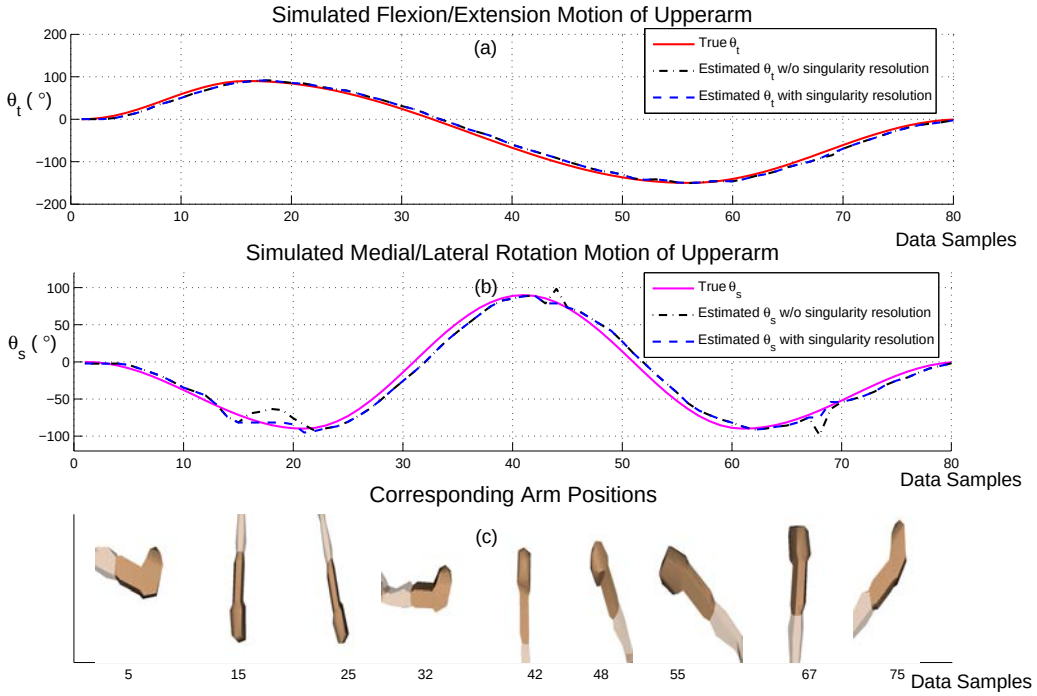

Figure 5.2. Simulated combination of flexion/ extension and medial/ lateral rotation of upperarm showing the effects of singularity resolution

Forearm

Next, a simulation of a possible combination of flexion/extension and pronation/supination motion of the forearm with a corresponding movement of the upperarm was carried out. The angle of flexion/extension , θ_t, and angle of medial/lateral rotation, θ_s, of the upperarm are shown in Fig. 5.3a. The values of the components of the vector $\mathbf{v}$ and the value of γ are also shown in Fig. 5.3b and 5.3c. The simulated and estimated angle of flexion/extension, θ_{n-}, and angle of pronation of the forearm are shown in Fig. 5.3d and 5.3e respectively. The corresponding arm positions are shown in Fig. 5.3f. In this simulation, the upperarm first performs an extension from the horizontal position to $\theta_t = -150°$ at the 60^{th} data sample. At the same time, the forearm performs a flexion from $\theta_{n-} = 0°$ to $145°$ and back to $0°$ while performing a pronation/supination from $\theta_m = -5°$ to -160° and back. Following that, the upperarm then flexes from $\theta_t = -150°$ back to the horizontal position at the 100^{th} data sample while performing a medial rotation to $\theta_s = -90°$, tilting the plane of motion for the forearm to horizontal. During this period of time, the forearm performs a flexion to $\theta_{n-} = 45°$ at the 80^{th} data sample. The forearm then remains in that flexion position while it performs a pronation/supination to $\theta_m = -90°$ and back at the 120^{th} data sample. From the 100^{th} to 120^{th} data sample, the upperarm performs an extension to $60°$ below the horizontal and lateral rotation to $45°$, tilting the plane of motion of the forearm to $45°$ about the vertical. The forearm then performs an extension to $\theta_{n-} = 0°$ and flexion to $\theta_{n-} = 145°$ and a pronation/supination to $\theta_m = -160°$ along this tilted plane.

It can be observed that the estimated value of θ_{n-} follows the true value closely except when the values of v_1 and v_3 is close to zero at about the 100^{th} sample. At this singular state, the upperarm is medially rotated and any flexion/extension of the forearm is a rotation about the vertical axis. The estimated angle of flexion/extension, θ_{n-}, diverges away from the true value giving a mean error of

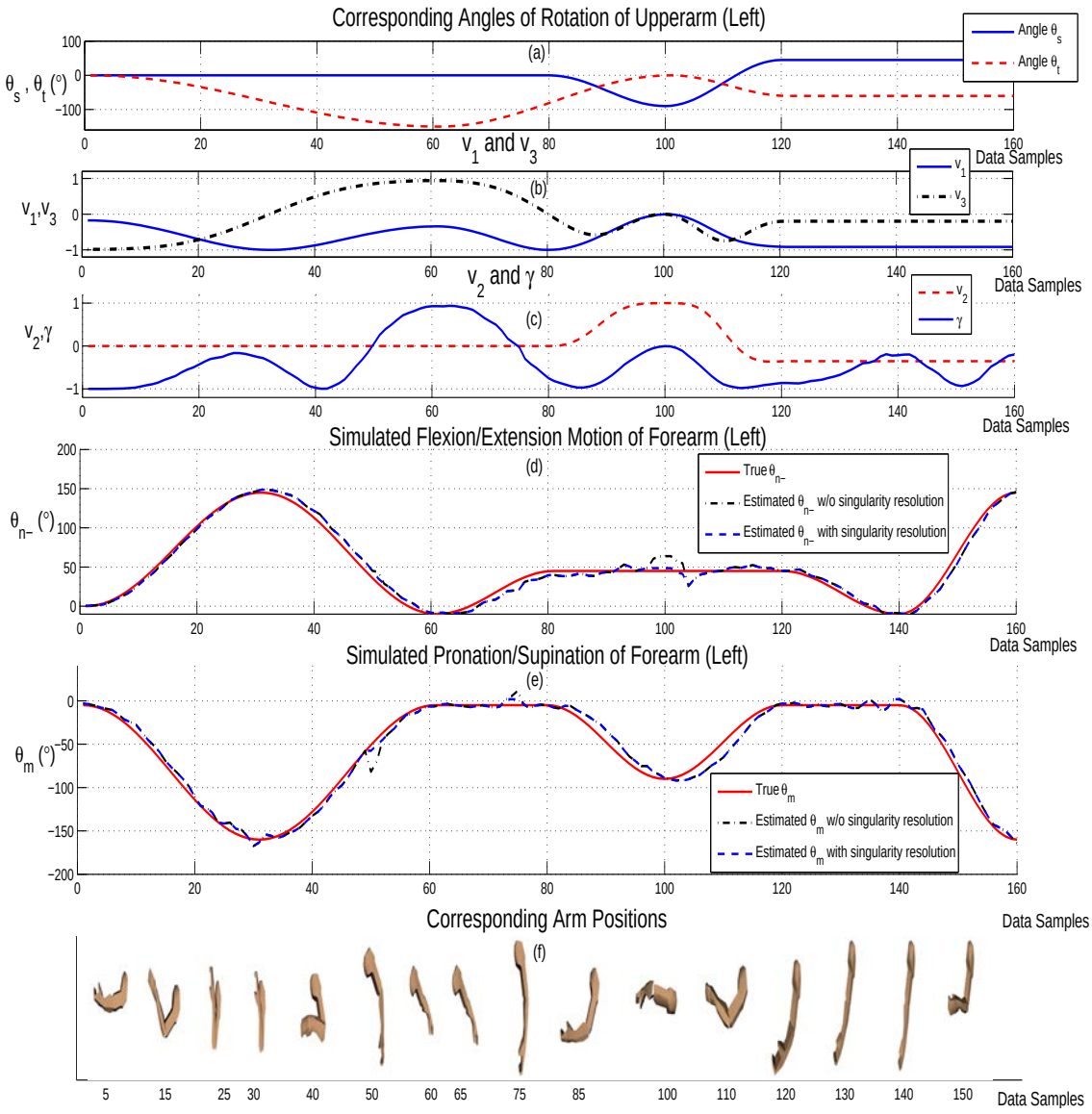

Figure 5.3. Simulated combination of flexion/ extension and pronation/ supination motion of forearm showing the effects of singularity resolution

0.4119° and standard deviation of 6.6283°. Applying the strategy for singularity resolution by letting $n_{k+1} = n_k$ when $v_1 < 0.05$ and $v_3 < 0.05$, the divergence is arrested and the estimation improves with a mean error of -0.1746° and standard deviation of 5.7959°. For pronation/supination movements, it can be observed that the estimated θ_m tend to deviate from the true values when both the values of v_2 and γ are close to zero at the 50^{th} and 75^{th} data sample. Without singularity resolution, the mean error is 0.6815° and the standard deviation is 7.4781°. With singularity resolution, letting $m_{k+1} = m_k$ when $v_2 < 0.05$ and $\gamma < 0.08$, the divergence is again arrested at the singular states of θ_m resulting in a mean error of 0.8582° and improved standard deviation of 6.6448°.

From the 120^{th} data sample onwards, the upperarm is simulated to flex at $\theta_t = -60°$ and laterally rotated to $\theta_s = 45$. This results in a tilting of the plane of motion from the vertical. The forearm is then simulated to perform a series of flexion/extension and pronation/supination along this tilted plane. It is observed that the factorized quaternion approach is able to estimate closely the true values of θ_{n-} and θ_m even when the plane of motion is tilted.

5.4.2 Ambiguity Resolution

Next, the performance of the factorized quaternion approach in the resolution of ambiguity of solutions by adopting the strategy as described in Section 5.3.3 was investigated. In this simulation, the plane of motion is tilted 45° to the gravity axis when the angle of upperarm flexion/extension is -45° and angle of medial/lateral rotation is -90°. Fig. 5.4 shows a simulated motion of the left forearm depicting a flexion/extension from 0° to 150° and back to 0° simultaneously with a pronation/supination angle of 0°. It is observed that the estimated angles of rotation are different from the true angles of rotation. Specifically, the angle of flexion/extension, θ_{n-}, is "flipped". The corresponding estimated arm positions depicted in Fig. 5.4c are also anatomically impossible to achieve. However, the

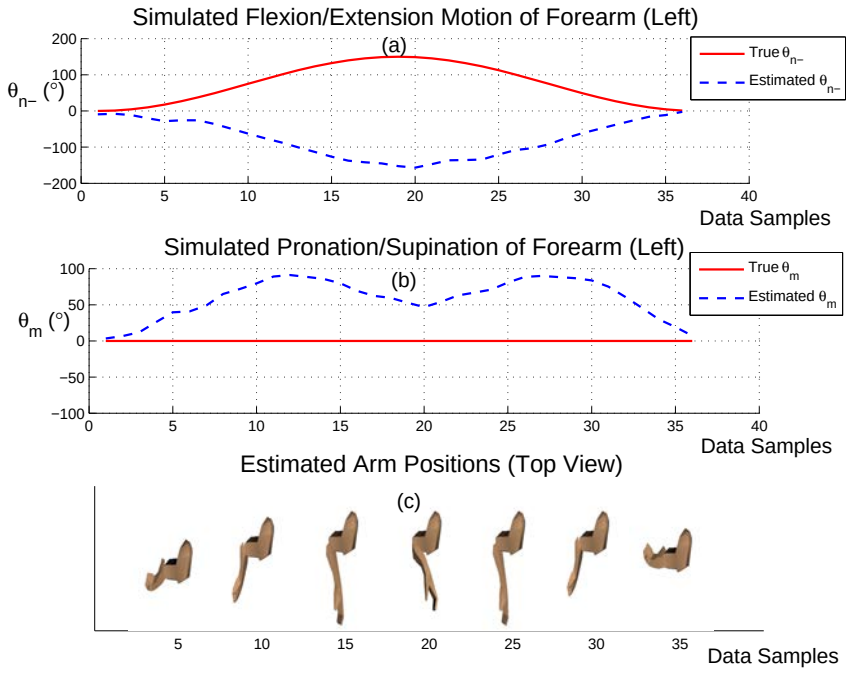

Figure 5.4. Simulated forearm movement showing convergence of algorithm to the other solution in a tilted plane (45° with respect to vertical)

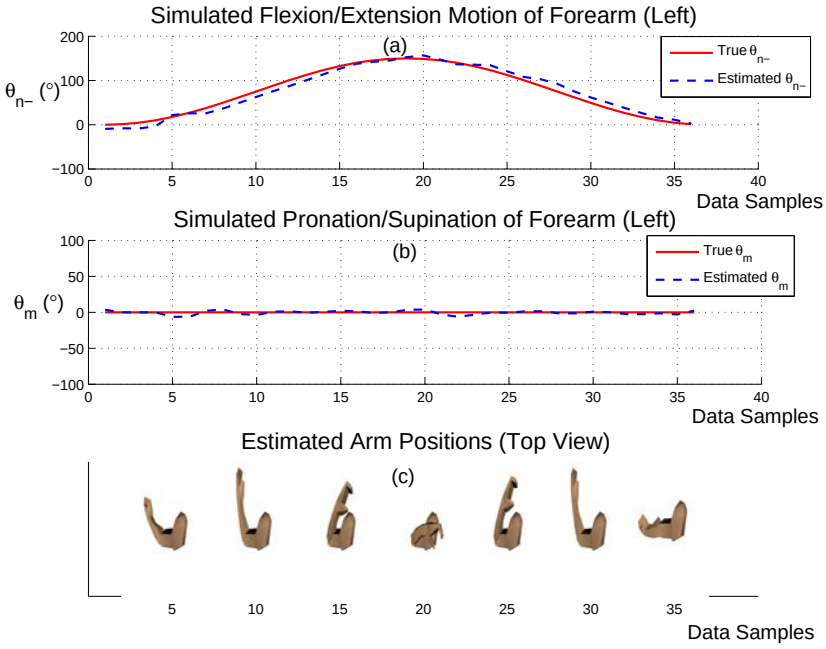

Figure 5.5. Simulated forearm movement showing convergence of algorithm to the desired solution with ambiguity resolution.

estimated quaternion solution when substituted into (5.36) will give accelerometer readings that are close to the actual accelerometer readings. The algorithm implemented in this case has converged to the other solution instead of the true value.

If the angle θ_n is inverted as mentioned, the algorithm converges to the correct solution instead as shown in Fig 5.5. This example illustrates the usefulness of the proposed approach in the resolution of ambiguity.

5.4.3 Second Order Correction

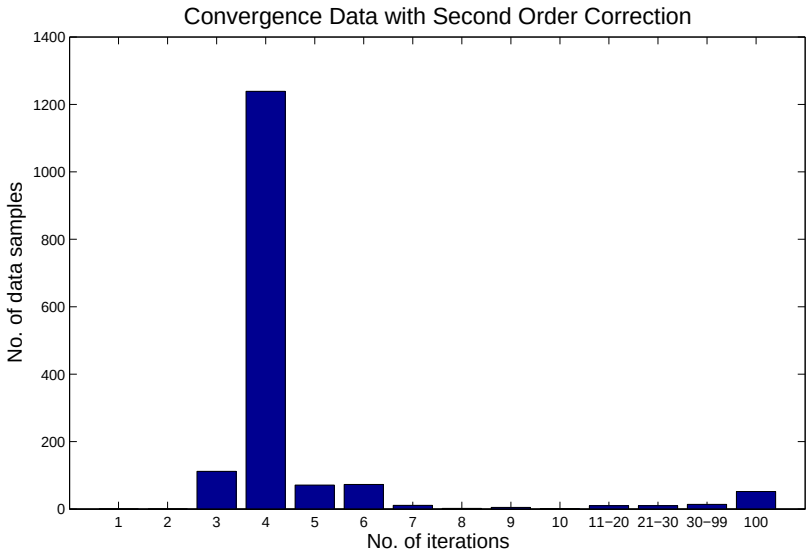

Figure 5.6. Convergence of forearm simulation data with second order correction

In this section, the convergence rate of the Newton's iterations with second order correction discussed in Section 5.3.1 is evaluated. Fig. 5.6 and 5.7 show the convergence rate for the forearm movement simulation data in Section 5.4.1 with and without second order correction.

In this simulation, the maximum number of iterations is capped at 100. The total number of data samples considered is 1600. For each data sample, a new set of random noise is generated for the statistical study. With second order correction, most of the data samples converge with four iterations. In addition,

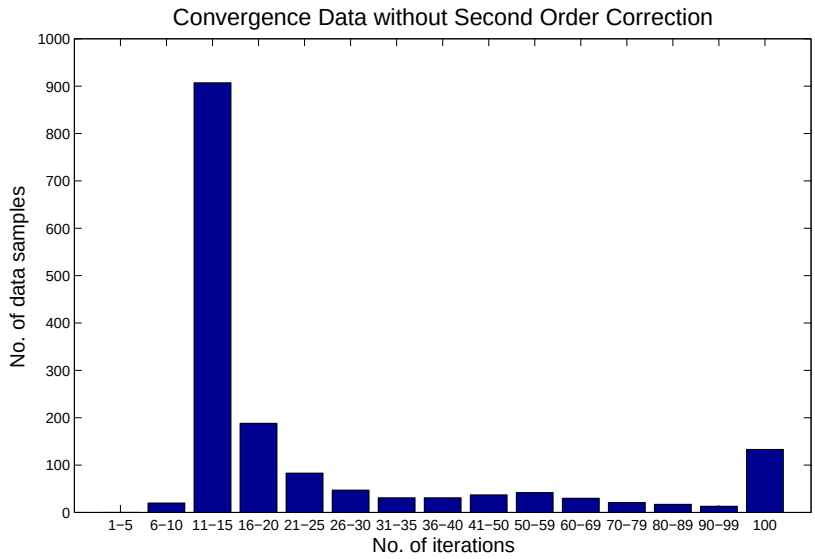

Figure 5.7. Convergence of forearm simulation data without second order correction

95% of the data samples converge within 10 iterations. Without second order correction, more than half of the data samples require 11-15 iterations. Only 82% of the data samples converge within 40 iterations.

In conclusion, the convergence rate is much faster with the second order correction. The maximum number of iterations required to prevent infinite loops during implementation can also be reduced to ten with second order correction.

5.4.4 Computational Requirements

To obtain an estimation of the efficiency of the optimization process using Algorithm 5.1 and 5.2, the time required to compute 1600 data samples was determined using MATLAB on a PC with an Intel Core i5-750 (2.6GHz, 8M L3 cache, 4 cores, 4 threads) and 4GB (2×2GB) of DDR3 1333MHz SDRAM. Table 5.4 shows the mean computational time for each data sample.

As can be seen from Table 5.4, the mean processing obtained times for Algorithm 5.1 and 5.2 were 8.2ms and 12.3ms respectively without implementing the second order correction. The maximum number of iterations used for optimization without the second order correction was set at 100 so that the convergence rate

TABLE 5.4
COMPUTATIONAL TIME FOR OPTIMIZATION USING ALGORITHM 5.1 & 5.2

	Mean Processing Time	
	with second order correction (max no. iteration = 10)	w/o second order correction (max no. iteration = 100)
Algorithm 5.1 (upperarm)	2.2ms	8.2ms
Algorithm 5.2 (forearm)	2.6ms	12.3ms

obtained was at least 90%). By implementing the second order correction, much lower mean processing times were obtained for Algorithm 5.1 and 5.2 at 2.3ms and 2.6ms respectively while lowering the maximum number of iterations to 10 to achieve a similar convergence rate.

5.5 Experimental Evaluation

To validate the performance of the factorized quaternion approach, various experiments have also been conducted using the developed wearable wireless sensor network platform described in Chapter 3. In this study, the tri-axial accelerometer, MMA7361L, from Freescale, is used in each sensor node. The raw signal of each accelerometer is filtered with a fourth order Butterworth filter with a cut-off frequency of 3.5Hz as in [27]. The scale factor matrix, $\mathbf{K_a}$, representing the sensitivity of the accelerometer, $\mathbf{R_a}$, the rotation matrix accounting for misalignment of the sensor coordinate frame with the body coordinate frame and cross-axis sensitivity effects and $\mathbf{b_a}$, the vector of sensor biases or zero-g offset, are estimated in a calibration process outlined in [90]. The acceleration vector, $\mathbf{a}$, is then determined using the accelerometer reading, $\mathbf{u_a}$, by the following linear model:

$$\mathbf{a} = {\mathbf{R_a}}^T {\mathbf{K_a}}^{-1} (\mathbf{u_a} - \mathbf{b_a}) \tag{5.52}$$

Fig. 5.8 shows the attachment of the sensor nodes onto the upperarm and forearm. Ideally, the sensor nodes should be mounted close to the center of rotation to minimize the effects of angular velocity and acceleration. In our experiments, the sensor node on the upperarm is mounted close to the elbow joint. This is because the muscle near the shoulder joint does not rotate with any medial/lateral rotation of the upperarm. The sensor node on the forearm is also mounted near the wrist in order to measure the pronation/supination motion of the forearm.

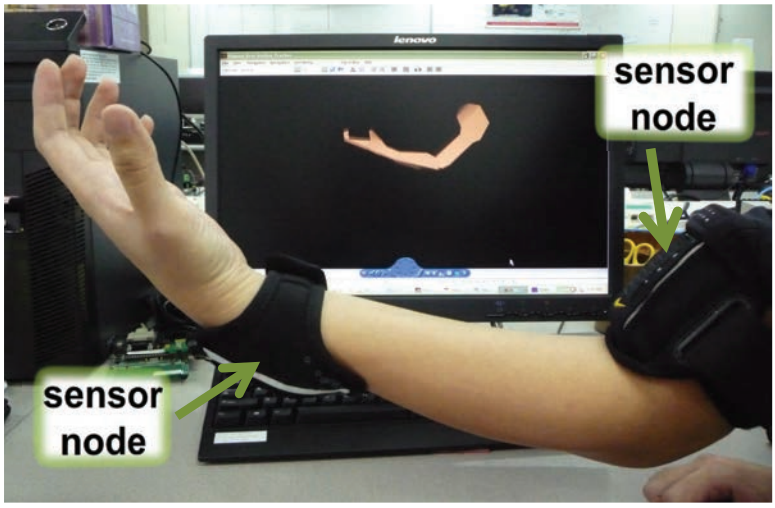

Figure 5.8. Attachment of a sensor node on the upperarm near the elbow joint and another sensor node on the forearm near the wrist

The output of the accelerometers are benchmarked with an industrial inertial measurement unit (IMU), MTx, from Xsens. The IMU has a three-axes accelerometer, gyroscope and magnetometer integrated with an embedded processor. It has a static accuracy of 0.5° for roll and pitch, 1.0° for yaw in homogenous magnetic environment and a dynamic accuracy of 2° rms. As shown in Fig. 5.9, the IMU is mounted on top of the sensor node during the experiments. This is to ensure that the IMU has the same reference coordinate frame as the sensor node and is at the same distance away from the center of rotation (elbow or shoulder joint). In addition, the orientation of the IMU is estimated and is offset from the estimated orientation of the sensor node before the start of each experiment.

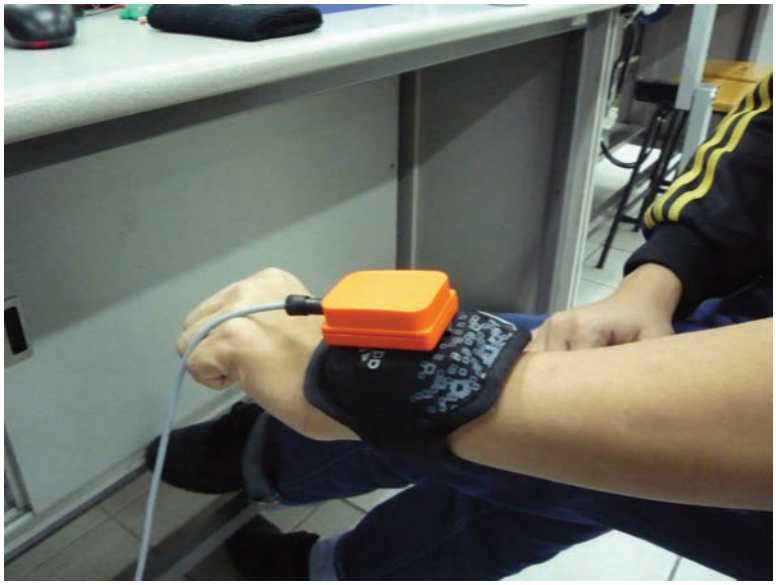

Figure 5.9. Attachment of IMU on top of sensor node (inside wrist wallet)

5.5.1 Upperarm Experiment

To evaluate the algorithm in determining the orientation of the upperarm, an experiment was first performed requiring the subject to move his left upperarm in the sagittal plane in a series of motions designed to cover the normal range of motion. Initially, the subject's arm is held at the horizontal position. The arm is then flexed upwards vertically until no further flexion can be performed. Following that, the arm is extended all the way until it is beside the subject's body. Hyperextension is performed from this point onwards and continued until the limit. The arm is then flexed back to the horizontal position and a medial/lateral rotation is performed in this position. The medial and lateral rotations are repeated when the arm flexed above the horizontal and again when it is extended below the horizontal.

Fig. 5.10a shows the angle of flexion/extension, θ_t, obtained from the experimental system together with the pitch angle, θ, obtained from IMU. Fig. 5.10b shows the corresponding angle of lateral/medial rotation, θ_s obtained using the accelerometer and the IMU roll angle, ϕ. The yaw angle, ψ, from the IMU is also shown for reference. Fig. 5.10c shows the plot of differences $(\theta_t - \theta)$ and $(\theta_s - \phi)$.

The estimated arm positions using the accelerometer at certain times are also shown in Fig. 5.10d. It can be observed that θ_t follows closely the pitch angle, θ. Moreover, θ_s follows the roll angle, ϕ, closely except at 6s when the value of ϕ start to diverge. When the upperarm performs an extension beyond $-90°$ at 6.5s, the values of both θ_t and θ are observed to increase instead of decreasing beyond $-90°$. At the same time, the yaw increases sharply while θ_s and roll decreases sharply by similar amount. Since the accelerometer is unable to determine the yaw angle as the IMU, the value of θ_s has appeared to diverge at this point.

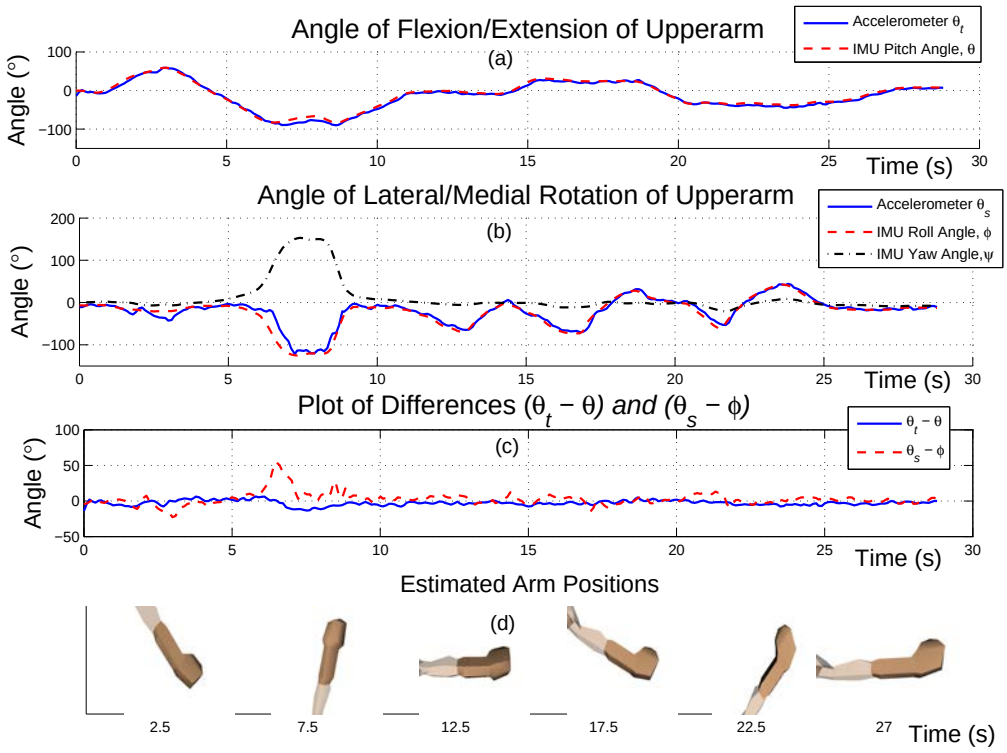

Figure 5.10. Angle of Flexion/ Extension (θ_t) and Lateral/ Medial rotation (θ_s) of upperarm without singularity resolution with IMU Pitch (θ), Roll (ϕ) and Yaw (ψ) angles

Using the strategy for singularity resolution as discussed in Section 5.3.3, the value of θ_t at 6.5s beyond $-90°$ can be obtained together with a better estimate of θ_s that does not diverge as shown in Fig. 5.11. The Euler angles of yaw, pitch and roll from the IMU is required to be converted to follow the range of values $-180° < \theta < 180°$, $-180° < \phi < 180°$ and $-90° < \psi \leq 90°$, while minimizing

ψ since the motion is performed in a vertical plane. Fig. 5.11c shows the plot of differences $(\theta_t - \theta)$ and $(\theta_s - \phi)$ with and without singularity resolution. The estimated arm positions using the accelerometer at certain times are also shown in Fig. 5.11d. It is observed that the increases in differences $(\theta_t - \theta)$ and $(\theta_s - \phi)$ are arrested at the 6.5s with singularity resolution. With singularity resolution, the mean difference between θ_t and θ is $-2.12°$ and the standard deviation is $4.78°$. The mean difference between θ_s and ϕ is $-3.68°$ and the standard deviation is $9.64°$. The higher mean difference and standard deviation are due to the movement deviating from the sagittal plane at the time from 2 to 4 s and the inability of the accelerometer to capture the true value of θ_s at the singularity point of θ_t near $-90°$ from 6 to 9 s.

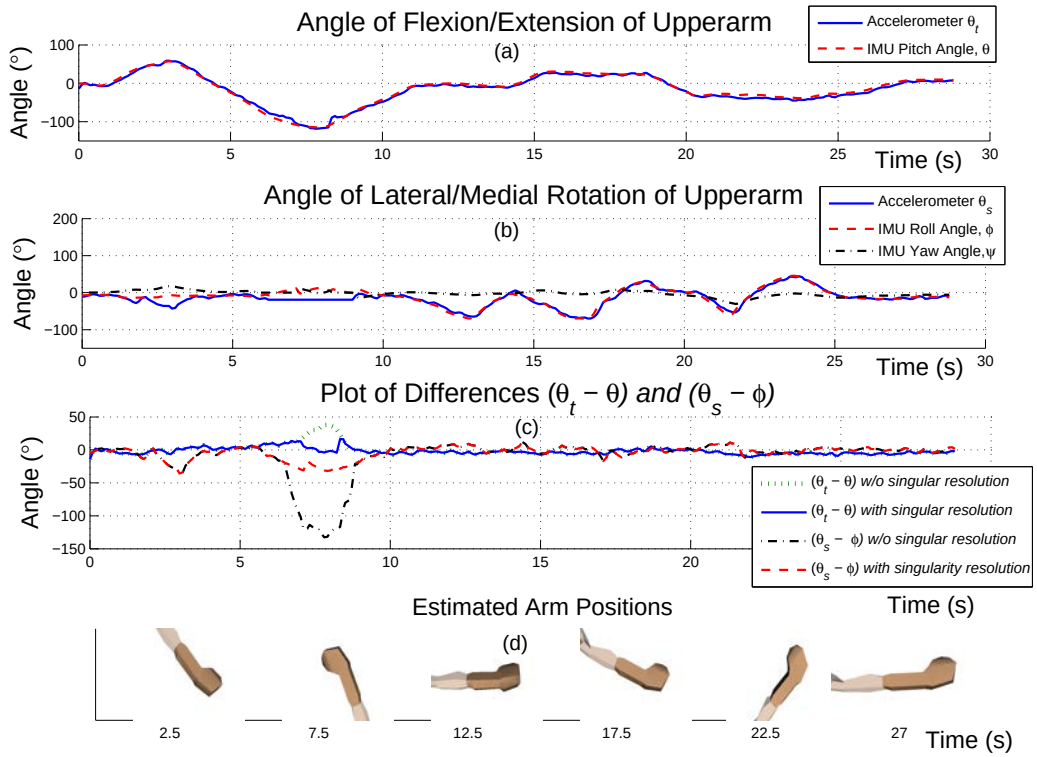

Figure 5.11. Angle of Flexion/ Extension (θ_t) and Lateral/ Medial rotation (θ_s) of upperarm with singularity resolution with IMU Pitch (θ), Roll (ϕ) and Yaw (ψ) angles

5.5.2 Forearm Experiment

To evaluate the performance of the algorithm in determining the orientation of the forearm, the subject is asked to perform a series of flexion/extension and pronation/supination motion of the left forearm together with flexion/extension and medial/lateral rotation of the upperarm. A few set of the arm positions corresponding to the time scale is illustrated in Fig. 5.12g. These motions are designed to cover the normal range of motion for both the upperarm and forearm while keeping the upperarm in the sagittal plane. The corresponding θ_t, and θ_s of the upperarm are shown in Fig. 5.12a while the corresponding values of $\mathbf{v}$ and γ are shown in Fig. 5.12b–c. Fig. 5.12d–e shows the angle of flexion/extension, θ_{n-}, and the corresponding angle of pronation/supination θ_m obtained from the accelerometer attached to the forearm. The results of the yaw, pitch and roll angles obtained from the IMU attached to the forearm (offset by the Euler angles of the upperarm's orientation) are also plotted for comparison. Fig. 5.12f shows the plot of differences ($\theta_{n-}-$pitch angle) and (θ_m- roll angle) with and without singularity resolution.

The results show that θ_{n-} follows closely to the IMU pitch angle except when the values of v_1 and v_3 are close to zero at 18.5s resulting in a near singularity state. Without singularity resolution, the estimate of θ_{n-} diverges resulting in a mean difference of $-3.69°$ and standard deviation of $17.31°$. This divergence is overcome with singularity resolution, resulting in an improved mean difference of $-3.08°$ and a standard deviation of $12.34°$. Similarly, θ_m follows closely to roll angle except at 13s and 27s when the values of v_2 and γ are close to zero. Without singularity resolution, the estimate of θ_m at this state of near singularity diverges resulting in a mean difference of $-3.16°$ and standard deviation of $17.50°$. It can also be observed that the estimate of θ_{n-} is also affected with a slight divergence at 13s. With singularity resolution, the estimate of θ_m improves to a mean difference

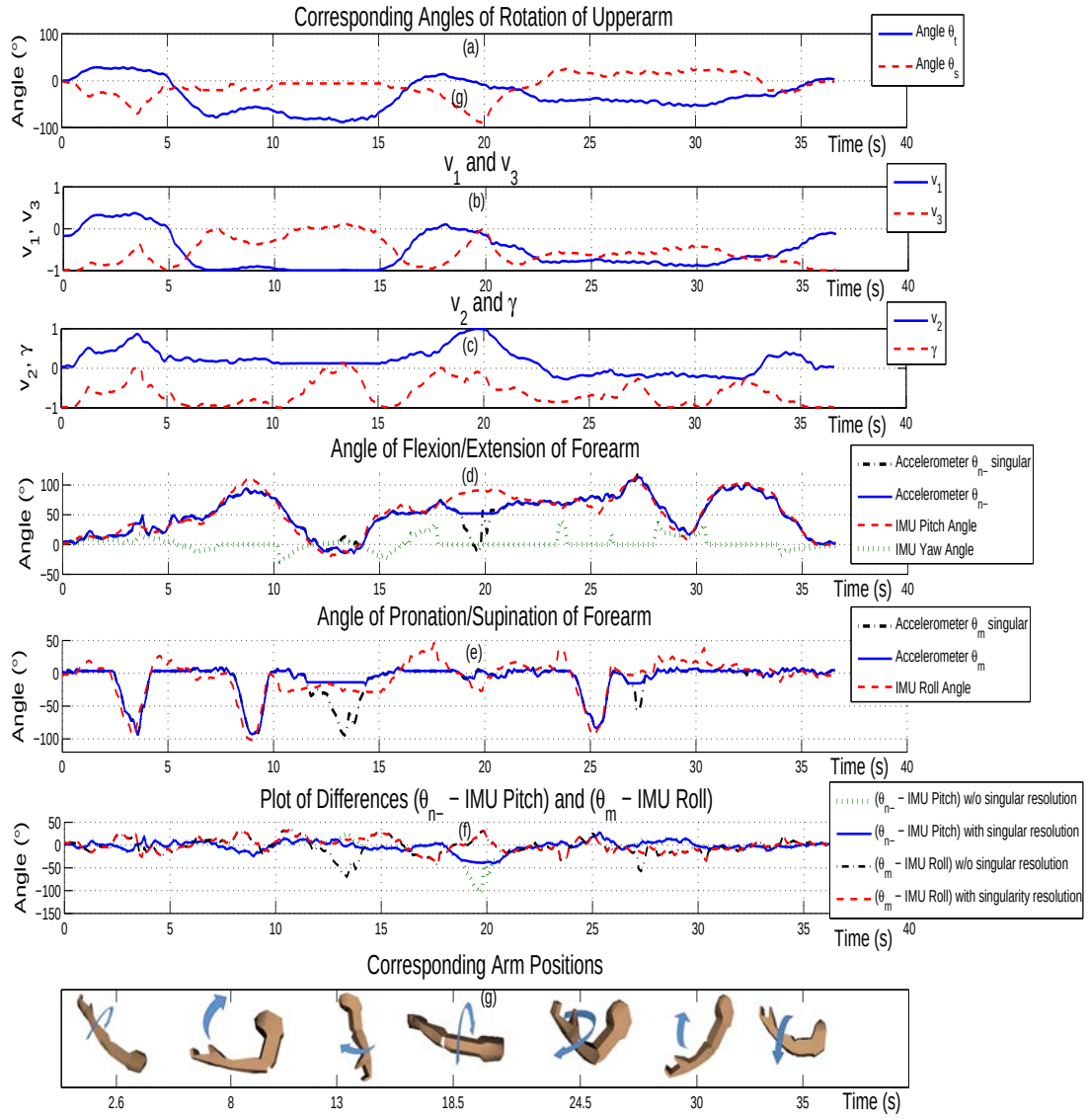

Figure 5.12. Angle of Flexion/ Extension (θ_{n-}) and Pronation/ Supination (θ_m) of Forearm with Pitch, Roll and Yaw angles from IMU

of $-0.22°$ and standard deviation of $14.38°$.

From the 22s, lateral rotation of the upperarm to about $\theta_s = 20°$ causes the plane of motion of the forearm to be tilted from the vertical. It is observed that the estimate of θ_{n-} and θ_m follows closely the corresponding values of pitch and roll angles obtained from the IMU even when the plane of motion is non-vertical. The value of the yaw angle obtained from the IMU is also shown in 5.12d. It can be seen that there is not much change in heading except when the forearm undergoes flexion/extension in a slanted plane from 28 to 31s .

5.5.3 Ambiguity Resolution

Fig. 5.13a-b shows θ_{n-} and θ_m of the forearm performing a flexion/extension motion with the upperarm held vertically beside the body. The pitch and roll angles obtained from the IMU are also shown. The estimated arm positions using the accelerometer without and with ambiguity resolution are shown in Fig. 5.13c-d. The pitch and roll angles obtained from the IMU are also shown. As each accelerometer reading can correspond to two different orientations, Fig. 5.13 shows that it is possible for the estimates of θ_{n-} and θ_m (shown by the black dash-dot lines) to converge to the undesired solution. Using the constraints in Section 5.2.3 and strategy as described in Section 5.3.3, the solution space and ambiguity of solutions are reduced. The algorithm will then converge to the desired solution following closely to the angles determined using the IMU.

5.5.4 Power Consumption and Cost

Table 5.5 shows the estimated power consumption and cost of some of the common triaxial accelerometers, gyroscopes and magnetometers in the market today. It is observed that the power consumption of a gyroscope is 12–30 times of an accelerometer while the power consumption of a typical magnetometer is twice that of the accelerometer. Moreover, the gyroscope is 7–10 times more expensive

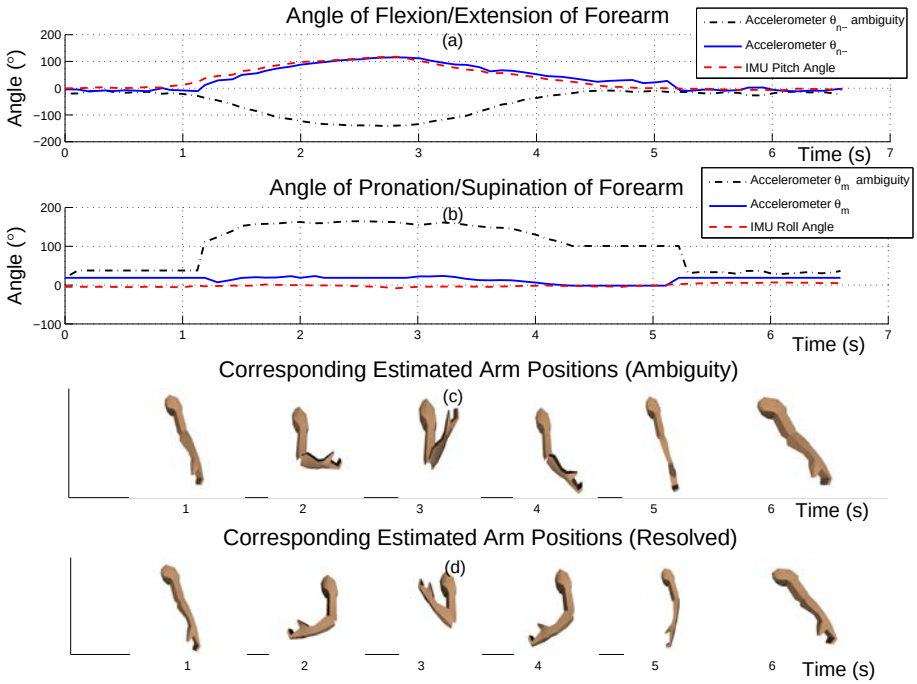

Figure 5.13. Angle of Flexion/ Extension (θ_{n-}) and Pronation/ Supination (θ_m) of Forearm showing ambiguity resolution with Pitch and Roll angles from IMU

TABLE 5.5
ESTIMATED POWER CONSUMPTION AND COST OF COMMON TRI-AXIAL ACCELEROMETERS, GYROSCOPES AND MAGNETOMETERS

Tri-axial Sensor	**Part No.**	**Power Consumption**	**Estimated Cost (USD)**
Accelerometer	MMA7361L	1.32mW	$1.00
	LIS352AX	0.99mW	$2.41
	ADXL327	1.05mW	$3.03
Gyroscope	ITG-3200	16.25mW	$10.00
	L3G4200D	18.3mW	$7.52
	ADXRS450	30mW	$53.97
Magnetometer	HMC5843 (AMR)	2.25mW	$3.25
	MAG3110 (AMR)	2.16mW	$1.47
	AK8973N/B/S (Hall Effect)	2.49mW	$3.03

than the accelerometer. The magnetometer on the other hand is 1.5–3 times more expensive.

5.5.5 Real Time Screenshots

Fig. 5.14 shows the display on the computer monitor in real time with the sensors mounted on the arm. The results show that the system has fairly good correlation between the actual arm movements and re-constructed movements on the computer screen. The system works well even if the person is moving away from the network coordinator at a distance of 20m in the laboratory environment.

5.5.6 Discussion

The quaternion rotation operator is singularity free and can relate any two independent coordinate frames. One reason for the occurrence of singularity is that the factorized quaternion approach mimics the conventional Euler sequence of yaw, pitch and roll (yaw is fixed in our case) which has a singularity at a pitch of $\pm 90°$. This singularity coincides with the singularity arising from the use of the accelerometer in determining the orientation of the upperarm when it is vertical, with any subsequent medial/lateral rotation being a rotation about the vertical axis. The singularities arising from the use of the accelerometer in determining the forearm's orientation on the other hand follows from a combination of rotation of the upperarm and forearm resulting in either the subsequent flexion/extension or pronation/supination of the forearm to be a rotation about the vertical axis. The singularities arising from the use of the accelerometers are unavoidable and therefore explains the need for an implementation of a strategy for singularity resolution in the algorithm for orientation determination. Factorization of the quaternion into its principal axes quaternions allows the detection of the singularities. This in turn allows the implementation of a strategy to "lock" rotation about the vertical axis at the state of singularity to prevent divergence of solution.

Figure 5.14. Real time data display showing arm movements

This strategy is based on the assumption that the motion of the arm is continuous and that the state is transient. The result is a smooth tracking process using only the accelerometer for the motion of the arm.

In addition, by factorizing the quaternion, the angle of flexion/extension and medial/lateral rotation (or pronation/supination) of the upperarm and forearm can be determined directly. As such, measurements can be made to conform to the range of motion subject to anatomical constraints and hence reduce any ambiguity in the estimated orientation.

5.6 Summary

In this chapter, a factorized quaternion approach has been proposed for determining the orientation of the articulated human arm in a single plane. Numerical simulation studies has been conducted to validate the feasibility of the proposed approach. The implementation of a second order correction was also shown to be able to speed up the convergence rate of the orientation estimates and the computational time of the optimization algorithms. The developed wearable wireless sensor network system was then used to evaluate experimentally the performance of the proposed factorized quaternion approach. Experiments performed demonstrated that the proposed approach was able to determine the orientation of the upperarm along a vertical plane and the forearm along a tilted plane from the vertical by making use of information on the upperarm. Experimental results also showed that the factorized quaternion approach had a comparable accuracy when benchmarked with a commercial multiple-sensor IMU. In addition, the proposed factorized quaternion approach is able to resolve transient singularities arising from the use of the tri-axial accelerometers. The ambiguity of solutions can also be reduced by implementing constraints on the range of arm motion and eliminating solutions that are anatomically impossible. The typical power consumption

of the sensor node equipped with triaxial accelerometer is 89mW as compared to 350mW for an IMU. This approach is therefore superior to the single angle-axis quaternion approach presented in Section 4.6.

The main limitation of this approach is that the orientation measurement is still confined to a single plane. For applications in which the orientation measurement in the 3D plane is required, additional sensors are required. In the next chapter, a new algorithm for orientation measurement using an additional tri-axial magnetometer and gyroscope sensor will be presented.

CHAPTER 6

Sensor Fusion Algorithm for Determination of Arm Orientation

6.1 Introduction

In Chapter 5, the factorized quaternion approach has been proposed using an accelerometer to measure the arm orientation along a single plane. As an accelerometer only approach, the main limitation lies in the determination of rotation about the vertical axis. As mentioned in Chapter 2, a magnetometer can be added to determine heading information while a gyroscope can be used to account for dynamic changes in orientation. In this chapter, a novel algorithm is proposed to fuse information from these sensors to determine the orientation of an arm limb.

The orientation of a noninertial coordinate frame relative to an inertial reference frame is often described using a sequence of consecutive rotations through three body-referenced Euler angles [91]. Since there are twelve possible ways to describe three independent Euler angles rotations(where no two successive rotations may be about the same axis), the temporal order of these rotations needs to be specified. For instance, in the aerospace rotation sequence, the Euler sequence of yaw $\rightarrow$ pitch $\rightarrow$ roll is used. Inherent in every Euler angle sequence though is at least one singularity [71]. An alternative is to use the Euler-Rodrigues parameter or quaternion of finite rotation which is inherently singularity free and can be used to relate any two independent coordinate frames. However, the physical interpretation of the quaternion is much less intuitive than that associated with

the Euler angles [83].

In contrast to these approaches, a new algorithm based on fixed elevation and heading angles in the determination of orientation is presented. The elevation angle is defined as the angle of the sensor's axes with respect to the horizontal plane. The heading angle on the other hand is defined as the angle between the projection of the heading axes on the horizontal plane and the magnetic north. Compared to the Euler angles, the fixed elevation and heading angles are independent on the temporal order of rotations. Given an object in a certain orientation, the fixed elevation and heading angles are also visually intuitive as compared to the Euler angles or quaternions. A novel method is proposed to avoid singularities that may arise, thereby allowing for tracking through all possible orientations.

The magnetometer output is known to be affected by local magnetic interferences in the environment caused by nearby ferromagnetic materials and electrical appliances. One approach is to decouple the accelerometer and magnetometer readings and use the magnetometer only for the determination of heading. As such, interfering magnetic fields affect only the accuracy of heading measurements. The TRIAD algorithm [45] based on solving the Wabha problem [42] can be used to eliminate the contribution of the magnetometer reading relative to the vertical axis by using the gravitational and magnetic field vectors. However information on the earth's magnetic inclination is often lost when using the magnetic field vector as the second reference vector. Other methods to determine the yaw angle using only the magnetometer include the azimuth detector proposed by Zhu et al. [43] based on rotation matrices using Euler angles and a closed-form algorithm based on factorized quaternions proposed by Yun et. al [44]. Applying a similar strategy, the magnetometer output in the proposed algorithm is formulated to determine only the heading angle while the accelerometer readings are used to determine the elevation angles.

In using the accelerometer for orientation determination, one of the challenges

is the estimation of the gravity vector in the presence of external acceleration due to motion of the body. One approach is to use the norm of the accelerometer reading to detect the presence of external acceleration and vary the measurement noise accordingly [37, 63]. In [64], Suh proposed an indirect Kalman filter based on quaternions which uses the residual of the accelerometer measurement update instead for external acceleration estimation. These approaches for accounting the external acceleration are however heuristic and are dependent on the threshold for detection. In this algorithm, the kinematics of the rotations are considered in order to estimate the external acceleration arising from the rotations of the arm limbs using the gyroscope. This external acceleration is then offset from the accelerometer output to obtain a more accurate estimate of the gravitational acceleration vector.

In this chapter, the derivation of the proposed sensor fusion is first presented. This is then followed by the presentation of the results of experiments conducted to test the proposed algorithm.

6.2 Determination of Orientation of Body Segment

Fig. 6.1 shows the fixed inertial coordinate frame and the sensor coordinate frame. In this figure, the Z-axis of the fixed inertial reference frame is defined as pointing vertically upwards. The X and Y-axes of the fixed inertial reference frame are defined as lying in the horizontal plane with the X-axis pointing in the direction of the magnetic north. The direction of Y-axis is such that X, Y and Z-axes form a right handed coordinate system.

6.2.1 Compensation of External Acceleration

Define the gravity vector, $\mathbf{g}$, and the earth magnetic north vector, $\mathbf{h}$, by:

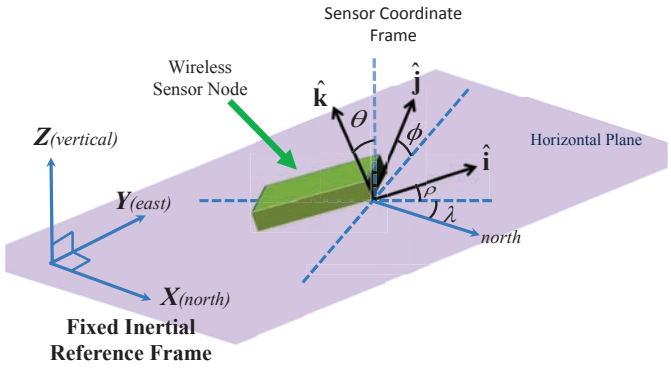

Figure 6.1. Fixed inertial reference frame and sensor coordinate frame showing the elevation angles and heading angles

$$\mathbf{g} = \begin{pmatrix} 0 \\ 0 \\ g \end{pmatrix}, \quad \mathbf{h} = \begin{pmatrix} H\cos\alpha \\ 0 \\ -H\sin\alpha \end{pmatrix} \tag{6.1}$$

where g is the gravitational acceleration, α is the magnetic dip angle (angle in which the earth magnetic field makes with the surface) and H is the Earth's magnetic field strength. The accelerometer output $\mathbf{u}_a$, gyroscope output $\mathbf{u}_g$ and magnetometer output $\mathbf{u}_m$ can be modeled as

$$\mathbf{u}_a = \mathbf{R}\mathbf{g} + \mathbf{a}_e + \mathbf{b}_a + \mathbf{v}_a \tag{6.2}$$

$$\mathbf{u}_g = \boldsymbol{\omega} + \mathbf{b}_g + \mathbf{v}_g \tag{6.3}$$

$$\mathbf{u}_m = \mathbf{R}\mathbf{h} + \mathbf{b}_m + \mathbf{m}_d + \mathbf{v}_m \tag{6.4}$$

where $\mathbf{R}$ is the rotation matrix representing the orientation of the sensor node with respect to the inertial frame and $\boldsymbol{\omega}$ is the angular velocity. $\mathbf{b}_a$, $\mathbf{b}_g$ and $\mathbf{b}_m$ are the biases of the accelerometer, gyroscope and magnetometer respectively which can be estimated through calibration [47, 90, 92]. $\mathbf{v}_a$, $\mathbf{v}_g$ and $\mathbf{v}_m$ are the sensor

noises which are assumed to be zero mean white Gaussian noises. $\mathbf{m}_d$ is the non-deterministic magnetic disturbance to the magnetometer caused by ferromagnetic objects in the environment which move independently of the sensor node. This can be minimized by taking measurements away from ferromagnetic materials and strong electrical currents. The magnetic field, $\tilde{\mathbf{m}}$, at the sensor node is estimated as follows:

$$\tilde{\mathbf{m}}= \begin{pmatrix} m_x \\ m_y \\ m_z \end{pmatrix} = \mathbf{u}_m - \mathbf{b}_m \tag{6.5}$$

$\mathbf{a}_e$ is the external acceleration due to the arm limb which can be expressed as

$$\mathbf{a}_e = \mathbf{a}_o + \boldsymbol{\alpha} \times \mathbf{r} + \boldsymbol{\omega} \times (\boldsymbol{\omega} \times \mathbf{r}) \tag{6.6a}$$

$$\begin{aligned} &= \begin{pmatrix} a_x^o \\ a_y^o \\ a_z^o \end{pmatrix} + \begin{pmatrix} r_z\dot{\omega}_y - r_y\dot{\omega}_z \\ -r_z\dot{\omega}_x + r_x\dot{\omega}_z \\ r_y\dot{\omega}_x - r_x\dot{\omega}_y \end{pmatrix} \\ &\quad - \begin{pmatrix} r_x\left({w_y}^2 + {w_z}^2\right) \\ r_y\left({w_x}^2 + {w_z}^2\right) \\ r_z\left({w_x}^2 + {w_y}^2\right) \end{pmatrix} + \begin{pmatrix} r_y\omega_x\omega_y + r_z\omega_x\omega_z \\ r_x\omega_x\omega_y + r_z\omega_y\omega_z \\ r_x\omega_x\omega_z + r_y\omega_y\omega_z \end{pmatrix} \end{aligned} \tag{6.6b}$$

where $\boldsymbol{\alpha}$ is the angular velocity. Assuming that the joint corresponding to the center of rotation is stationary, the value of $\mathbf{a}_o$ is then close to zero. $\mathbf{r}$ is the vector of the position of the inertial measurement unit with respect to the joint. The component of the angular velocity, ω_x, ω_y and ω_z can be estimated from the gyroscope output as

$$\tilde{\omega} = \mathbf{u}_g - \mathbf{b}_g \tag{6.7}$$

while the components of the angular acceleration, $\dot{\omega}_x$, $\dot{\omega}_y$ and $\dot{\omega}_z$, can be estimated using the first order backward difference approximation as

$$\dot{\omega}\left[kT\right] = \frac{1}{T}\left\{\mathbf{u}_g\left[kT\right] - \mathbf{u}_g\left[\left(k-1\right)T\right]\right\} \tag{6.8}$$

where T is the sampling period. The influence of the external acceleration can then be offset from the accelerometer reading together with the bias, $\mathbf{b}_a$, obtained by calibration. If the sensor node is mounted on the wrist for the forearm and on the bicep for the upperarm, it can also be observed from (6.6) that the effect of the external acceleration is greatest for the flexion motion where the component of $\mathbf{r}$ is largest. Similarly, the effect of the external acceleration is smallest for a medial/lateral rotation motion where the component of $\mathbf{r}$ is smaller.

The acceleration vector in the sensor coordinates is then estimated using (6.2)

$$\tilde{\mathbf{a}} = \begin{pmatrix} a_x \\ a_y \\ a_z \end{pmatrix} = \left(\mathbf{u}_a - \mathbf{a}_e - \mathbf{b}_a\right) \tag{6.9}$$

6.2.2 Method of Fixed Elevation Angles

The rotation matrix, $\mathbf{R}$, in (6.2) and (6.4) is decomposed into three components, namely into

$$\mathbf{R} = {\mathbf{R}_o}^T \mathbf{R}_v \mathbf{R}_y \tag{6.10}$$

where $\mathbf{R}_v$ is the rotation matrix representing the elevation of the sensor node with respect to the horizontal plane, $\mathbf{R}_y$ represents the rotation of the sensor node with respect to the vertical axis and $\mathbf{R}_o$ is used for singularity resolution to be describe in Section 6.2.3. As shown in Fig. 6.1, the elevation angle ρ is defined as the angle of the $\hat{\imath}$-axis of the sensor node relative to the horizontal, elevation angle ϕ is defined as the angle of the $\hat{\jmath}$-axis relative to the horizontal and elevation angle θ is defined as the angle of the $\hat{k}$-axis relative to vertical. The heading angle, λ, is

the angle between the projection of the $\hat{i}$-axis onto the horizontal plane and the X-axis.

The values of the three angles can be determined as

$$\rho = \text{atan}\left(\frac{a_i}{\sqrt{{a_j}^2 + {a_k}^2}}\right) \tag{6.11}$$

$$\phi = \text{atan2}\left(a_j, sign\left(a_k\right)\sqrt{{a_i}^2 + {a_k}^2}\right) \tag{6.12}$$

$$\theta = \text{atan}\left(\frac{\sqrt{{a_i}^2 + {a_j}^2}}{a_k}\right) - H\left(a_k\right)180^\circ \tag{6.13}$$

where $H()$ is the Heaviside step function, atan is the 2-quadrant arctangent function and atan2(y_t,x_t) is the 4-quadrant arctangent function which computes the arctangent using both the signs of x_t and y_t. The range of values for the angles in this case is set as $-90^\circ < \rho < 90^\circ, -180^\circ < \phi \leq 180^\circ$ and $0^\circ \leq \theta \leq 180^\circ$ to avoid any ambiguity. θ is related to ρ and ϕ by the relationship:

$$\tan\theta = sign\left(\cos\rho\cos\phi - \frac{1}{2}\right)\sqrt{\frac{\sin^2\rho + \sin^2\phi}{\cos\left(\rho+\phi\right)\cos\left(\rho-\phi\right)}} \tag{6.14}$$

Assuming first that the heading axis, $\hat{i}$ of the sensor node is pointing in the X-axis direction, i.e, the heading angle, λ is zero, the unit vector of the rotated $\hat{i}$-axis is given by

$$\hat{\mathbf{i}} = \begin{pmatrix} \hat{i}_1 \\ \hat{i}_2 \\ \hat{i}_3 \end{pmatrix} = \begin{pmatrix} \cos\rho \\ 0 \\ \sin\rho \end{pmatrix} \tag{6.15}$$

Denote the unit vectors of the rotated $\hat{j}$ and $\hat{k}$-axes as $\hat{\mathbf{j}}$ and $\hat{\mathbf{k}}$, and define the components of the unit vectors as

$$\hat{\mathbf{j}} = \begin{pmatrix} \hat{j}_1 \\ \hat{j}_2 \\ \hat{j}_3 \end{pmatrix}, \quad \hat{\mathbf{k}} = \begin{pmatrix} \hat{k}_1 \\ \hat{k}_2 \\ \hat{k}_3 \end{pmatrix} \tag{6.16}$$

Since the $\hat{j}$-axis make an angle of ϕ with the horizontal, the scalar product of $\hat{\mathbf{j}}$ with the Z-axis gives

$$\begin{pmatrix} \hat{j}_1 \\ \hat{j}_2 \\ \hat{j}_3 \end{pmatrix}^T \begin{pmatrix} 0 \\ 0 \\ 1 \end{pmatrix} = \cos(90^\circ - \phi) \;\Rightarrow \hat{j}_3 = \sin\phi \tag{6.17}$$

Similarly, for $\hat{k}$-axis,

$$\begin{pmatrix} \hat{k}_1 \\ \hat{k}_2 \\ \hat{k}_3 \end{pmatrix}^T \begin{pmatrix} 0 \\ 0 \\ 1 \end{pmatrix} = \cos\theta \;\Rightarrow \hat{k}_3 = \cos\theta \tag{6.18}$$

Since $\hat{\mathbf{i}}$, $\hat{\mathbf{j}}$ and $\hat{\mathbf{k}}$ are orthonormal, taking the inner product between the vectors gives

$$\hat{\mathbf{i}}^T\hat{\mathbf{j}} = 0 \;\Rightarrow \hat{j}_1\cos\rho + \hat{j}_3\sin\rho = 0 \tag{6.19}$$

$$\hat{\mathbf{i}}^T\hat{\mathbf{k}} = 0 \;\Rightarrow \hat{k}_1\cos\rho + \hat{k}_3\sin\rho = 0 \tag{6.20}$$

Substituting (6.17) into (6.19) and (6.18) into (6.20) produces

$$\hat{j}_1 = -\hat{j}_3\tan\rho = -\sin\phi\tan\rho \tag{6.21}$$

$$\hat{j}_2 = -sign(a_k)\sqrt{\cos^2\phi - \sin^2\phi\tan^2\rho} \tag{6.22}$$

$$\hat{k}_1 = -\hat{k}_3\tan\rho = -\cos\theta\tan\rho \tag{6.23}$$

$$\hat{k}_2 = sign(a_j)\sqrt{\sin^2\theta - \cos^2\theta\tan^2\rho} \tag{6.24}$$

From (6.15)–(6.24), the rotation matrix representing the elevation, $\mathbf{R}_v$, is then given by

$$\mathbf{R}_v = \begin{pmatrix} \hat{\mathbf{i}} & \hat{\mathbf{j}} & \hat{\mathbf{k}} \end{pmatrix}^T \tag{6.25}$$

6.2.3 Strategy for Singularity Avoidance

It can be observed from (6.21)–(6.24) that the fixed elevation method breaks down when $\rho = \pm 90^\circ$ which corresponds to the case when the $\hat{i}$-axis of the accelerometer is vertical. A singularity avoidance method is proposed here. Before finding the values of ρ, ϕ and θ, the axes corresponding to i, j and k are first determined. This is done by considering the value of μ_{max} corresponding to the maximum absolute value of the component of acceleration, i.e.

$$\mu_{max} = \underset{\mu \in \{x,y,z\}}{\arg\max} \|a_\mu\| \tag{6.26}$$

For the value of μ_{max} obtained, the following singularity avoidance method can be implemented.

Case 1: $\mu_{max} = z$,

$$i = x, j = y, k = z, \mathbf{R}_o = \begin{bmatrix} 1 & 0 & 0 \\ 0 & 1 & 0 \\ 0 & 0 & 1 \end{bmatrix} \tag{6.27}$$

Case 2: $\mu_{max} = y$,

$$i = z, j = x, k = y, \mathbf{R}_o = \begin{bmatrix} 0 & 1 & 0 \\ 0 & 0 & 1 \\ 1 & 0 & 0 \end{bmatrix} \tag{6.28}$$

Case 3: $\mu_{max} = x$,

$$i = y, j = z, k = x, \mathbf{R}_o = \begin{bmatrix} 0 & 0 & 1 \\ 1 & 0 & 0 \\ 0 & 1 & 0 \end{bmatrix} \tag{6.29}$$

The idea of this singularity resolution method is to change the heading axis according to the accelerometer readings such that the angles of ρ, ϕ and θ are kept as small as possible and away from $\pm 90^{\circ}$, thereby avoiding the evaluation of large ratios in (6.11)–(6.13).

6.2.4 Determination of Heading Information

In order to determine $\mathbf{R}_y$, its relationship to the earth magnetic north vector, $\mathbf{h}$, and the magnetic field, $\tilde{\mathbf{m}}$, in the sensor node is first considered as follows

$$\mathbf{R}_v\mathbf{R}_y\mathbf{h} + \mathbf{r}_m = \tilde{\mathbf{m}} = \begin{pmatrix} m_i \\ m_j \\ m_k \end{pmatrix} \tag{6.30}$$

where $\mathbf{r}_m$ is the residual given by the sum of magnetic disturbances $\mathbf{m}_d$ which is to be minimized by taking measurements away from possible magnetic disturbances and the magnetometer noise $\mathbf{v}_m$. $\mathbf{R}_y$ is given in terms of the heading angle, λ, as

$$\mathbf{R}_y = \begin{bmatrix} \cos\lambda & \sin\lambda & 0 \\ -\sin\lambda & \cos\lambda & 0 \\ 0 & 0 & 1 \end{bmatrix} \tag{6.31}$$

If the magnetic inclination angle, α, of the current location is unknown, by substituting (6.31) into (6.30), the linear system of equation can be obtained as

$$\mathbf{R}_v \begin{bmatrix} \cos\lambda\cos\alpha \\ -\sin\lambda\cos\alpha \\ -\sin\alpha \end{bmatrix} = \frac{1}{H}\begin{pmatrix} m_i \\ m_j \\ m_k \end{pmatrix} - \mathbf{r}_m \tag{6.32}$$

The system of equations given by (6.32) can be solved to obtain the values of α and λ. In a new location where the inclination angle is unknown, (6.32) can be used to first determine the value of α. Once α is determined, the value of λ can

be solved using the overdetermined system of equation which can be obtained by re-expressing (6.32)

$$\cos\alpha \begin{bmatrix} \hat{i}_1 & 0 \\ \hat{j}_1 & -\hat{j}_2 \\ \hat{k}_1 & -\hat{k}_2 \end{bmatrix} \begin{bmatrix} \cos\lambda \\ \sin\lambda \end{bmatrix} = \begin{bmatrix} m_i + \hat{i}_3 \sin\alpha \\ m_j + \hat{j}_3 \sin\alpha \\ m_k + \hat{k}_3 \sin\alpha \end{bmatrix} - \mathbf{r}_m \tag{6.33}$$

With $\mathbf{R}_v$, $\mathbf{R}_o$ and $\mathbf{R}_y$ found, the overall equivalent rotation matrix $\mathbf{R}$ can be found using (6.10). The equivalent axis of rotation $\mathbf{v}$, and the rotation angle θ_v can also be easily determined as

$$\mathbf{v} = \begin{pmatrix} r_{23} - r_{32} \\ r_{31} - r_{13} \\ r_{12} - r_{21} \end{pmatrix} \tag{6.34}$$

$$\theta_v = \cos^{-1}\left(\frac{tr\,(\mathbf{R}) - 1}{2}\right) \tag{6.35}$$

6.3 Experimental Evaluation

To validate experimentally the performance of the proposed elevation and heading based algorithm, a gyroscope and magnetometer has been added to the initial sensor node design based on a triaxial accelerometer presented in Section 3.2. Fig. 6.2 shows a photograph of the new sensor node. Each new sensor node is now equipped with a Freescale MMA7361L triaxial accelerometer, Invensense ITG-3200 triaxial gyroscope and Honeywell HMC5843 triaxial magnetometer. The power consumption of each sensor node is about 120mW. The dimension of each sensor node is 49×39×16mm and weighs 20g with battery (15g without battery).

The sensor nodes were attached on the left forearm and the upperarm as shown in Fig. 5.8. In this experiment, the upperarm is held vertically next to the body such that the elbow joint is stationary. The forearm is first held in

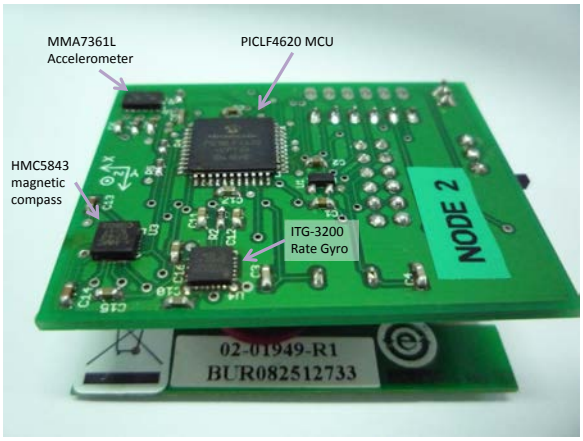

Figure 6.2. Photograph of a sensor node with triaxial accelerometer, gyroscope and magnetometer

the horizontal position, after which it is flexed upwards and extended downwards. As the forearm is in the vertically downwards position, a pronation/ supination motion is performed. Following which, the forearm is flexed back to the horizontal position and a medial/ lateral rotation of the upperarm is performed. Finally, a pronation/ supination motion of the forearm is performed while it is in the horizontal position.

6.3.1 Singularity Avoidance

Fig. 6.3 shows the plot of the elevation and heading angles of the sensor node attached to the forearm with and without implementing the singularity avoidance strategy described in Section 6.2.3. The elevation angle ρ of the heading i-axis and elevation angle ϕ of the j-axis of the sensor node with respect to the horizontal plane is shown in Fig. 6.3(a)–(b). The heading angle, defined as the angle between the projection of the heading axis of the sensor node on the horizontal plane and the magnetic north, is shown in Fig. 6.3(c). The value of μ_{max} which is used for the strategy for singularity avoidance is given in Fig. 6.3(d). The corresponding arm positions of the arm at various times are also shown in Fig. 6.3(e). Fig. 6.4 shows the corresponding values of $\tan(\rho)$ with and without implementation of the

singularity avoidance strategy.

Without implementing the singularity avoidance strategy, the heading axis of the sensor node is taken to the x-axis and the elevation angle can take values from -90° to 90°. This can pose a problem during implementation when using the tangent function in (6.21)–(6.24) of the proposed algorithm. With singularity avoidance, it can be seen from Fig. 6.3 that when the magnitude of the elevation angle ρ without singularity avoidance approaches ±90°, the heading axis changes accordingly to μ_{max} such that the elevation angle ρ with singularity avoidance does not exceed 45°. The behaviour of the ϕ and λ angles with singularity avoidance during 5-8 s are also more stable compared with that without singularity avoidance. This can also be observed from Fig. 6.4, in which the magnitude of the value of $\tan(\rho)$ with singularity avoidance is kept below 1 whereas the magnitude of $\tan(\rho)$ without singularity avoidance can suffer a sudden spike in value when ρ approaches ±90° as seen at the 6.5s. As such, by employing the singularity avoidance strategy, the fixed elevation and heading algorithm can be easily implemented in a fixed-point processor without arithmetic overflow and with improved accuracy and performance.

6.3.2 Benchmarking with other algorithm

The performance of this algorithm is next benchmarked with another algorithm utilising the inertial/magnetic sensors for orientation determination. The algorithm used for benchmarking is an indirect Kalman filter with adaptive estimation of external acceleration recently proposed by Suh [64]. The magnetic sensor in the Kalman filter is also used only for yaw angle estimation. Fig. 6.5 shows the performance of the proposed algorithm as compared with the indirect Kalman filter. For comparison purpose, the elevation and heading angles are converted to the Euler angles of yaw, pitch and roll. The angle of difference, defined as the angle in which the orientation determined by the proposed algorithm is to rotate

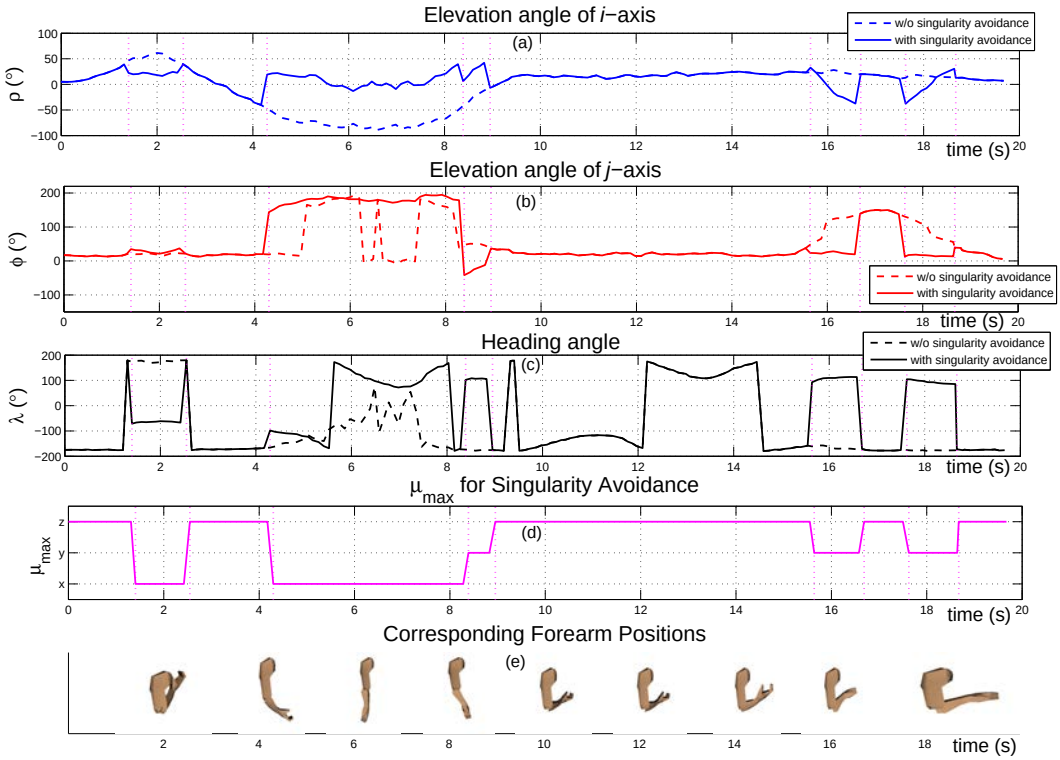

Figure 6.3. Plot of heading and elevation angles of sensor node attached to forearm

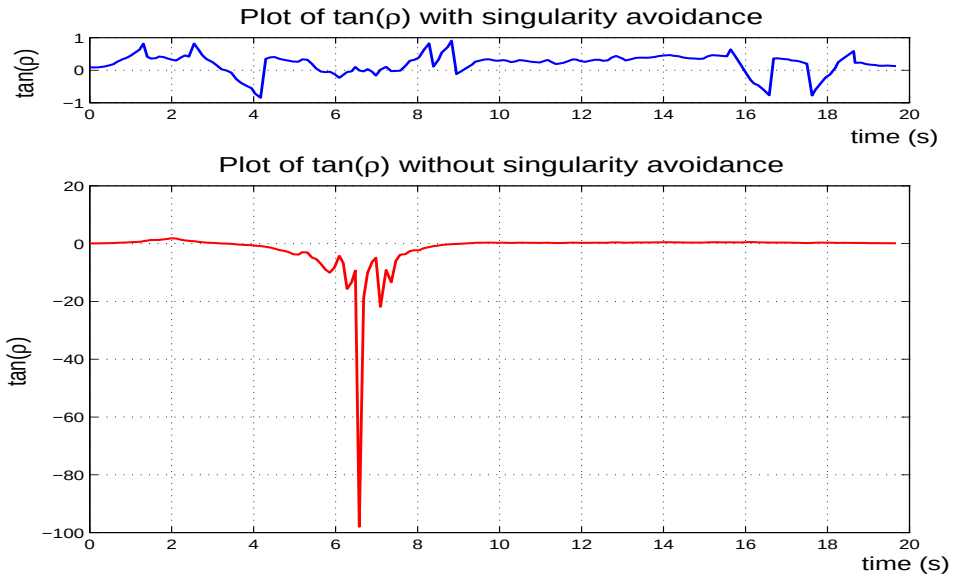

Figure 6.4. Plot of tan(ρ) with and without singularity avoidance

to obtain the orientation given by the indirect Kalman filter, is also shown at the bottom of the figure.

As can be seen, the Euler angles obtained from the proposed algorithm follows closely of that obtained using the indirect Kalman filter except at the singular state when the pitch angle is close to 90° during 5-8s in which the roll and yaw angles are erratic. This can be compared with the relatively stable elevation and heading angle in Fig. 6.3 with singularity avoidance. The mean difference between the indirect Kalman filter and the proposed algorithm is 3.2225° while the standard deviation is 7.4267° respectively. In terms of algorithmic efficiency, the proposed algorithm took an average of 0.622 ms for each data sample while the indirect Kalman filter took an average of 1.22 ms.

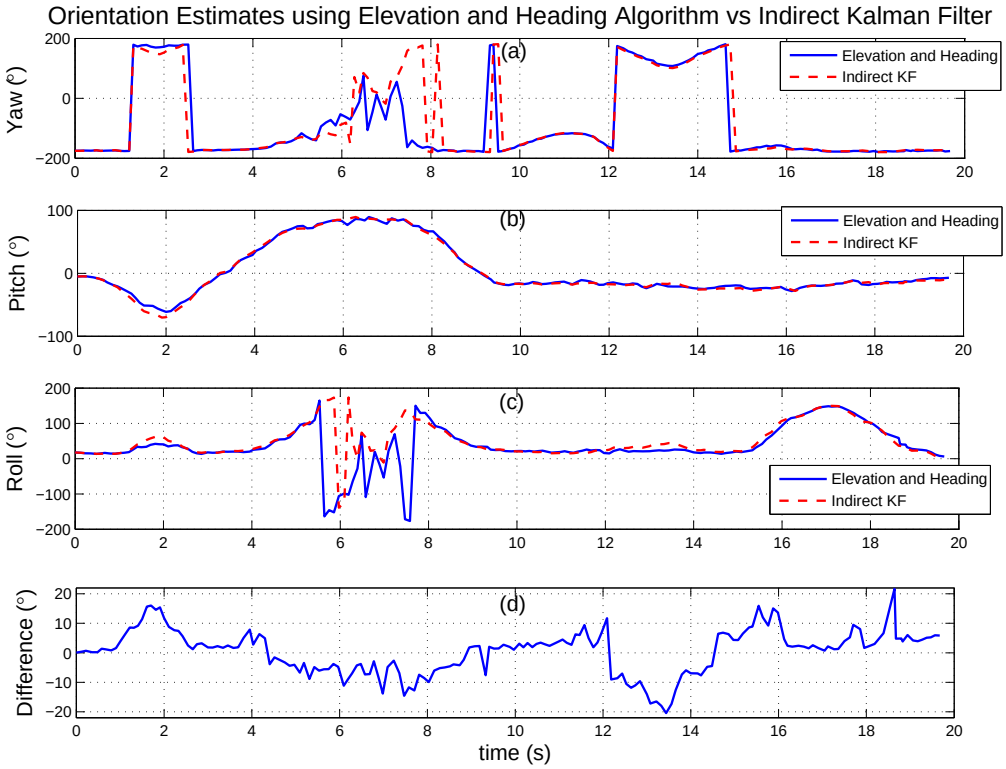

Figure 6.5. Benchmarking the performance of the proposed algorithm with indirect Kalman filter

6.3.3 Decoupling of magnetometer and accelerometer output

Next, the performance of the proposed algorithm is evaluated under the influence of a magnetic disturbance. In this experiment, the arm was held stationary at the horizontal position and a magnetic disturbance was applied to the sensor node at the forearm by bringing a magnet close to it. The estimated elevation and heading angles together with the magnetometer output are given in Fig. 6.6.

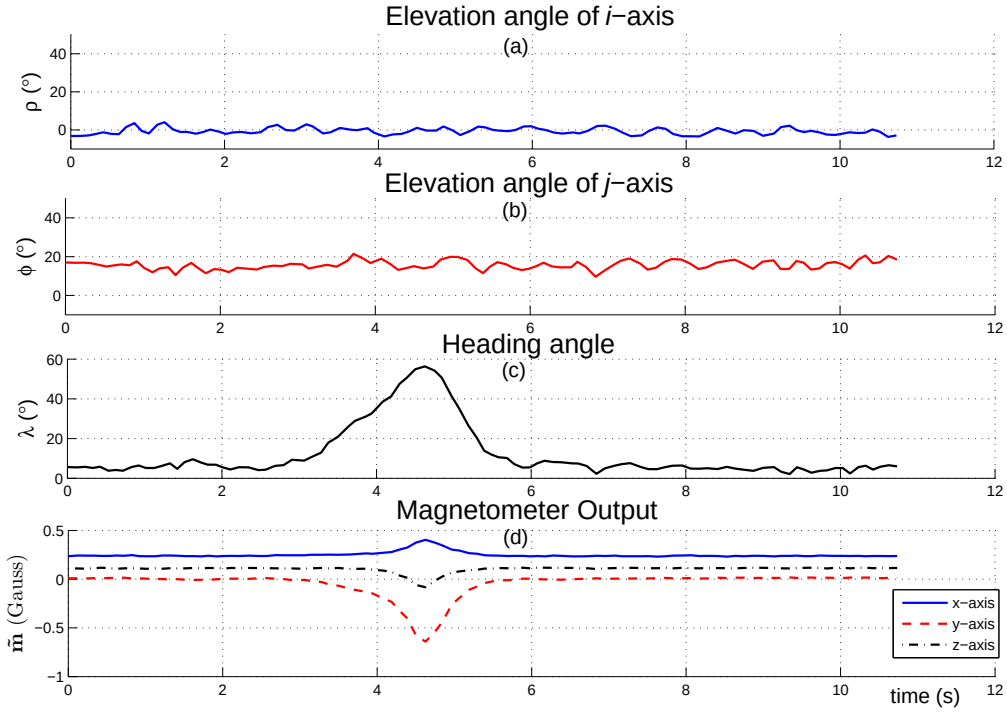

Figure 6.6. Performance of the proposed algorithm under magnetic disturbances

From the results, the influence of a magnetic disturbance at the 3-6s causes only the heading angle to deviate from the initial values. The elevation angles of ρ and ϕ are unaffected by the magnetic disturbance.

6.4 Summary

In this chapter, a novel sensor fusion algorithm for orientation determination using the accelerometer, gyroscope and magnetometer sensors is formulated. Instead of finding the conventional Euler angles, elevation angles of the sensor's coordinate frame axes with respect to the horizontal plane and the heading angle with respect to the magnetic north are determined. These angles are independent on the temporal order and can be visualized easily for a given orientation. Singularities that may arise in the estimation of the angles are avoided using a novel singularity avoidance method which changes the heading axes adaptively using the accelerometer output. Finally, by estimating the angular velocity and acceleration using the gyroscope output, the external acceleration in the accelerometer output can be compensated in dynamic movements.

The performance of the proposed elevation and heading algorithm is also evaluated experimentally using the wireless sensor network platform described in Chapter 3 but with an additional triaxial gyroscope and magnetometer added to each sensor node. Experimental results show that the performance of the elevation and heading algorithm is comparable to an indirect Kalman filter at a reduced computational cost. With the singularity avoidance strategy, the maximum value of the elevation angle of the heading axis is capped, allowing for the implementation of the algorithm in a fixed point processor without arithmetic overflow. The presence of magnetic disturbances affects only the accuracy of the heading angles and not the elevation angles.

CHAPTER 7

Conclusion and Future Work

7.1 Conclusions

In this thesis, the development of a wearable wireless sensor network for unrestrained measurement of the human arm limb has been presented together with preliminary studies on its use for tilt determination. A factorized quaternion approach has also been proposed to determine the orientation of the upperarm and forearm along a single plane taking into account the sensor and anatomical constraint. Determination of orientation can be extended using a triad of accelerometer, gyroscope and magnetometer sensors with a proposed sensor fusion algorithm based on elevation and heading angles. Simulations and experiments have also been performed to evaluate the performance of the proposed algorithms. In this concluding chapter, a summary of the contribution of the research work performed together with the experimental findings is given together with recommendations for future work.

7.1.1 Development of a wearable wireless sensor network for arm motion measurement

In our research, an ambulatory and unrestrained measurement system based on a wearable wireless sensor network for tracking the human arm motion has been proposed and developed. The wearable wireless sensor network system based on accelerometers was developed in 2008 and reported in 2009 [93]. At that time,

most of the inertial based sensors in the market such as the Xsens MTx were wired and cumbersome. A wireless sensor network based system for motion measurement was relatively new at that time and provided an advantage of unhindered measurement of natural human motion. (It is noted that to date, several similar commercial platforms have appeared.) To study the accuracy of tilt measurement using the triaxial accelerometers, controlled rotations were performed on a rotary stage at various angular speeds and a mean error of 0.52° was found. This mean error obtained is comparable to the accuracy obtained from a similar accelerometer based tilt angle sensing commercial product (for example, MicroStrain's accelerometer based flexion angle system FAS-A® inclinometer with an orientation accuracy of ±0.7°). Sensor nodes were also mounted on a human arm and the accuracy of tilt measurement is benchmarked using a goniometer. Experimental results show that the mean difference in angle increases from close to 0° at a mean angular speed of $10°/s$ to 3.5° at a mean angular speed of 80°. These results demonstrate that the accuracy of the system is sufficiently good for the targeted rehabilitation application where the angular velocity of the arm movement is less than 20°/s. Moreover, the latency of the system is less than 60 ms for a two-node network, making it suitable for real-time implementation. Evaluation of the power consumption shows that the system can last for a week with a daily usage of 8 hours. As compared to other existing approaches, the proposed system is portable and easy to use. It allows the patients to be monitored without restraint and rehabilitation can be carried out in a home environment instead of a specialized laboratory in the hospital.

7.1.2 Factorized Principal-axis Quaternion Approach

A new approach based on factorized principal axis quaternions to determine the orientation of the articulated human arm limb has been proposed in this thesis. Unlike other approaches, the proposed approach is formulated with sensor and

anatomical constraints and uses only tri-axial accelerometers. It is shown that measurement of the orientation of the upperarm can be taken along a vertical plane. Measurement of the orientation of the forearm can be extended along a titled plane from the vertical by making use of information on the orientation of the upperarm. As compared with the conventional approach using a single angle-axis quaternion, the proposed approach overcomes the problems of the transient singularities and ambiguity that arise from the use of tri-axial accelerometer. Experimental results show that the mean difference in angle of flexion/extension of the upperarm is -2.12° while lateral/medial rotation is -3.68°. For the forearm, the mean difference in angle of flexion/extension is -3.08° while pronation/supination is -0.22°. The typical power consumption of our sensor node is 89mW as compared to 350mW for the IMU. Experimental results have validated the proposed approach, showing a comparable accuracy when benchmarked with a multiple sensor IMU.

7.1.3 Elevation and Heading Angles Algorithm

A new approach based on fixed elevation and heading angles for orientation determination has also been proposed in this thesis. Instead of the conventional Euler angles, the elevation angle of the sensor axis is used together with the angle between the projection of the heading axis on the horizontal plane and the magnetic north. These elevation and heading angles are independent of temporal order and are easily visualized for a given orientation. A novel singularity avoidance strategy was also proposed to allow measurement through all possible orientations. Compensation of external acceleration for arm rotation motion using the gyroscope output was performed by modelling the kinematics of the arm limb. As the magnetometer is easily affected by magnetic disturbances caused by electrical appliances and ferrous materials, it is decoupled from the accelerometer and used solely for the determination of heading. Experimental results show that

the performance of the proposed algorithm is comparable to an indirect Kalman filter with a mean difference of 3.2225° and at 50% of the computational cost. The implementation of the singularity avoidance strategy limits the magnitude of the tangent of the heading axis elevation angle to below one and makes it suitable for implementation in a fixed-point processor. Magnetic disturbances applied to the sensor influence only the accuracy of the heading angle and the elevation angles are unaffected.

7.2 Future Work

The following section outlines the suggestion for future work and the direction this research can take in consideration of the current research and developments.

7.2.1 Estimation of external acceleration of articulated arm limb

In the proposed elevation and heading algorithm in Chapter 6, the joint corresponding to the center of rotation is assumed to be stationary. In the experiments conducted to evaluate the performance of the proposed algorithm of the forearm, the upperarm was kept stationary beside the body. To allow for orientation measurement of the free moving articulated arm, the acceleration of the elbow joint has to be estimated by making use of the information on the angular velocity and acceleration of the upperarm. Future work can investigate how to simultaneously use the information from the gyroscope sensors attached to the upperarm and the forearm to achieve this purpose.

7.2.2 Estimation of yaw angle of the forearm

Since the forearm can only perform flexion/extension and pronation/supination, the heading angle of the forearm can be deduced from the orientation of the

upperarm. This can be used to improve the accuracy of heading information by combining the magnetometer data from both the sensor nodes attached to the upperarm and forearm and improve the robustness to local magnetic disturbances which affect only either one of the sensor nodes.

7.2.3 Extension of orientation determination to other body parts

In this thesis, orientation determination of the arm is demonstrated in a sagittal using only accelerometers and extended through all orientations using an additional magnetometer and gyroscope sensor. A natural extension of this work is to determine the orientation of the other parts of the human body such as the leg, torso and head etc. Determination of the orientation of the leg during walking is complicated by the fact that the accelerometer readings suffers a sudden spike during the impact of the foot with the ground.

7.2.4 Implementation of wireless technology

To enable real time wireless monitoring of the whole human body movements, an increased number of wireless sensor nodes needs to be implemented in the sensor network. This also bring forth increased challenges in multiple access such as collision avoidance, data throughput, multihop and interference from other wireless networks. During the time of this research, IEEE 802 established a Task Group called IEEE802.15.6 for the standardization of of Wireless Body Area Network (WBAN) [94, 95]. This standard specifies the short range communication in the vicinity of, or inside, of a human body. Support for quality of service (QoS), extremely low power, and data rates up to 10 Mbps is required while simultaneously complying with strict non-interference guidelines where needed. Effects on portable antennas due to the presence of a person, radiation pattern shaping to

minimize the specific absorption rate (SAR) into the body, and changes in characteristics as a result of the user motions are also considered in this standard. To meet the medical and relevant communication regulations for medical and consumer electronics applications, future design of the wireless sensor network will have to take this new standard into account.

7.2.5 Inertial Navigation with RSS Measurements

Besides providing data from the inertial sensors as with a wired motion tracking system, the wireless wearable sensor network proposed and developed in this thesis is also able to provide RSS measurements at near zero cost from the received data packets. Although the focus of the thesis is on orientation determination of the human arm limb, an extension of the current work to a full-fledged six degrees of freedom human motion tracking system will also require determination of the position of the subject. MEMS inertial sensors have already been demonstrated for pedestrian dead reckoning and inertial navigation [96, 97]. RSS measurements on the other hand are also known to be used for localization [98, 99]. As such, data fusion of the inertial sensors and RSS measurements can be performed in a future work using the developed wearable wireless sensor network to obtain a more accurate position estimate for the subject.

7.2.6 Improved Sensor Technology

As our research work is going on, new sensor components continue to appear on the market. These new sensors continue to improve in smaller packages, consume lower power and are cheaper with mass production. Analog Devices has developed tactical grade MEMS gyroscopes (with bias stability of less than 10°/hour) which rivals fiber optics gyroscopes with smaller size, lighter weight and less power consumption. STMicroelectronics has made the first combination accelerometer and magnetometer in a single package in the market to take advantage of applications

such as augmented reality, 3D gaming and eHealth based on combined data extracted from magnetometers and accelerometers. Future revision of the wireless sensor nodes design can be designed to take advantage of these improvements in commercial sensor technologies.

In addition, promising research on sensor development continues to be reported. Of particular interest is the work on an angle measuring gyroscope [100] based on the principle of a Foucault's pendulum on a chip. All commercial MEMS gyroscope today are angular rate measuring sensors and perform integrations to determine the actual angle of rotation. The device built is capable of measuring angles faster and more accurately than current MEMS-based gyroscopes. It is envisioned that this new type of microscopic gyroscope can lead to better inertial navigation systems, better rollover protection in automobiles and balance restoring implants for the elderly.

List of Author's Publication

- G. X. Lee, K. S. Low and T. Taher, "Unrestrained Measurement of Arm Motion Based on a Wearable Wireless Sensor Network," *IEEE Transactions on Instrumentation and Measurement*, vol. 59, pp. 1309-1317, 2010.
- K. S. Low, G. X. Lee and T. Taher, "A Wearable Wireless Sensor Network for Human Limbs Monitoring," *in IEEE Instrumentation and Measurement Technology Conference I2MTC '09*, 2009, pp. 1332-1336.
- G. X. Lee and K. S. Low, "Factorized Quaternion Approach to Determine Arm Motions Using Tri-axial Accelerometers with Anatomical and Sensor Constraints," *IEEE Transactions on Instrumentation and Measurement*, vol. 61, pp. 1793-1802, 2012.
- K. S. Low and G. X. Lee , "Experimental Evaluation of Arm Motion Using Tri-axial Acceleromters based on Factorized Quaternion Approach," *in IEEE International Conference on Industrial Technology (ICIT)*, 2012, pp. 172-177.
- G. X. Lee and K. S. Low , "An Elevation and Heading Based Algorithm for Determination of Arm Limb Orientation," submitting to *IEEE Transactions on Instrumentation and Measurement*,

Bibliography

[1] J. M. Zheng, K. W. Chan, and I. Gibson, "Virtual reality," *IEEE Potentials*, vol. 17, no. 2, pp. 20–23, 1998.

[2] D. Jack, R. Boian, A. S. Merians, M. Tremaine, G. C. Burdea, S. V. Adamovich, M. Recce, and H. Poizner, "Virtual reality-enhanced stroke rehabilitation," *IEEE Transactions on Neural Systems and Rehabilitation Engineering*, vol. 9, no. 3, pp. 308–318, 2001.

[3] G. Zorpette, "Reverse engineering the human face," *IEEE Spectrum*, vol. 47, no. 4, pp. 18–18, 2010.

[4] M. Ermes, J. Pärkkä, J. Mäntyjärvi, and I. Korhonen, "Detection of daily activities and sports with wearable sensors in controlled and uncontrolled conditions," *IEEE Transactions on Information Technology in Biomedicine*, vol. 12, no. 1, pp. 20–26, 2008.

[5] D. Fitzgerald, J. Foody, D. Kelly, T. Ward, C. Markham, J. McDonald, and B. Caulfield, "Development of a wearable motion capture suit and virtual reality biofeedback system for the instruction and analysis of sports rehabilitation exercises," in *Proceedings of the 29th Annual International Conference of the IEEE Engineering in Medicine and Biology Society, EMBS '07*, 2007, pp. 4870–4874.

[6] H. Zhou and H. Hu, "Human motion tracking for rehabilitation – a survey," *Biomedical Signal Processing and Control*, vol. 3, no. 1, pp. 1–18, 2008.

[7] T. B. Moeslund, A. Hilton, and V. Krüger, "A survey of advances in vision-based human motion capture and analysis," *Computer Vision and Image Understanding*, vol. 104, no. 2-3, pp. 90–126, 2006.

[8] G. Welch and E. Foxlin, "Motion tracking: no silver bullet, but a respectable arsenal," *IEEE Computer Graphics and Applications*, vol. 22, no. 6, pp. 24–38, 2002.

[9] G. Å. Hansson, I. Balogh, K. Ohlsson, L. Rylander, and S. Skerfving, "Goniometer measurement and computer analysis of wrist angles and movements applied to occupational repetitive work," *Journal of Electromyography and Kinesiology*, vol. 6, no. 1, pp. 23–35, 1996.

[10] L. Wang, W. Hu, and T. Tan, "Recent developments in human motion analysis," *Pattern Recognition*, vol. 36, no. 3, pp. 585–601, 2003.

[11] F. H. Raab, E. B. Blood, T. O. Steiner, and H. R. Jones, "Magnetic position and orientation tracking system," *IEEE Transactions on Aerospace and Electronic Systems*, vol. AES-15, no. 5, pp. 709–718, 1979.

[12] http://www.ascension-tech.com/.

[13] S. Miyazaki, "Long-term unrestrained measurement of stride length and walking velocity utilizing a piezoelectric gyroscope," *IEEE Transactions on Biomedical Engineering*, vol. 44, no. 8, pp. 753–759, 1997.

[14] B. Kemp, A. J. M. W. Janssen, and B. van der Kamp, "Body position can be monitored in 3D using miniature accelerometers and earth-magnetic field sensors," *Electroencephalography and Clinical Neurophysiology/Electromyography and Motor Control*, vol. 109, no. 6, pp. 484–488, 1998.

[15] D. Roetenberg, H. J. Luinge, C. T. M. Baten, and P. H. Veltink, "Compensation of magnetic disturbances improves inertial and magnetic sensing of human body segment orientation," *IEEE Transactions on Neural Systems and Rehabilitation Engineering*, vol. 13, no. 3, pp. 395–405, 2005.

[16] R. Zhu and Z. Zhou, "A real-time articulated human motion tracking using tri-axis inertial/magnetic sensors package," *IEEE Transactions on Neural Systems and Rehabilitation Engineering*, vol. 12, no. 2, pp. 295–302, 2004.

[17] X. Yun and E. R. Bachmann, "Design, implementation, and experimental results of a quaternion-based Kalman filter for human body motion tracking," *IEEE Transactions on Robotics*, vol. 22, no. 6, pp. 1216–1227, 2006.

[18] T. J. Dishongh and M. McGrath, *Wireless sensor networks for healthcare applications*. Boston: Artech House, 2010.

[19] C. Jadhav and V. Krovi, "A low-cost framework for individualized interactive telerehabilitation," in *Proceedings of the 26th Annual International Conference of the IEEE Engineering in Medicine and Biology Society, IEMBS '04*, vol. 2, 2004, pp. 3297–3300.

[20] Y. Tao and H. Hu, "A novel sensing and data fusion system for 3-D arm motion tracking in telerehabilitation," *IEEE Transactions on Instrumentation and Measurement*, vol. 57, no. 5, pp. 1029–1040, 2008.

[21] S. Tanaka, K. Motoi, M. Nogawa, and K. Yamakoshi, "A new portable device for ambulatory monitoring of human posture and walking velocity using miniature accelerometers and gyroscope," in *Proceedings of the 26th Annual International Conference of the IEEE Engineering in Medicine and Biology Society, IEMBS '04*, vol. 1, 2004, pp. 2283–2286.

[22] G. M. Bertolotti, A. Cristiani, R. Gandolfi, and R. Lombardi, "A portable system for measuring human body movement," in *9th EUROMICRO Conference on Digital System Design: Architectures, Methods and Tools, DSD '06*, 2006, pp. 569–576.

[23] P. F. Binkley, "Predicting the potential of wearable technology," *IEEE Engineering in Medicine and Biology Magazine*, vol. 22, no. 3, pp. 23–27, 2003.

[24] H. Zhou, H. Hu, and N. Harris, "Application of wearable inertial sensors in stroke rehabilitation," in *27th Annual International Conference of the Engineering in Medicine and Biology Society, (IEEE-EMBS '05)*, 2005, pp. 6825–6828.

[25] T. Liu, Y. Inoue, and K. Shibata, "A wearable sensor system for human motion analysis and humanoid robot control," in *Proceedings of the 2006 IEEE International Conference on Robotics and Biomimetics, ROBIO '06*, 2006, pp. 43–48.

[26] T. Liu, Y. Inoue, K. Shibata, and R. Zheng, "Measurement of human lower limb orientations and ground reaction forces using wearable sensor systems," in *Proceedings of the 2007 IEEE/ASME International Conference on Advanced Intelligent Mechatronics*, 2007, pp. 1–6.

[27] H. J. Luinge and P. H. Veltink, "Inclination measurement of human movement using a 3-D accelerometer with autocalibration," *IEEE Transactions on Neural Systems and Rehabilitation Engineering*, vol. 12, no. 1, pp. 112–121, 2004.

[28] B. Andò, S. Baglio, and C. Trigona, "Autonomous sensors: From standard to advanced solutions [Instrumentation notes]," *IEEE Instrumentation & Measurement Magazine,*, vol. 13, no. 3, pp. 33–37, 2010.

[29] J. R. W. Morris, "Accelerometry – A technique for the measurement of human body movements," *Journal of Biomechanics*, vol. 6, no. 6, pp. 729–732, IN17, 733–736, 1973.

[30] M. Caruso and C. Smith, "A new perspective on magnetic field sensing," in *Sensors Expo Proceedings*, 1998, pp. 195–213.

[31] P. Ripka, *Magnetic sensors and magnetometers*, ser. Artech House remote sensing library. Boston: Artech House, 2001.

[32] R. Collinson, *Introduction to Avionics Systems*, 3rd ed. Springer Science+Business Media B.V., 2011.

[33] E. Bernmark and C. Wiktorin, "A triaxial accelerometer for measuring arm movements," *Applied Ergonomics*, vol. 33, no. 6, pp. 541–547, 2002.

[34] P. Cheng, F. Linnarsson, and B. Oelmann, "Joint angular sensor based on distributed biaxial MEMS accelerometers," in *33rd Annual Conference of the IEEE Industrial Electronics Society, IECON '07*, 2007, pp. 2242–2247.

[35] C. T. Chen, *Linear System Theory and Design*, 3rd ed. Oxford University Press, 1999.

[36] J. Lee and I. Ha, "Sensor fusion and calibration for motion captures using accelerometers," in *Proceedings of the 1999 IEEE International Conference on Robotics and Automation*, vol. 3, 1999, pp. 1954–1959.

[37] H. Rehbinder and X. Hu, "Drift-free attitude estimation for accelerated rigid bodies," in *Proceedings of the 2001 IEEE International Conference on Robotics and Automation, ICRA'01*, vol. 4, 2001, pp. 4244–4249.

[38] H. J. Luinge and P. H. Veltink, "Measuring orientation of human body segments using miniature gyroscopes and accelerometers," *Medical & Biological Engineering & Computing*, vol. 43, no. 2, pp. 273–82, 2005.

[39] H. J. Luinge, P. H. Veltink, and C. T. M. Baten, "Ambulatory measurement of arm orientation," *Journal of Biomechanics*, vol. 40, no. 1, pp. 78–85, 2007.

[40] Z. Zhang, Z. Huang, and J. Wu, "Hierarchical information fusion for human upper limb motion capture," in *12th International Conference on Information Fusion, FUSION '09*, 2009, pp. 1704–1711.

[41] D. Gebre-Egziabher, G. H. Elkaim, J. D. Powell, and B. W. Parkinson, "A gyro-free quaternion-based attitude determination system suitable for implementation using low cost sensors," in *IEEE Position Location and Navigation Symposium*, 2000, pp. 185–192.

[42] G. Wahba, "A least squares estimate of satellite attitude," *SIAM Review*, vol. 7, no. 3, pp. 409–409, 1965.

[43] R. Zhu, Z. Zhou, S. Li, and X. Sun, "A novel miniature azimuth-level detector based on MEMS," in *Microelectromechanical Systems Conference*, 2001, pp. 50–53.

[44] X. Yun, E. R. Bachmann, and R. B. McGhee, "A simplified quaternion-based algorithm for orientation estimation from earth gravity and magnetic field measurements," *IEEE Transactions on Instrumentation and Measurement*, vol. 57, no. 3, pp. 638–650, 2008.

[45] M. D. Shuster and S. D. Oh, "Three-axis attitude determination from vector observations," *Journal of Guidance and Control*, vol. 4, pp. 70–77, 1981.

[46] W. D. Jones, "A compass in every smartphone," *IEEE Spectrum*, vol. 47, no. 2, pp. 12–13, 2010.

[47] D. Gebre-Egziabher, G. H. Elkaim, J. D. Powell, and B. W. Parkinson, "Calibration of strapdown magnetometers in magnetic field domain," *Journal of Aerospace Engineering*, vol. 19, no. 2, pp. 87–102, 2006.

[48] P. Guo, H. Qiu, Y. Yang, and Z. Ren, "The soft iron and hard iron calibration method using extended Kalman filter for attitude and heading reference system," in *IEEE/ION Position, Location and Navigation Symposium*, 2008, pp. 1167–1174.

[49] E. Foxlin, "Inertial head-tracker sensor fusion by a complementary separate-bias Kalman filter," in *Proceedings of the 1996 IEEE Virtual Reality Annual International Symposium*.

[50] B. Friedland, "Treatment of bias in recursive filtering," *IEEE Transactions on Automatic Control*, vol. 14, no. 4, pp. 359–367, 1969.

[51] R. Zhu and Z. Zhou, "A small low-cost hybrid orientation system and its error analysis," *IEEE Sensors Journal*, vol. 9, no. 3, pp. 223–230, 2009.

[52] R. E. Mortensen, "Strapdown guidance error analysis," *IEEE Transactions on Aerospace and Electronic Systems*, vol. AES-10, no. 4, pp. 451–457, 1974.

[53] E. R. Bachmann, I. Duman, U. Y. Usta, R. B. McGhee, X. P. Yun, and M. J. Zyda, "Orientation tracking for humans and robots using inertial sensors," in *International Symposium on Computational Intelligence in Robotics & Automation (CIRA99)*, 1999, pp. 187–194.

[54] E. R. Bachmann, R. B. McGhee, X. Yun, and M. J. Zyda, "Inertial and magnetic posture tracking for inserting humans into networked virtual environments," in *Proceedings of the ACM symposium on Virtual reality software and technology*. ACM, 2001, pp. 9–16.

[55] E. R. Bachmann and X. Yun, "A single parameter tunable quaternion based attitude estimation filter," *Navigation: Journal of the Institute of Navigation*, vol. 53, no. Compendex, pp. 109–120, 2006.

[56] J. L. Marins, X. Yun, E. R. Bachmann, R. B. McGhee, and M. J. Zyda, "An extended Kalman filter for quaternion-based orientation estimation using MARG sensors," in *Proceedings of the 2001 IEEE/RSJ International Conference on Intelligent Robots and Systems*, vol. 4, 2001, pp. 2003–2011.

[57] X. Yun, M. Lizarraga, E. R. Bachmann, and R. B. McGhee, "An improved quaternion-based Kalman filter for real-time tracking of rigid body orientation," in *Proceedings of the 2003 IEEE/RSJ International Conference on Intelligent Robots and Systems (IROS '03)*, vol. 2, 2003, pp. 1074–1079.

[58] X. Yun, C. Aparicio, E. R. Bachmann, and R. B. McGhee, "Implementation and experimental results of a quaternion-based Kalman filter for human body motion tracking," in *Proceedings of the 2005 IEEE International Conference on Robotics and Automation, ICRA '05*, 2005, pp. 317–322.

[59] E. R. Bachmann, X. Yun, D. McKinney, R. B. McGhee, and M. J. Zyda, "Design and implementation of MARG sensors for 3-DOF orientation measurement of rigid bodies," in *Proceedings of the 2003 IEEE International Conference on Robotics and Automation, ICRA '03*, vol. 1, 2003, pp. 1171–1178.

[60] X. Yun, E. R. Bachmann, A. Kavousanos-Kavousanakis, F. Yildiz, and R. B. McGhee, "Design and implementation of the MARG human body motion tracking system," in *Proceedings of the 2004 IEEE/RSJ International Conference on Intelligent Robots and Systems, (IROS '04)*, vol. 1, 2004, pp. 625–630.

[61] J. Calusdian, X. Yun, and E. R. Bachmann, "Adaptive-gain complementary filter of inertial and magnetic data for orientation estimation," in *IEEE International Conference on Robotics and Automation (ICRA '11)*, 2011, pp. 1916–1922.

[62] D. Roetenberg, C. T. M. Baten, and P. H. Veltink, "Estimating body segment orientation by applying inertial and magnetic sensing near ferromagnetic materials," *IEEE Transactions on Neural Systems and Rehabilitation Engineering*, vol. 15, no. 3, pp. 469–471, 2007.

[63] A. M. Sabatini, "Quaternion-based extended Kalman filter for determining orientation by inertial and magnetic sensing," *IEEE Transactions on Biomedical Engineering*, vol. 53, no. 7, pp. 1346–1356, 2006.

[64] Y. S. Suh, "Orientation estimation using a quaternion-based indirect Kalman filter with adaptive estimation of external acceleration," *IEEE Transactions on Instrumentation and Measurement*, vol. 59, no. 12, pp. 3296–3305, 2010.

[65] Z. Q. Zhang and J. K. Wu, "A novel hierarchical information fusion method for three-dimensional upper limb motion estimation," *IEEE Transactions on Instrumentation and Measurement*, vol. 60, no. 11, pp. 3709–3719, 2011.

[66] H. Zhou and H. Hu, "Inertial motion tracking of human arm movements in stroke rehabilitation," in *Proceedings of the 2005 IEEE International Conference on Mechatronics and Automation*, vol. 3, 2005, pp. 1306–1311.

[67] ——, "Reducing drifts in the inertial measurements of wrist and elbow positions," *IEEE Transactions on Instrumentation and Measurement*, vol. 59, no. 3, pp. 575–585, 2010.

[68] E. Foxlin, M. Harrington, and G. Pfeifer, "Constellation: a wide-range wireless motion-tracking system for augmented reality and virtual set applications," in *Proceedings of the 25th Annual Conference on Computer Graphics and Interactive Techniques*. ACM, 1998, pp. 371–378.

[69] D. Roetenberg, P. J. Slycke, and P. H. Veltink, "Ambulatory position and orientation tracking fusing magnetic and inertial sensing," *IEEE Transactions on Biomedical Engineering*, vol. 54, no. 5, pp. 883–890, 2007.

[70] D. Roetenberg, P. Slycke, A. Ventevogel, and P. H. Veltink, "A portable magnetic position and orientation tracker," *Sensors and Actuators A: Physical*, vol. 135, no. 2, pp. 426–432, 2007.

[71] J. B. Kuipers, *Quaternions and Rotation Sequences : A Primer with Applications to Orbits, Aerospace, and Virtual Reality*. Princeton, N.J.: Princeton University Press, 1999.

[72] Y. Tao and H. Hu, "3D arm motion tracking for home-based rehabilitation," in *3rd Cambridge Workshop on universal access and assistive technology (CWUAAT 06)*, 2006, pp. 105–111.

[73] J. A. Gutiérrez, E. H. Callaway, Jr., and R. L. Barrett, Jr., *Low-Rate Wireless Personal Area Networks, Enabling Wireless Sensors with IEEE 802.15.4™*, 2nd ed. IEEE Press, 2007.

[74] D. Flowers and Y. Yang, "AN1066 - MiWi™ wireless networking protocol stack," 2007.

[75] G. Burdea and P. Coiffet, *Virtual reality technology*, 2nd ed. Hoboken, N.J.: John Wiley, 2003.

[76] C. V. C. Bouten, K. T. M. Koekkoek, M. Verduin, R. Kodde, and J. D. Janssen, "A triaxial accelerometer and portable data processing unit for the assessment of daily physical activity," *IEEE Transactions on Biomedical Engineering*, vol. 44, no. 3, pp. 136–147, 1997.

[77] M. J. Mathie, A. C. F. Coster, N. H. Lovell, and B. G. Celler, "Accelerometry: providing an integrated, practical method for long-term, ambulatory monitoring of human movement," *Physiological Measurement*, vol. 25, no. 2, pp. R1–R20, 2004.

[78] J. Hamill and K. Knutzen, *Biomechanical Basis of Human Movement*, 3rd ed. Philadelphia: Wolters Kluwer Health/Lippincott Williams and Wilkins, 2009.

[79] A. Bedford and W. L. Fowler, *Engineering Mechanics, Statics & Dynamics*, 5th ed. Harlow: Prentice Hall, 2008.

[80] B. Hingtgen, J. R. McGuire, M. Wang, and G. F. Harris, "An upper extremity kinematic model for evaluation of hemiparetic stroke," *Journal of Biomechanics*, vol. 39, no. 4, pp. 681–688, 2006.

[81] R. F. Beer, J. P. A. Dewald, M. L. Dawson, and W. Z. Rymer, "Target-dependent differences between free and constrained arm movements in chronic hemiparesis," *Experimental Brain Research*, vol. 156, no. 4, pp. 458–470, 2004.

[82] L. Euler, "Formulae generales pro translatione quacunque corporum rigidorum," *Novi Commentari Academiae Scientiarum Imperialis Petropolitanae*, vol. 20, pp. 189–207, 1775.

[83] W. F. Phillips, C. E. Hailey, and G. A. Gebert, "Review of attitude representations used for aircraft kinematics," *Journal of Aircraft*, vol. 38, no. 4, pp. 718–737, 2001.

[84] R. B. McGhee, E. R. Bachmann, and M. J. Zyda, "Rigid body dynamics, inertial reference frames, and graphics coordinate systems: A resolution of conflicting conventions and terminology," Naval Postgraduate School, Tech. Rep., 2000.

[85] W. R. Hamilton, "On quaternions; or on a new system of imaginaries in algebra," *Philosophical Magazine*, vol. 25, no. 3, pp. 489–495, 1844.

[86] J. Stuelpnagel, "On the parametrization of the three-dimensional rotation group," *SIAM Review*, vol. 6, no. 4, pp. 422–430, 1964.

[87] J. Nocedal and S. J. Wright, *Numerical optimization*, 2nd ed., ser. Springer series in operations research and financial engineering. New York: Springer, 2006.

[88] M. T. Heath, *Scientific computing : an introductory survey*, 2nd ed. Boston: McGraw-Hill, 2002.

[89] R. Fletcher, *Practical methods of optimization*, 2nd ed. Chichester ; New York: Wiley, 1987.

[90] F. Ferraris, U. Grimaldi, and M. Parvis, "Procedure for effortless in-field calibration of three-axis rate gyros and accelerometers," *Sensors and Materials*, vol. 7, no. 5, pp. 311–330, 1995.

[91] M. D. Shuster, "A survey of attitude representations," *Journal of the Astronautical Sciences*, vol. 41, pp. 439–517, 1993.

[92] H. Weinberg, "AN-1049 Calibrating iMEMS gyroscope," 2009.

[93] K. S. Low, G. X. Lee, and T. Taher, "A wearable wireless sensor network for human limbs monitoring," in *IEEE International Instrumentation and Measurement Technology Conference, I2MTC '09*, 2009, pp. 1332–1336.

[94] K. S. Kwak, S. Ullah, and N. Ullah, "An overview of IEEE 802.15.6 standard," in *3rd International Symposium on Applied Sciences in Biomedical and Communication Technologies (ISABEL)*, 2010, pp. 1–6.

[95] "IEEE Standard for Local and metropolitan area networks Part 15.6: Wireless Body Area Networks," *IEEE Std 802.15.6-2012*, pp. 1–271, 2012.

[96] X. Yun, E. R. Bachmann, H. Moore, IV, and J. Calusdian, "Self-contained position tracking of human movement using small inertial/magnetic sensor modules," in *IEEE International Conference on Robotics and Automation*, 2007, pp. 2526–2533.

[97] C. Huang, Z. Liao, and L. Zhao, "Synergism of INS and PDR in self-contained pedestrian tracking with a miniature sensor module," *IEEE Sensors Journal*, vol. 10, no. 8, pp. 1349–1359, 2010.

[98] N. Patwari and J. Wilson, "RF sensor networks for device-free localization: Measurements, models, and algorithms," *Proceedings of the IEEE*, vol. 98, no. 11, pp. 1961–1973, 2010.

[99] G. Wang and K. Yang, "A new approach to sensor node localization using RSS measurements in wireless sensor networks," *IEEE Transactions on Wireless Communications*, vol. 10, no. 5, pp. 1389–1395, 2011.

[100] I. P. Prikhodko, S. A. Zotov, A. A. Trusov, and A. M. Shkel, "Foucault pendulum on a chip: angle measuring silicon MEMS gyroscope," in *IEEE 24th International Conference on Micro Electro Mechanical Systems (MEMS)*, 2011, pp. 161–164.